Design principles for cadmium chalcogenide nanoparticle assembly via peptoids

Madison Monahan

A dissertation

submitted in partial fulfillment of the

requirements for the degree of

Doctor of Philosophy

University of Washington

2022

Reading Committee:

James De Yoreo, Chair

Brandi Cossairt

Daniel Gamelin

Program Authorized to Offer Degree:

Chemistry

University of Washington

Abstract

Design principles for cadmium chalcogenide nanoparticle assembly via peptoids

Madison Monahan

Chair of the Supervisory Committee:
Affiliate Professor James De Yoreo
Department of Chemistry and Materials Science & Engineering

Self-assembled organic nanomaterials can be generated by bottom-up assembly pathways where the structure is controlled by the organic sequence and altered using pH, temperature, and solvation. These nanomaterials have been used as scaffolds for assembly of inorganic materials but are limited to architectures accessible by the organic monomers. In contrast, self-assembled structures based on inorganic nanoparticles typically rely on physical packing and drying effects to achieve uniform superlattices. By combining these two chemistries to access inorganic-organic nanostructures, we aim to understand the key factors that govern the assembly pathway and structural outcomes in hybrid systems. This dissertation focuses on the assembly of peptidomimetic poly-N-substituted glycines, also known as peptoids. We explore the combination of peptoids with cadmium chalcogenide clusters and quantum dots (QDs) to

generate hybrid materials. By creating a set of design principles for controlling the structure and structural evolution of hybrid peptoid-QD assemblies we are closer to the predictive synthesis of complex hybrid matter.

Chapter 1 introduces the field of hybrid nanomaterials with a focus on peptoids and semiconducting nanoparticles. The properties, functions, and assembly of peptoids and nanoparticles are reviewed and the inherent challenges in coupling these two disparate building blocks are highlighted. Chapter 2 demonstrates the use of preformed peptoid nanostructures as scaffolds for CdSe nanoparticle assembly via an irreversibly formed covalent linkage. The structure of the resulting hybrid materials is explored using ex-situ transmission electron microscopy (TEM) and atomic force microscopy (AFM), and methods to control the density of nanoparticles on the peptoid surfaces are developed. Furthermore, we probe the chemistry underlying the covalent conjugation using ^{1}H NMR spectroscopy. Chapter 3 describes a bottom-up approach to QD assembly with peptoids that relies on reversible peptoid monomer coordination to QD surfaces. The synthesis of hybrid QD/peptoid monomers is developed. The surface chemistry and size of the QD were demonstrated as viable handles to alter the hybrid monomer solubility in various solvents, ultimately resulting in rational access to different hybrid morphologies.

TABLE OF CONTENTS

LIST OF FIGURES

LIST OF TABLES

LIST OF SCHEMES

ACKNOWLEDGEMENTS

Graduate school has been quite a process with both great challenges and accomplishments. Getting a PhD wouldn't be possible without a large support system within UW and through friends and family. First and foremost, I would like to thank my family who have supported me every step of the way. They reminded me that there is a life outside of graduate school, provided comic relief, and always had an open bed and fresh food when I needed a break. My husband and our two dogs supported me both physically and emotionally through the exams, countless moves, and looked the other way when I'd stress clean the baseboards. My friends have put up with slow replies and flakey scheduling with compassion and understanding. They have been my biggest hype girls and pushed me to have fun every once and a while.

I have had the pleasure to work with not one but two wonderful labs during my time at UW. The De Yoreo lab, while scattered across the state, provided different perspectives and solutions to complex problems. They were game to tackle any project and offer tips and tricks on how to get the best microscopy images. The Cossairt lab took me in early on in my graduate career and taught me how to be an inorganic chemist. They provided a helping hand, guidance, and open ears through the failed syntheses, all with good humor. The lab was more than a group of coworkers but a second family who understood the struggle of grad school but could always see the light at the end of your tunnel, even when they couldn't see their own. I will miss every one of you and cannot wait to see all the amazing accomplishments to come.

Finally, I need to give my biggest gratitude to my two advisors, Brandi and Jim. While from two completely different backgrounds, they came together to tackle complex problems with the same enthusiasm for science. They supported me and their other graduate students by thinking outside the box when we hit a wall and reminding us why the work we do is so exciting. Through everything, they always believed in me and were open whenever I needed someone to talk to, whether it was about science or life in general. I truly cannot image better advisors to have. Thank you, Brandi and Jim.

Chapter 1. INTRODUCTION

1.1 BIO INSPIRED NANOMATERIALS

Nature has optimized the interplay between structure and function in materials through design of hierarchy. A classic example of this complex hierarchy can be found in bone, wherein collagen fibrils mineralize hydroxyapatite nanoparticles, which together interact with proteins and water to form a unique material with robust mechanical properties (**Figure 1.1**).[1] In creating structure across many length scales, properties generated on the nanoscale can impact those observed on the microscale.[2] Functional hybrid materials have great promise for applications where the assembled materials can have distinct properties from the building blocks alone. Through assembly the material may show increased stability under a variety of conditions, enhancement of the intrinsic building block properties, or the generation of emergent properties arising from cooperativity between the hybrid components, such as electronic communication.[3-7] Hybrid assemblies are typically composed of an organic and inorganic component.[2] Organic components are typically soft with high elasticity, low density, and lower thermal stability. In contrast, inorganic materials display opposing properties with high rigidity, strength, density, and thermal stability. By coupling these two types of materials, a hybrid can be generated that displays favorable characteristics from both materials. If we can understand the interactions between organic and inorganic components and how to direct assembly between the two on the atomic scale, we can predictively synthesize materials with targeted morphologies and properties.

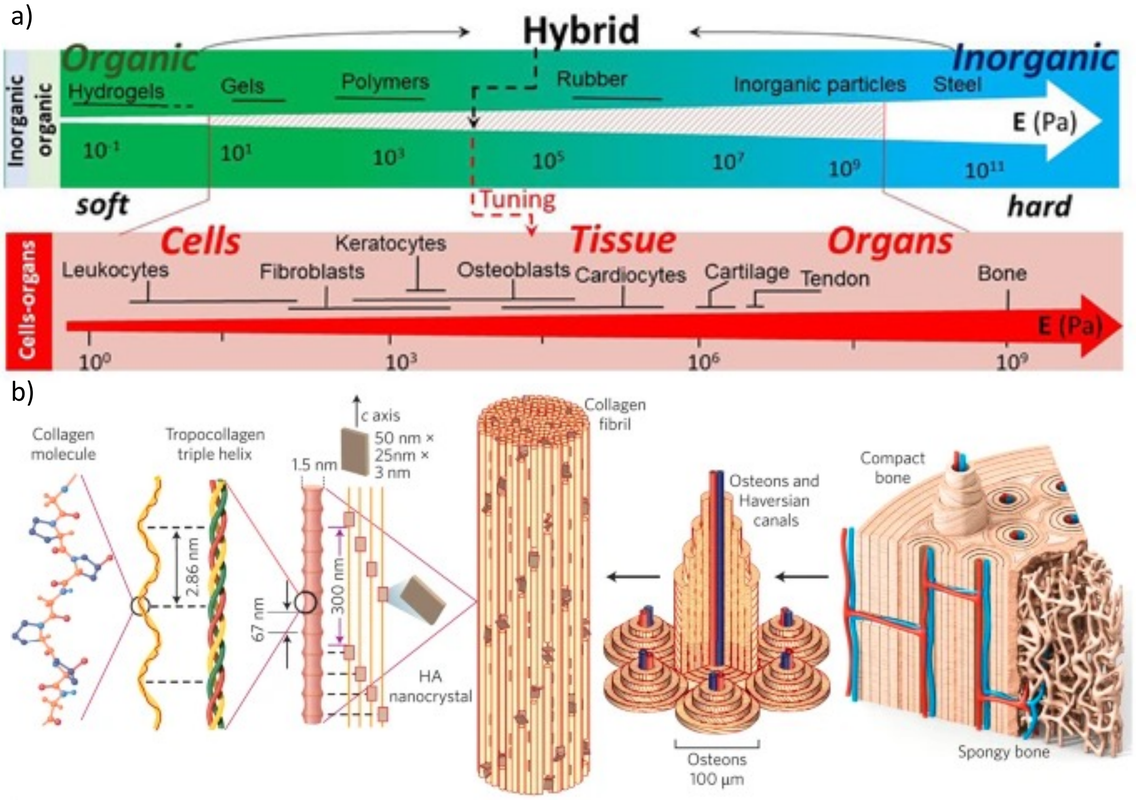

Figure 1.1. Hierarchical structure in synthetic systems using inorganic and organic materials compared to those in nature such cells and organs (a). The complex architecture of bone from a collagen molecule with high flexibility to compact bone with high rigidity and strength (b). Adapted from ref 1, 2.

There has been significant work on integrating inorganic nanoparticles with organic scaffolds and linkers with high precision, most commonly with biomolecules. DNA has been widely used as both a scaffold on which to assemble nanoparticles and as linkers to direct assembly between nanoparticles (**Figure 1.2**).[7-11] Using complimentary strands, multiple types of nanoparticles can be assembled with precise locations relative to each other. The Mirkin group has demonstrated extensive control with DNA functionalized nanoparticles aligning large and small particles relative to each other and demonstrating mobility within a lattice, as an analog to study how an electron may move through an atomic lattice (**Figure 1.2a**).[8] These assemblies are not limited to 2D but also exhibit a high degree of control for the generation of 3D structures. Additionally, they have utilized multivalent DNA to define the valency and lattice of the 3D crystal.[9] DNA mediated assembly has been used for a variety of nanoparticle compositions ranging from metals to semiconductors as well as various morphologies for the nanoparticle and resulting structure (**Figure 1.2b**).[10, 11] Finally, they assemble in solution without relying on drying effects or external manipulation to facilitate the assembly process. While these hybrid materials show great promise for predictive control and optoelectronic and catalytic potential, they are limited to aqueous solutions due to the stability and solubility of DNA and other biomolecules.[10] In water, the types of inorganic nanoparticles that are stable and contain useful properties are limited, narrowing the potential applications and precise control over the inorganic component.

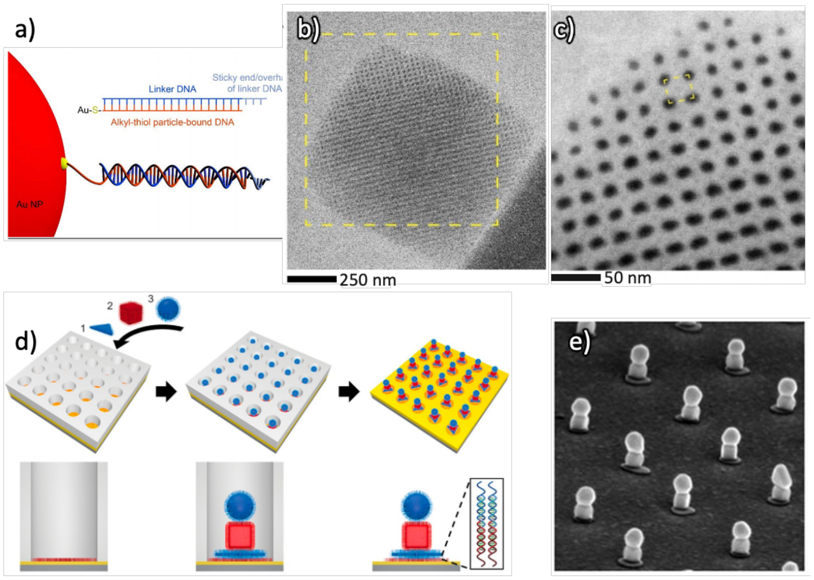

Figure 1.2. DNA mediated assembly of metal nanoparticles. Complimentary DNA strands attached to gold nanoparticles via thiols to act as a linker (a) for generation of ordered 3D assemblies with two sizes of nanoparticles (b,c). Vertical assemblies of nanoparticles via DNA

templating with various particle morphologies using alternating functionalization of complimentary DNA strands as ligation (d,e). Adapted from ref 8, 11.

1.2 PEPTOIDS FOR HYBRID MATERIALS

1.2.1 *Peptoids and their self-assembling properties*

Peptoids, poly-N-substituted glycines, are sequence-defined biomimetic polymers that closely resemble peptides.[12-14] Peptoids have the same backbone structure as peptides but with side chains located on the nitrogen rather than the alpha carbon (**Figure 1.3a,c**). The lack of amide hydrogens allows for solubility in a wide range of solvents, including organics, and for the structure to be more directly controlled by the sequence. Self-assembly in peptoids is dictated only by the sequence of the monomer, without secondary structure arising from phenomena such as hydrogen bonding. Simulations, in combination with AFM and SAXS experiments, have shown that for a sheet forming sequence the assembly is dictated by the quality or identity of the solvents and interactions between the aryl halogens.[15, 16] In these studies, the peptoid monomers first formed a disordered aggregate which evolved into a helical rod then finally ordered 2D nanosheets. Peptoids are highly engineered and can be tuned at the atomic level for precise control over the sequence and structure that can be generated (**Figure 1.3**). These polymers can be synthesized through two routes, solid-phase synthesis, or solution polymerization.[14] Solid-phase synthesis involves the sequential addition of amine monomers to the base chain, immobilized on resin, allowing for precise control over the sequence unlike a traditional polymer that incorporates monomers randomly. Additionally, there is a wide range of side chain possibilities as the monomers are not limited to amino acids but rather amine containing molecules. As such, the peptoid sequences, specifically their resulting structures and nucleation properties, can be quantitively studied based on identification of the side chain, number of repeat units, and location of side chains relative to each other.[16]

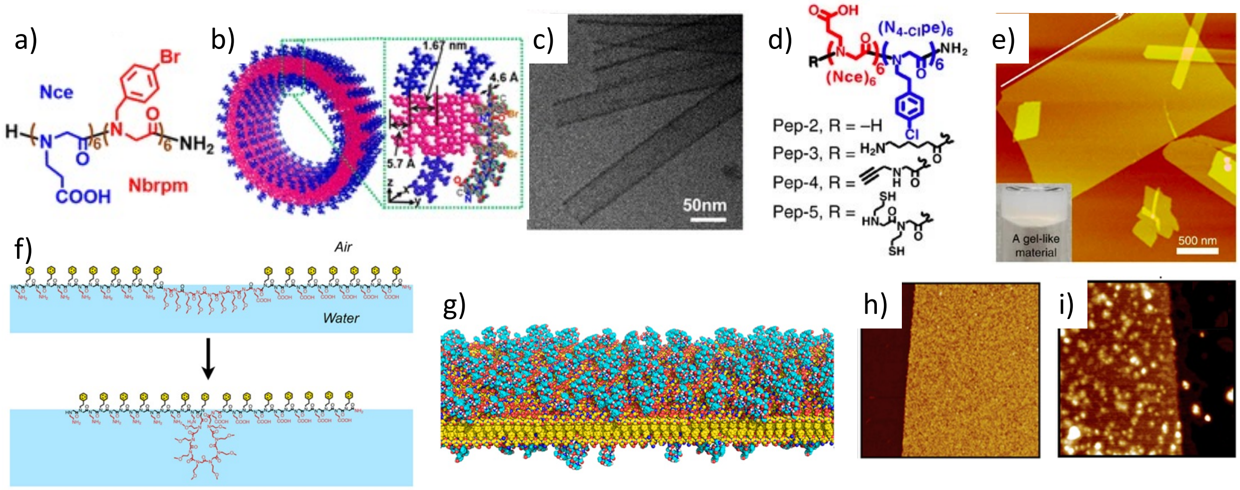

Figure 1.3. Peptoid nanostructures formed based on the peptoid sequence. Diblock peptoid sequences for tube (a,c) and sheet (d,e) formation with an interdigitation of the hydrophobic regions (b). Peptoid sequence engineer with a loop feature (f) that, once assembled, sits on the surface of the nanosheet (g,h) and can act as a nucleation site for gold (i). Adapted from ref 18, 19, 31.

Peptoids have been shown to assemble into a variety of structures including tubes, sheets, helices, micelles, and various intermediates (**Figure 1.3**).[17-22] A common type of self-assembling peptoids is a di-block sequence consisting of a hydrophobic and hydrophilic region. These sequences have been shown to generate highly crystalline nanotubes and 2D sheets that mimic membranes.[18, 19] For both of these structures, the peptoid monomers have been shown to form an interdigitated bilayer. In this bilayer the peptoids stack into alternating rows of “up” and “down” monomers with the hydrophilic region on the monomer on the surface (**Figure 1.3b**).[23] Assembly of such structures is initiated through an evaporative process with a mixed solvent system (1:1, water:organic solvent) where initially the monomers are soluble. As the organic solvent slowly evaporates, the environment becomes less favorable for the hydrophobic regions of the monomers, which assemble through interdigitation driven typically through π-π stacking of aryl halogens, leaving the hydrophilic residues on the surface of the structures. The van der Waals forces within the bilayer produce a robust structure that is stable across a wide range of pH (2-10), temperature, and mechanical stress. Finally, these structures are dynamic where the peptoid monomers can move or be replaced. Studies have been performed to damage the peptoid sheets, removing sections, that upon flow of peptoid monomer solution are seen to repair to return the sheet to its original form (**Figure 1.4**).[18]

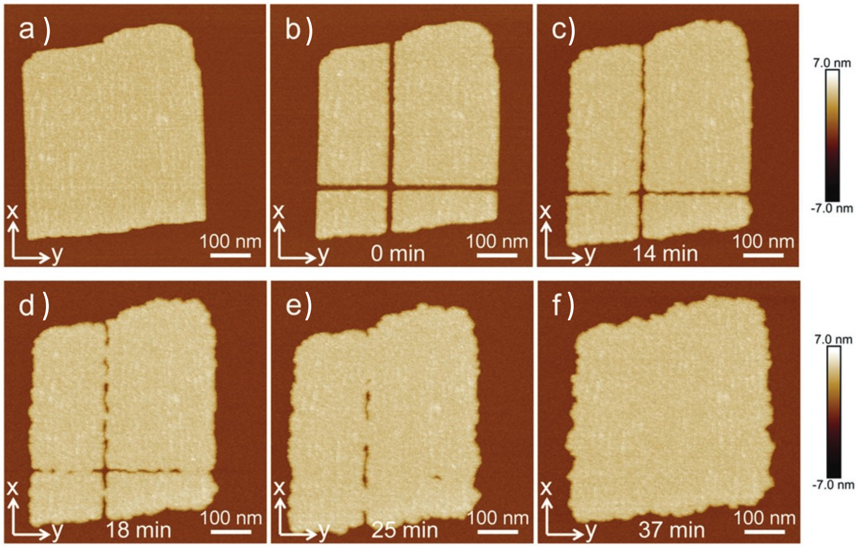

Figure 1.4. Peptoid nanosheets (a), damaged with an AFM tip (b), show self-healing upon the flow of peptoid monomer until sections have been filled (c-f). Adapted from ref 18.

1.2.2 *Structure and assembly pathways based on sequence*

While peptoid structure is primarily dictated by the backbone sequence, it can be tuned by solvent, pH, and pendant groups on the end of the peptoid.[15, 18, 19, 24-28] Peptoids have been well studied as a function of their sequence and assembly conditions. As previously mentioned, most peptoid assembly, at least in the case of diblock peptoids, is induced by the slow evaporation of an organic solvent used to solubilize the peptoid monomer. Studies have shown that the identity of this organic solvent can alter the assembly, impacting both the formation mechanism and quality of the structures formed.[16] Further studies have shown that the pH and salt can impact the structures formed, resulting in the formation of nanoribbons or micelles rather than sheets.[24, 25] Other work has shown that simply changing the end or pendant group in the hydrophilic region has a large impact on assembly. Work by Ma et al. showed that by adding a carbon chain to the end rather than a carbocyclic acid changed the assembly pathway, inducing an aggregated intermediate (**Figure 1.5a**).[26] Other work by Jiao et al. showed that adding a bulky cyclodextrin group to the end of the monomer changed the assembly mechanism where the peptoids could no longer interdigitate due to disruption in packing from the cyclodextrin (**Figure 1.5b**).[24] In this study, micelles, cylindrical micelles, or 2D films could all be generated from the same sequence by changing the pH, salt concentration, and surface which the peptoids were allowed to assemble on.

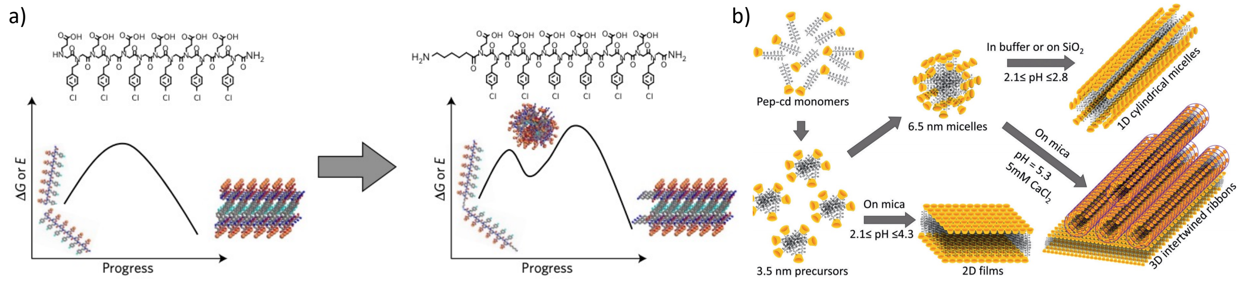

Figure 1.5. Pendant groups on peptoid monomers altering the intermediates in assembly and final structure. Addition of a carbon chain adds an aggregated intermediate in sheet formation (a). A

bulky end group, cyclodextrin, disrupts typical peptoid interdigitation to form micelles, tubes, or films depending on assembly conditions and solutes (b). Adapted from ref 24, 26.

Studies have also shown that introducing inorganic nanoparticles can influence not just the assembly pathway but the final structures. Polyhedral oligomeric silsesquioxanes (POSS) have been introduced at the time of monomer synthesis, resulting in covalent coordination of the cluster to the peptoid monomer (**Figure 1.6a**).[27] In this system, the POSS cluster acted as the nonpolar region of the peptoid monomer with varying numbers of polar residues. This cluster did not disrupt the interdigitation of the peptoid monomers but was incorporated into the bilayer. The assembly pathway was altered, with nanoparticles forming initially that shrank with time, giving way to nanorods and finally sheets. Work by Ma et al. decorated pre-formed peptoid sheets with silica binding proteins then added silica nanoparticles into solution.[28] The addition of the nanoparticles induced stacking of the nanosheets to generate a 3D layered structure where the silica acted as a binder between sheets (**Figure 1.6b**). In addition to end groups, the change in peptoid structures and assembly as a function of sequence have been investigated. A standard diblock peptoid with six polar residues (N-(2-carboxyethyl)glycine) and six nonpolar residues (N-[2-(4-bromophenyl)ethyl]glycine) assembled into nanoparticles and nanoribbons that with time grew into nanosheets.[18] Maintaining the sequence but changing the nonpolar region to (N-[2-(4-bromophenyl)methyl]glycine) was shown to follow the same basic assembly but the nanoribbons were seen to roll into nanotubes and no nanosheets formed (**Figure 1.3a-c**).[19]

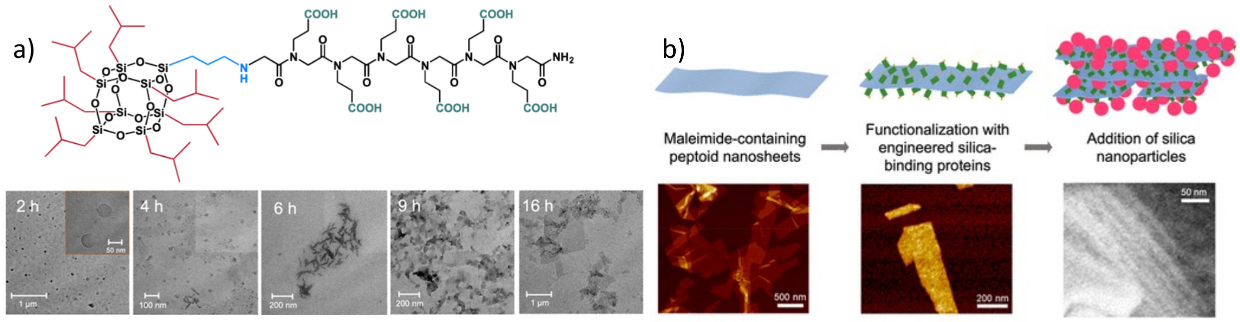

Figure 1.6. Silica nanoparticles altering peptoid assembly pathways and final structures. Hydrophobic silica clusters in cooperated into the peptoid monomer shown to assemble into nanosheets with the clusters inside the bilayer (a). Peptoid nanosheets decorated with solid-binding proteins on the surface then stacked into a layered structure through addition of silica nanoparticles (b). Adapted from ref 27, 28.

1.2.3 *Templated nucleation and growth using peptoid scaffolds*

Peptoids have been demonstrated as versatile platforms, as monomers and assembled structures, for nucleation and growth of inorganic nanoparticles.[29-34] Nucleation has been studied with peptoid monomers to understand how changing the peptoid sequence can change the morphology of a given material. It has been found that gold nucleation can be tuned from spherical to highly branched particles as a function of peptoid sequence (**Figure 1.7a,b**).[29] The peptoid played a critical role in the formation and aggregation of nanorods to form branched particles based on the binding affinity to the gold surface. More recent work has shown specific peptoid sequences promoting the formation of twinned gold nanostars through particle attachment (**Figure 1.7c-e**).[30] In this study the peptoid was shown to stabilize the (111) facets, promoting the attachment of particles in the [100] direction generating the nanostar morphology. Both of these studies utilized theory to outline the key interactions between various peptoid side chains and gold to understand the key interactions and move toward predictive synthesis. Peptoid monomers have also been engineered with a mid-sequence “loop” that upon nanosheet formation creates loops on the surface that can be used as controlled gold nucleation sites (**Figure 1.3f-i**).[31] Beyond gold, peptoids nanosheets have been used to control the nucleation of zeolite and palladium nanoparticles for catalytic applications, as well as calcite.[32-34]

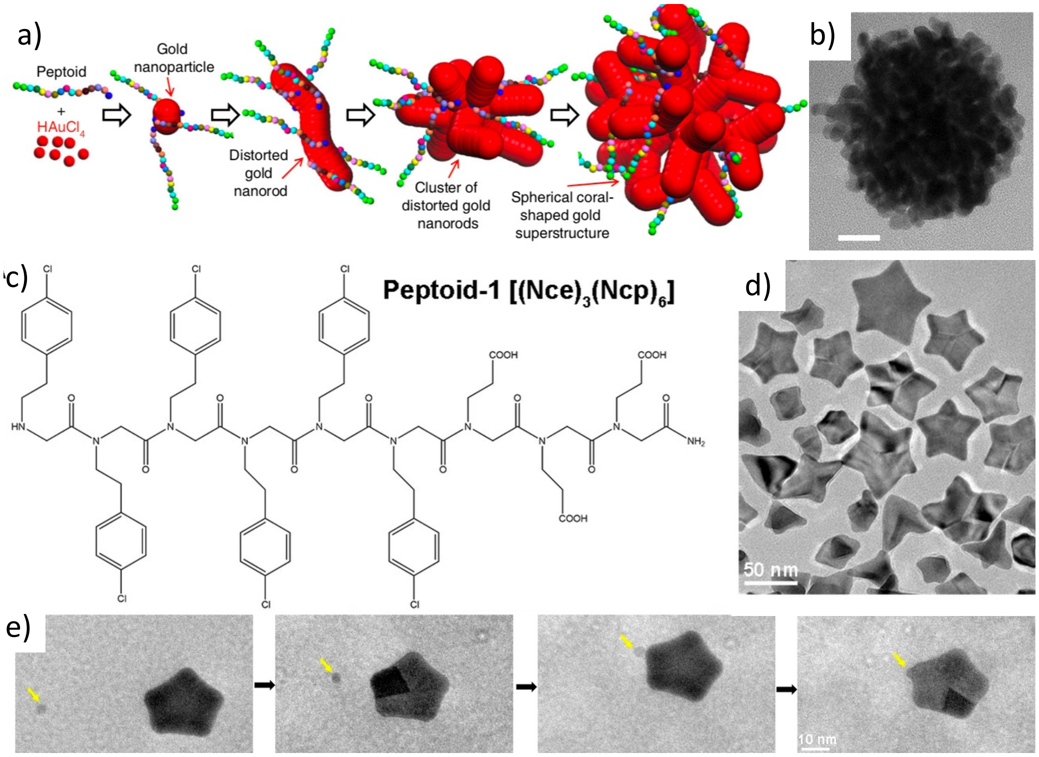

Figure 1.7. Peptoid-directed nucleation of complex gold nanoparticles. Formation of highly branched gold coral through peptoid mediated nanorod growth and aggregation (a) as seen by TEM (b). Diblock peptoids (c) seen to promote the formation of twinned nanostars (d) through stabilization of the (111) facets and growth along the [100] direction through particle attachment (e). Adapted from ref 29, 30.

1.3 SEMICONDUCTING NANOPARTICLES IN HYBRID MATERIALS

1.3.1 *Properties, synthesis, and surface chemistry of semiconducting nanoparticles*

To achieve predictive assembly, both the inorganic and organic components must be controlled to a high degree of accuracy and precision. Additionally, for the principles to be generalizable to a wide range of building blocks, the components should be tunable and easily studied to understand the interactions at play. Typically, metal nanoparticles are used in hybrid assemblies due to their stability in water, plasmonic properties, and ease of nucleation under mild, reducing conditions.[7-11] While useful for aqueous assembly of hybrid systems, metal nanoparticle-based structures have limited applications beyond plasmonics. Semiconducting nanoparticles (quantum dots), on the other hand, have absorption and photoluminescence properties that are precisely tunable based on their composition and size, and have found widespread use in optoelectronic technologies.[7, 35-38]

Quantum dots (QDs) can be synthesized under a wide range of conditions to target various morphologies, compositions, and optical properties.[39-41] While some syntheses are done in water, the reactivity and stability of precursors limits the types of quantum dots that can be synthesized this way. Beyond precursor stability, there has been less work on the precision synthesis of quantum dots in water, limiting the tunability of their optical properties and typically leading to an increase in sample polydispersity. As such, most reactions are done in organic solvents, such as hexadecane or octadecene, with long chain fatty acids to ligate the particle surface, resulting in a very hydrophobic material.[40-42] In addition to the hydrophobicity, the resulting particles are often air and water sensitive, oxidizing upon exposure and often causing a loss or change in optical properties over time.[43, 44] To combat this problem and make the quantum dots more stable, shelling is often employed. Typically, an insulating shell of zinc chalcogenide is added to confine the exciton and enhance the optical properties, however the surface of the particles remains hydrophobic.[39, 45, 46] Silica shells are also commonly used to encase the nanoparticles in a protective layer that is water soluble.[39, 47] These routes, while greatly increasing the stability of the particle, lead to significant surface modification and a decrease in overall homogeneity, making precise assembly more challenging. Another way to solubilize particles is through ligand exchange to place a more hydrophilic ligand on the surface.[48, 49] However, the addition of excess ligand, like carboxylic acids or thiols, can result in etching and destabilization. Ligand exchange does not offer any protection to the surface of the particle and must also be coupled with a shelling method if the optical properties are to be protected.

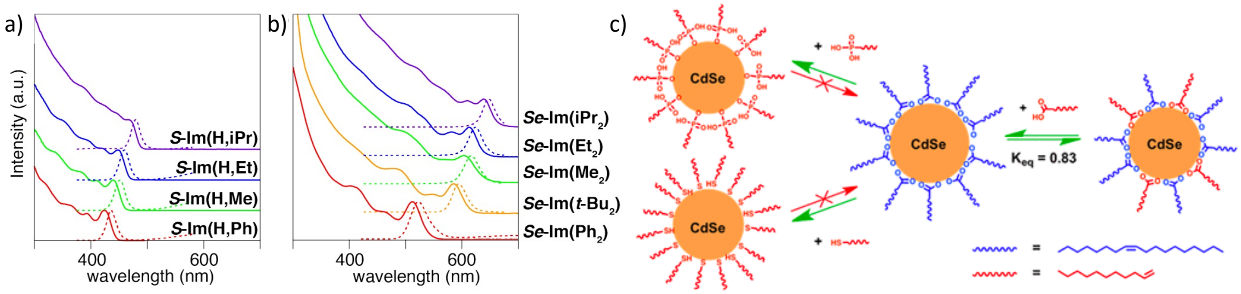

Figure 1.8. Size control of CdS (a) and CdSe (b) QDs based on the reactivity of the precursor, modulated by the substituents. Ligand exchange and binding affinity on CdSe QDs based on ligand head groups for -SH, -PO_3H_2, and -COOH (c). Adapted from ref 51, 53.

Cadmium chalcogenide nanoparticles have been widely studied with a variety of solvents, ligands, and synthetic conditions.[50-54] In these systems, the cadmium-ligand complexes are typically air stable and there are a variety of anion precursors, some of which are also air stable. The option to synthesize these materials in air or water allows for direct synthesis with hydrophilic ligands and water stability without surface modification. There have been numerous studies on how the optical properties of cadmium chalcogenides change as a function of size, and well documented syntheses targeting different sizes.[40, 51] Specifically, the Owen group has outlined how the reactivity of selenourea and thiourea precursors can directly change the size of chalcogenide-based quantum dots, with the less reactive precursors making larger QDs under the same reaction conditions (**Figure 1.8a,b**).[51] Beyond syntheses, the binding strengths of different ligand head groups and their exchange onto the surface of cadmium chalcogenide quantum dots has been well documented (**Figure 1.8c**).[53] At the smallest end of the size spectrum, cadmium chalcogenides also include magic sized clusters, which are atomically precise particles with perfect monodispersity.[50, 55, 56] Such clusters can be viewed as a smaller analog of the larger quantum dots, with similar reactivity, allowing for a more precise probe for directly studying interactions with organic molecules using techniques such as NMR spectroscopy. Starting with an inorganic core that has been well studied in both water and organic solvents allows for initial studies in water, the media which the organic peptoid components are well studied, to understand the compatibility and interactions between the two before branching into organic solvents. Additionally, by using a material that is tunable in both size, surface chemistry, solubility, and properties, we can outline assembly dynamics for the system and how it changes as a function of these parameters. In defining how specific parameters alter or direct assembly, we can get closer to predictive synthesis of hybrid materials and target different functionalities. Finally, by understanding the basic principles, we can expand the system to be generalizable to use a variety of core compositions to further expand the accessible properties.

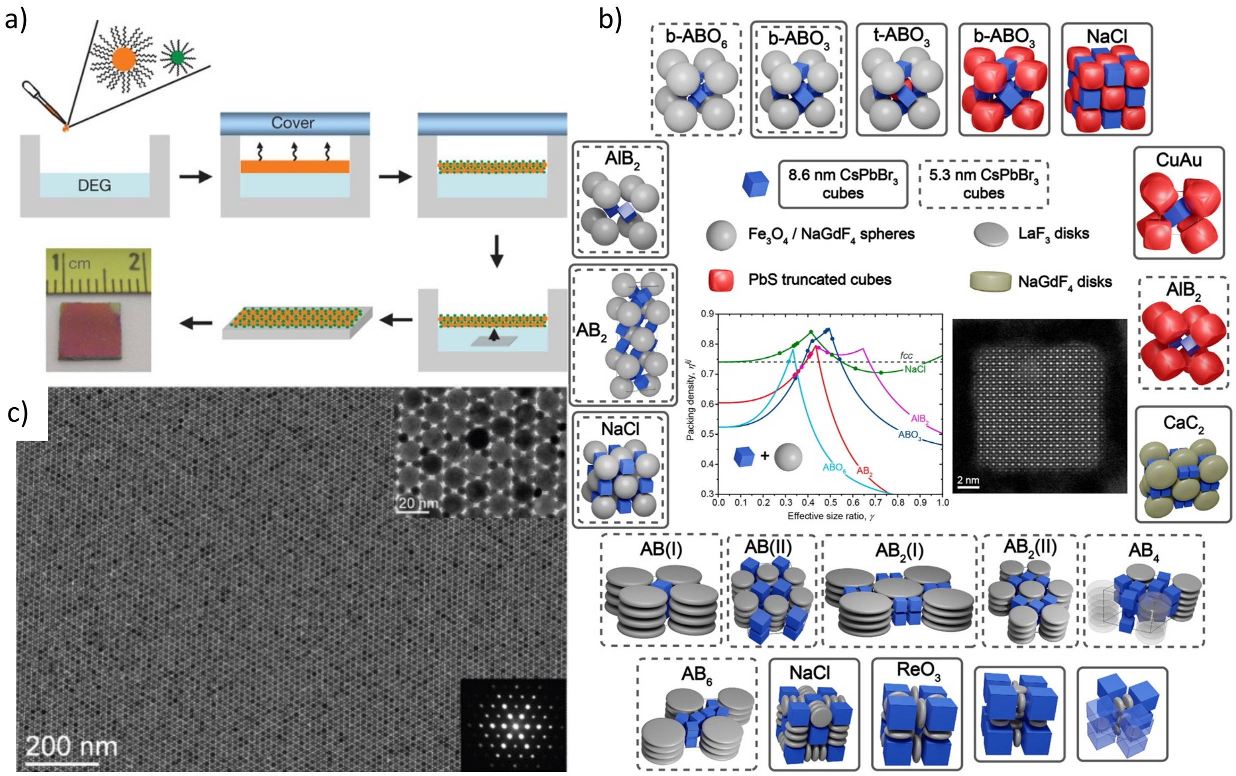

Figure 1.9. Nanoparticle-directed films through slow evaporation of solvent. Heterogeneous nanoparticle films generated through slow evaporation of solvent at an air-water interface (a). Films show a high uniformity and crystallinity by TEM (c). The packing structure and density of evaporative films can be altered by the particles morphology as well as effective size, calculated by the ratio of two different nanoparticles sizes (b). Adapted from ref 59, 60.

1.3.2 *Nanoparticle-directed assembly*

Assemblies directed by inorganic nanoparticles are typically achieved through drying to create 2D films of superlattices (**Figure 1.9a,c**).[57-62] In such films the nanoparticle size, morphology, and surface chemistry impact the structure of the generated lattices (**Figure 1.9b**).[58, 59] These structures are typically densely packed, without porosity and are limited in dimensionality and complexity. 3D assemblies of such films can be achieved by stacking of the layers. These structures have limited applications as they must be dried under specific conditions and do not maintain their structure upon re-solvation. The complexity of the films can be increased and the packing structure can be tuned by introducing nanoparticles of multiple sizes and shapes (**Figure 1.9b**).[58, 59] By altering the ratio of the large and small nanoparticles, the packing can be changed to a multitude of more complex structures. In addition to these films, assembly can be induced by altering the surface chemistry or facet specific interactions between the nanoparticles.[6, 63-67] In lead chalcogenide assemblies, square close pack films are common following fusion or interactions of the (100) facets due to decreased ligation, generating porous structures (**Figure 1.10a-c**).[6, 64-67] In examples where the structures are fused, an increase in electronic communication has been observed between quantum dots, paving the way for exciting optoelectronic device applications.[6] For the porous structures without fusion, assembly is initiated through drying.[64] Another type of assembly seen to have facet specificity are tetrahedron quantum dots.[63] Quasi-crystalline assemblies have also been generated through facet differentiation using CdS tetrahedrons where the {0002} facets were ligated by octadecyl phosphonic acid and the $\{10\bar{1}1\}$ by oleic acid (**Figure 1.10d**). This difference in ligation led to dimers between the QDs where the {0002} facets preferentially packed together that, upon drying, 10-fold quasi-crystalline films were generated (**Figure 1.10e-g**). This symmetry was achieved because of the particle morphology and patchy ligation.

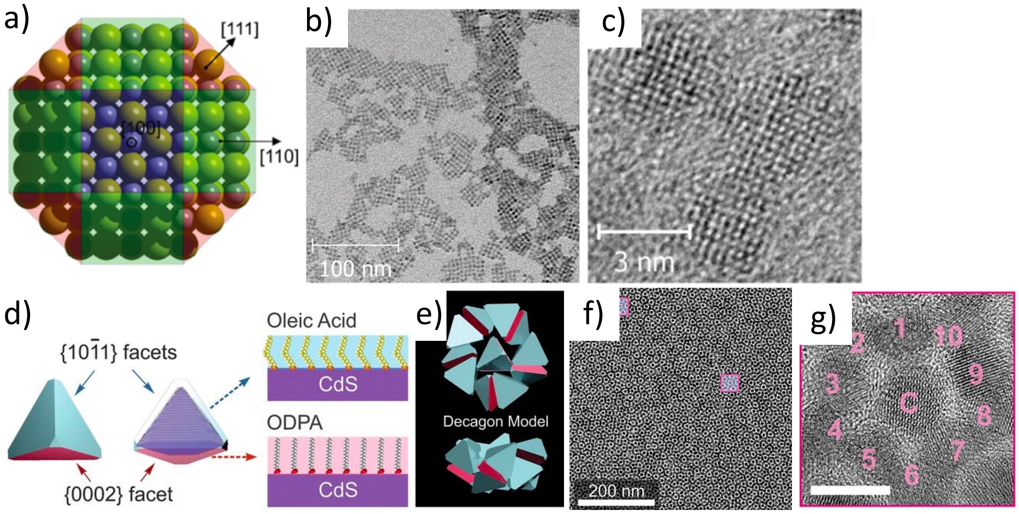

Figure 1.10. Nanoparticle assemblies based on facet-specific ligation differences. Lead chalcogenide QDs with reduced ligation on the (100) facet (a) initiating particle fusion and formation of square packed assemblies (b,c). CdS tetrahedrons with ODPA on the {0002} facet (d) creating dimers between two particles (e) that can assemble into 10-fold quasi-crystals, as seen by TEM (f,g). Adapted from ref 63, 66.

1.3.3 *Nanoparticle assemblies based in organic solvents*

To generate functional materials the building blocks, such as quantum dots, must have some inherent property such as photoluminescence or absorption features. By assembling quantum dots in organic solvents, the optical properties of the materials can be maintained without significant surface modification. Ordered assemblies have been achieved in organic solvents but are limited in terms of predictive control. Typically, these assemblies rely on the inorganic quantum dot interacting with an organic linker or structure directing scaffold.[57, 61, 62, 68, 69] 2D sheet-like assemblies can be generated *in situ* by adding rigid bifunctional linkers of similar length to the native ligand and incubating for a week (**Figure 1.11a,c,d**).[68] In such assemblies, the rigidity was found to be important to keep both functional groups on one linker from interacting with the same QD and the linker being long enough to penetrate two ligand shells. Additionally, the structures could be tuned from 2D to 3D by increasing the equivalents of linker in solution (**Figure 1.11e**). These assemblies show promise for applications in photocatalysis since the linker could be equipped with a bipyridine group to bind transition metals. Having the transition metal in close proximity to the QDs with a defined location could allow for optimization in photocatalysis by overcoming limitations associated with charge transfer and diffusion. Similar assemblies have been achieved using atomically precise CdSe clusters and amine linkers to generate crystalline 3D structures that exhibit catalytic activity (**Figure 1.11b**).[69] Through assembly of the CdSe clusters, the photoluminescence was enhanced with an increase in thermal stability of the material. The studies showed that through incorporation of Mn and Zn into the cluster cores the activity of the material could be modulated for cycloadditon of CO_2 gas with propylene oxide.

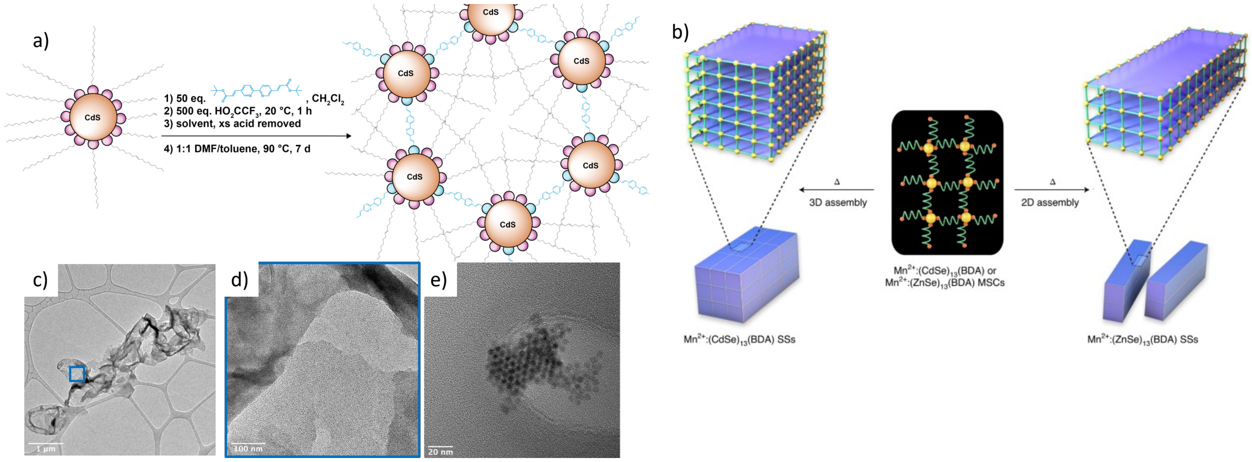

Figure 1.11. Nanoparticle assemblies with bifunctional linkers. Cadmium chalcogenide QDs assembled with 2,2′-bipyridine-5,5′-diacrylic acid (a) over 7 days to form 2D sheets (c) with distinct layers (d). Increasing the amount of linker present forms 3D ordered assemblies (e). CdSe and ZnSe clusters nucleated with diamine linkers to form 2D and 3D ordered assemblies with catalytic activity (b). Adapted from ref 68, 69.

Other studies have used polymers as linkers in organic media with promise both in achieving ordered assemblies and accessing a variety of morphologies.[70-73] Macfarlane and coworkers have done extensive work using polymer ligated nanoparticles with complimentary end groups to generate ordered assemblies through hydrogen boding (**Figure 1.12a**).[71-73] These polymers, terminated with diaminopyridine or thymine, selectively interact with one another allowing for incorporation of different sized nanoparticles in an ordered fashion. They further show control in the system by changing the length of the polymer, altering the polarity of the solvent, and altering the size and ratio of nanoparticles. Morphologies beyond films and crystalline blocks have been achieved using PbTe QDs with poly(3-hexylthiophene) nanowires (**Figure 1.12b,c**).[70] In these systems, they were able to generate long tendril structures decorated with QDs where they could control the density of QDs on the surface by tuning the QD concentration. These materials saw a decrease in photoluminescence and subsequent increase in charge transfer as they number of QDs on the surface increased. These studies have shown promise for ordered assemblies in organic solvents based on ligand modulation for a variety of structures and with functional applications. By further understanding these interactions and how to target different properties, predictive synthesis can be achieved for a wide variety of materials.

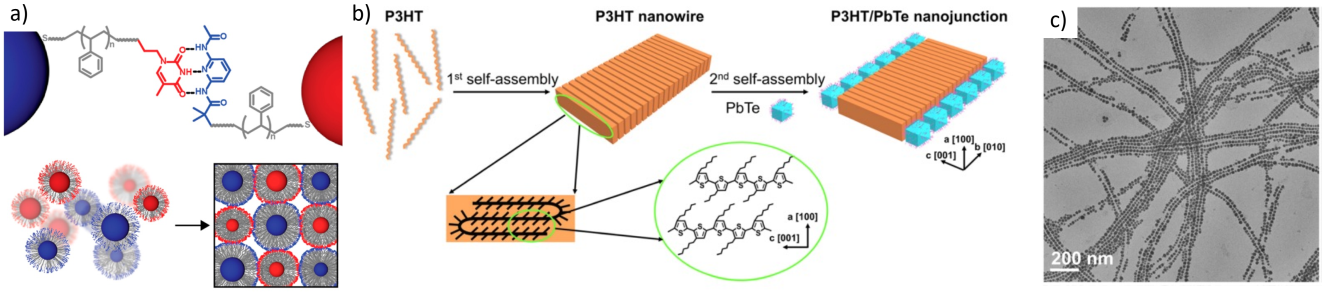

Figure 1.12. Assemblies of inorganic nanoparticles based in organic solutions. Polymer functionalized nanoparticles that form ordered superlattices in solution based on hydrogen bonding

(a). P3HT nanowires that self-assemble and can be controllable decorated with PbTe (b) as seen by TEM (c). Adapted from ref 70, 72.

1.4 REFERENCES

1. Wegst, U. G. K.; Bai, H.; Saiz, E.; Tomsia, A. P.; Ritchie, R. O. Bioinspired Structural Materials. *Nature Mater* **2015**, *14* (1), 23–36.
2. Saveleva, M. S.; Eftekhari, K.; Abalymov, A.; Douglas, T. E. L.; Volodkin, D.; Parakhonskiy, B. V.; Skirtach, A. G. Hierarchy of Hybrid Materials—The Place of Inorganics-in-Organics in It, Their Composition and Applications. *Frontiers in Chemistry* **2019**, *7*.
3. Moradi, M.; Vaskin, A.; Staude, I.; Jäger, M.; Elbert, J.; Schubert, U. S. Photoluminescence Switching of CdSe/ZnS Quantum Dots Toward Sensing Applications Triggered by Thermoresponsive Poly(N-Isopropylacrylamide) Films on Plasmonic Gold Surfaces. *ACS Appl. Nano Mater.* **2021**, *4* (3), 2386–2394.
4. Cargnello, M.; Johnston-Peck, A. C.; Diroll, B. T.; Wong, E.; Datta, B.; Damodhar, D.; Doan-Nguyen, V. V. T.; Herzing, A. A.; Kagan, C. R.; Murray, C. B. Substitutional Doping in Nanocrystal Superlattices. *Nature* **2015**, *524* (7566), 450–453.
5. Franke, M.; Leubner, S.; Dubavik, A.; George, A.; Savchenko, T.; Pini, C.; Frank, P.; Melnikau, D.; Rakovich, Y.; Gaponik, N.; Eychmüller, A.; Richter, A. Immobilization of PH-Sensitive CdTe Quantum Dots in a Poly(Acrylate) Hydrogel for Microfluidic Applications. *Nanoscale Research Letters* **2017**, *12* (1), 314.
6. Whitham, K.; Yang, J.; Savitzky, B. H.; Kourkoutis, L. F.; Wise, F.; Hanrath, T. Charge Transport and Localization in Atomically Coherent Quantum Dot Solids. *Nature Mater* **2016**, *15* (5), 557–563.
7. Li, Z.; Fan, Q.; Yin, Y. Colloidal Self-Assembly Approaches to Smart Nanostructured Materials. *Chem. Rev.* **2022**, *122* (5), 4976–5067.
8. Girard, M.; Wang, S.; Du, J. S.; Das, A.; Huang, Z.; Dravid, V. P.; Lee, B.; Mirkin, C. A.; Olvera de la Cruz, M. Particle Analogs of Electrons in Colloidal Crystals. *Science* **2019**, *364* (6446), 1174–1178.
9. Cheng, H. F.; Wang, S.; Mirkin, C. A. Electron-Equivalent Valency through Molecularly Well-Defined Multivalent DNA. *J. Am. Chem. Soc.* **2021**, *143* (4), 1752–1757.
10. Samanta, D.; Zhou, W.; Ebrahimi, S. B.; Petrosko, S. H.; Mirkin, C. A. Programmable Matter: The Nanoparticle Atom and DNA Bond. *Advanced Materials* **2022**, *34* (12), 2107875.
11. Lin, Q.-Y.; Mason, J. A.; Li, Z.; Zhou, W.; O'Brien, M. N.; Brown, K. A.; Jones, M. R.; Butun, S.; Lee, B.; Dravid, V. P.; Aydin, K.; Mirkin, C. A. Building Superlattices from Individual Nanoparticles via Template-Confined DNA-Mediated Assembly. *Science* **2018**, *359* (6376), 669–672.
12. DeStefano, A. J.; Segalman, R. A.; Davidson, E. C. Where Biology and Traditional Polymers Meet: The Potential of Associating Sequence-Defined Polymers for Materials Science. *JACS Au* **2021**, *1* (10), 1556–1571.
13. Li, Z.; Cai, B.; Yang, W.; Chen, C.-L. Hierarchical Nanomaterials Assembled from Peptoids and Other Sequence-Defined Synthetic Polymers. *Chem. Rev.* **2021**, *121* (22), 14031–14087.

14. Sun, J.; Zuckermann, R. N. Peptoid Polymers: A Highly Designable Bioinspired Material. *ACS Nano* **2013**, *7* (6), 4715–4732.
15. Hammons, J. A.; Baer, M. D.; Jian, T.; Lee, J. R. I.; Weiss, T. M.; De Yoreo, J. J.; Noy, A.; Chen, C.-L.; Van Buuren, A. Early-Stage Aggregation and Crystalline Interactions of Peptoid Nanomembranes. *J. Phys. Chem. Lett.* **2021**, *12* (26), 6126–6133.
16. Zhao, M.; Lachowski, K. J.; Zhang, S.; Alamdari, S.; Sampath, J.; Mu, P.; Mundy, C. J.; Pfaendtner, J.; De Yoreo, J. J.; Chen, C.-L.; Pozzo, L. D.; Ferguson, A. L. Hierarchical Self-Assembly Pathways of Peptoid Helices and Sheets. *Biomacromolecules* **2022**, *23* (3), 992–1008.
17. Cai, B.; Li, Z.; Chen, C.-L. Programming Amphiphilic Peptoid Oligomers for Hierarchical Assembly and Inorganic Crystallization. *Acc. Chem. Res.* **2021**, *54* (1), 81–91.
18. Jin, H.; Jiao, F.; Daily, M. D.; Chen, Y.; Yan, F.; Ding, Y.-H.; Zhang, X.; Robertson, E. J.; Baer, M. D.; Chen, C.-L. Highly Stable and Self-Repairing Membrane-Mimetic 2D Nanomaterials Assembled from Lipid-like Peptoids. *Nat Commun* **2016**, *7* (1), 12252.
19. Jin, H.; Ding, Y.-H.; Wang, M.; Song, Y.; Liao, Z.; Newcomb, C. J.; Wu, X.; Tang, X.-Q.; Li, Z.; Lin, Y.; Yan, F.; Jian, T.; Mu, P.; Chen, C.-L. Designable and Dynamic Single-Walled Stiff Nanotubes Assembled from Sequence-Defined Peptoids. *Nat Commun* **2018**, *9* (1), 270.
20. Wu, C. W.; Sanborn, T. J.; Huang, K.; Zuckermann, R. N.; Barron, A. E. Peptoid Oligomers with α-Chiral, Aromatic Side Chains: Sequence Requirements for the Formation of Stable Peptoid Helices. *J. Am. Chem. Soc.* **2001**, *123* (28), 6778–6784.
21. Robertson, E. J.; Battigelli, A.; Proulx, C.; Mannige, R. V.; Haxton, T. K.; Yun, L.; Whitelam, S.; Zuckermann, R. N. Design, Synthesis, Assembly, and Engineering of Peptoid Nanosheets. *Acc. Chem. Res.* **2016**, *49* (3), 379–389.
22. Sun, J.; Jiang, X.; Lund, R.; Downing, K. H.; Balsara, N. P.; Zuckermann, R. N. Self-Assembly of Crystalline Nanotubes from Monodisperse Amphiphilic Diblock Copolypeptoid Tiles. *Proceedings of the National Academy of Sciences* **2016**, *113* (15), 3954–3959.
23. Xuan, S.; Jiang, X.; Spencer, R. K.; Li, N. K.; Prendergast, D.; Balsara, N. P.; Zuckermann, R. N. Atomic-Level Engineering and Imaging of Polypeptoid Crystal Lattices. *Proceedings of the National Academy of Sciences* **2019**, *116* (45), 22491–22499.
24. Jiao, F.; Wu, X.; Jian, T.; Zhang, S.; Jin, H.; He, P.; Chen, C.-L.; De Yoreo, J. J. Hierarchical Assembly of Peptoid-Based Cylindrical Micelles Exhibiting Efficient Resonance Energy Transfer in Aqueous Solution. *Angewandte Chemie International Edition* **2019**, *58* (35), 12223–12230.
25. Castelletto, V.; Seitsonen, J.; Tewari, K. M.; Hasan, A.; Edkins, R. M.; Ruokolainen, J.; Pandey, L. M.; Hamley, I. W.; Lau, K. H. A. Self-Assembly of Minimal Peptoid Sequences. *ACS Macro Lett.* **2020**, *9* (4), 494–499.
26. Ma, X.; Zhang, S.; Jiao, F.; Newcomb, C. J.; Zhang, Y.; Prakash, A.; Liao, Z.; Baer, M. D.; Mundy, C. J.; Pfaendtner, J.; Noy, A.; Chen, C.-L.; De Yoreo, J. J. Tuning Crystallization Pathways through Sequence Engineering of Biomimetic Polymers. *Nature Mater* **2017**, *16* (7), 767–774.
27. Wang, M.; Song, Y.; Zhang, S.; Zhang, X.; Cai, X.; Lin, Y.; De Yoreo, J. J.; Chen, C.-L. Programmable Two-Dimensional Nanocrystals Assembled from POSS-Containing

Peptoids as Efficient Artificial Light-Harvesting Systems. *Science Advances* **2021**, *7* (20), eabg1448.

28. Ma, J.; Cai, B.; Zhang, S.; Jian, T.; De Yoreo, J. J.; Chen, C.-L.; Baneyx, F. Nanoparticle-Mediated Assembly of Peptoid Nanosheets Functionalized with Solid-Binding Proteins: Designing Heterostructures for Hierarchy. *Nano Lett.* **2021**, *21* (4), 1636–1642.
29. Yan, F.; Liu, L.; Walsh, T. R.; Gong, Y.; El-Khoury, P. Z.; Zhang, Y.; Zhu, Z.; De Yoreo, J. J.; Engelhard, M. H.; Zhang, X.; Chen, C.-L. Controlled Synthesis of Highly-Branched Plasmonic Gold Nanoparticles through Peptoid Engineering. *Nat Commun* **2018**, *9* (1), 2327.
30. Jin, B.; Yan, F.; Qi, X.; Cai, B.; Tao, J.; Fu, X.; Tan, S.; Zhang, P.; Pfaendtner, J.; Naser, N. Y.; Baneyx, F.; Zhang, X.; DeYoreo, J. J.; Chen, C.-L. Peptoid-Directed Formation of Five-Fold Twinned Au Nanostars through Particle Attachment and Facet Stabilization. *Angewandte Chemie International Edition* **2022**, *61* (14), e202201980.
31. Olivier, G. K.; Cho, A.; Sanii, B.; Connolly, M. D.; Tran, H.; Zuckermann, R. N. Antibody-Mimetic Peptoid Nanosheets for Molecular Recognition. *ACS Nano* **2013**, *7* (10), 9276–9286.
32. Li, R.; Smolyakova, A.; Maayan, G.; Rimer, J. D. Designed Peptoids as Tunable Modifiers of Zeolite Crystallization. *Chem. Mater.* **2017**, *29* (21), 9536–9546.
33. Merrill, N. A.; Yan, F.; Jin, H.; Mu, P.; Chen, C.-L.; Knecht, M. R. Tunable Assembly of Biomimetic Peptoids as Templates to Control Nanostructure Catalytic Activity. *Nanoscale* **2018**, *10* (26), 12445–12452.
34. Nielsen, A. R.; Jelavić, S.; Murray, D.; Rad, B.; Andersson, M. P.; Ceccato, M.; Mitchell, A. C.; Stipp, S. L. S.; Zuckermann, R. N.; Sand, K. K. Thermodynamic and Kinetic Parameters for Calcite Nucleation on Peptoid and Model Scaffolds: A Step toward Nacre Mimicry. *Crystal Growth & Design* **2020**, *20* (6), 3762–3771.
35. Ibáñez, M.; Luo, Z.; Genç, A.; Piveteau, L.; Ortega, S.; Cadavid, D.; Dobrozhan, O.; Liu, Y.; Nachtegaal, M.; Zebarjadi, M.; Arbiol, J.; Kovalenko, M. V.; Cabot, A. High-Performance Thermoelectric Nanocomposites from Nanocrystal Building Blocks. *Nat Commun* **2016**, *7* (1), 10766.
36. Jin, H.; Li, J.; Iocozzia, J.; Zeng, X.; Wei, P.-C.; Yang, C.; Li, N.; Liu, Z.; He, J. H.; Zhu, T.; Wang, J.; Lin, Z.; Wang, S. Hybrid Organic–Inorganic Thermoelectric Materials and Devices. *Angewandte Chemie International Edition* **2019**, *58* (43), 15206–15226.
37. Zheng, S.; Chen, J.; Johansson, E. M. J.; Zhang, X. PbS Colloidal Quantum Dot Inks for Infrared Solar Cells. *iScience* **2020**, *23* (11), 101753.
38. Yuan, M.; Liu, M.; Sargent, E. H. Colloidal Quantum Dot Solids for Solution-Processed Solar Cells. *Nat Energy* **2016**, *1* (3), 1–9.
39. Farzin, M. A.; Abdoos, H. A Critical Review on Quantum Dots: From Synthesis toward Applications in Electrochemical Biosensors for Determination of Disease-Related Biomolecules. *Talanta* **2021**, *224*, 121828.
40. Rosenthal, S. J.; McBride, J.; Pennycook, S. J.; Feldman, L. C. Synthesis, Surface Studies, Composition and Structural Characterization of CdSe, Core/Shell and Biologically Active Nanocrystals. *Surface Science Reports* **2007**, *62* (4), 111–157.
41. Smith, A. M.; Nie, S. Semiconductor Nanocrystals: Structure, Properties, and Band Gap Engineering. *Acc. Chem. Res.* **2010**, *43* (2), 190–200.

42. Park, N.; Monahan, M.; Ritchhart, A.; Friedfeld, M. R.; Cossairt, B. M. Synthesis of In37P20(O2CR)51 Clusters and Their Conversion to InP Quantum Dots. *JoVE (Journal of Visualized Experiments)* **2019**, No. 147, e59425.
43. Shi, G.; Wang, H.; Zhang, Y.; Cheng, C.; Zhai, T.; Chen, B.; Liu, X.; Jono, R.; Mao, X.; Liu, Y.; Zhang, X.; Ling, X.; Zhang, Y.; Meng, X.; Chen, Y.; Duhm, S.; Zhang, L.; Li, T.; Wang, L.; Xiong, S.; Sagawa, T.; Kubo, T.; Segawa, H.; Shen, Q.; Liu, Z.; Ma, W. The Effect of Water on Colloidal Quantum Dot Solar Cells. *Nat Commun* **2021**, *12* (1), 4381.
44. Sykora, M.; Koposov, A. Y.; McGuire, J. A.; Schulze, R. K.; Tretiak, O.; Pietryga, J. M.; Klimov, V. I. Effect of Air Exposure on Surface Properties, Electronic Structure, and Carrier Relaxation in PbSe Nanocrystals. *ACS Nano* **2010**, *4* (4), 2021–2034.
45. Li, J. J.; Wang, Y. A.; Guo, W.; Keay, J. C.; Mishima, T. D.; Johnson, M. B.; Peng, X. Large-Scale Synthesis of Nearly Monodisperse CdSe/CdS Core/Shell Nanocrystals Using Air-Stable Reagents via Successive Ion Layer Adsorption and Reaction. *J. Am. Chem. Soc.* **2003**, *125* (41), 12567–12575.
46. Grabolle, M.; Ziegler, J.; Merkulov, A.; Nann, T.; Resch-Genger, U. Stability and Fluorescence Quantum Yield of CdSe–ZnS Quantum Dots—Influence of the Thickness of the ZnS Shell. *Annals of the New York Academy of Sciences* **2008**, *1130* (1), 235–241.
47. Ma, Y.; Li, Y.; Ma, S.; Zhong, X. Highly Bright Water-Soluble Silica Coated Quantum Dots with Excellent Stability. *J. Mater. Chem. B* **2014**, *2* (31), 5043–5051.
48. Zhang, Y.; Clapp, A. Overview of Stabilizing Ligands for Biocompatible Quantum Dot Nanocrystals. *Sensors* **2011**, *11* (12), 11036–11055.
49. Wang, M.; Felorzabihi, N.; Guerin, G.; Haley, J. C.; Scholes, G. D.; Winnik, M. A. Water-Soluble CdSe Quantum Dots Passivated by a Multidentate Diblock Copolymer. *Macromolecules* **2007**, *40* (17), 6377–6384.
50. Beecher, A. N.; Yang, X.; Palmer, J. H.; LaGrassa, A. L.; Juhas, P.; Billinge, S. J. L.; Owen, J. S. Atomic Structures and Gram Scale Synthesis of Three Tetrahedral Quantum Dots. *J. Am. Chem. Soc.* **2014**, *136* (30), 10645–10653.
51. Hamachi, L. S.; Yang, H.; Jen-La Plante, I.; Saenz, N.; Qian, K.; Campos, M. P.; Cleveland, G. T.; Rreza, I.; Oza, A.; Walravens, W.; Chan, E. M.; Hens, Z.; Crowther, A. C.; Owen, J. S. Precursor Reaction Kinetics Control Compositional Grading and Size of $CdSe_{1-x}S_x$ Nanocrystal Heterostructures. *Chem. Sci.* **2019**, *10* (26), 6539–6552.
52. Zhao, L.; Hu, L.; Fang, X. Growth and Device Application of CdSe Nanostructures. *Adv. Funct. Mater.* **2012**, *22* (8), 1551–1566.
53. Knauf, R. R.; Lennox, J. C.; Dempsey, J. L. Quantifying Ligand Exchange Reactions at CdSe Nanocrystal Surfaces. *Chem. Mater.* **2016**, *28* (13), 4762–4770.
54. Mussa Farkhani, S.; Valizadeh, A. Review: Three Synthesis Methods of CdX (X = Se, S or Te) Quantum Dots. *IET Nanobiotechnology* **2014**, *8* (2), 59–76.
55. Cossairt, B. M.; Juhas, P.; Billinge, S. J. L.; Owen, J. S. Tuning the Surface Structure and Optical Properties of CdSe Clusters Using Coordination Chemistry. *J. Phys. Chem. Lett.* **2011**, *2* (24), 3075–3080.
56. Sadeghi, S.; Khabbaz Abkenar, S.; Ow-Yang, C. W.; Nizamoglu, S. Efficient White LEDs Using Liquid-State Magic-Sized CdSe Quantum Dots. *Sci Rep* **2019**, *9* (1), 10061.
57. Si, K. J.; Chen, Y.; Shi, Q.; Cheng, W. Nanoparticle Superlattices: The Roles of Soft Ligands. *Adv. Sci.* **2018**, *5* (1), 1700179.

58. Chen, Z.; O'Brien, S. Structure Direction of II−VI Semiconductor Quantum Dot Binary Nanoparticle Superlattices by Tuning Radius Ratio. *ACS Nano* **2008**, *2* (6), 1219–1229.
59. Cherniukh, I.; Sekh, T. V.; Rainò, G.; Ashton, O. J.; Burian, M.; Travesset, A.; Athanasiou, M.; Manoli, A.; John, R. A.; Svyrydenko, M.; Morad, V.; Shynkarenko, Y.; Montanarella, F.; Naumenko, D.; Amenitsch, H.; Itskos, G.; Mahrt, R. F.; Stöferle, T.; Erni, R.; Kovalenko, M. V.; Bodnarchuk, M. I. Structural Diversity in Multicomponent Nanocrystal Superlattices Comprising Lead Halide Perovskite Nanocubes. *ACS Nano* **2022**.
60. Dong, A.; Chen, J.; Vora, P. M.; Kikkawa, J. M.; Murray, C. B. Binary Nanocrystal Superlattice Membranes Self-Assembled at the Liquid–Air Interface. *Nature* **2010**, *466* (7305), 474–477.
61. Lee, M. S.; Yee, D. W.; Ye, M.; Macfarlane, R. J. Nanoparticle Assembly as a Materials Development Tool. *J. Am. Chem. Soc.* **2022**, *144* (8), 3330–3346.
62. Boles, M. A.; Engel, M.; Talapin, D. V. Self-Assembly of Colloidal Nanocrystals: From Intricate Structures to Functional Materials. *Chem. Rev.* **2016**, *116* (18), 11220–11289.
63. Nagaoka, Y.; Zhu, H.; Eggert, D.; Chen, O. Single-Component Quasicrystalline Nanocrystal Superlattices through Flexible Polygon Tiling Rule. *Science* **2018**, *362* (6421), 1396–1400.
64. Liu, J.; Enomoto, K.; Takeda, K.; Inoue, D.; Pu, Y.-J. Simple Cubic Self-Assembly of PbS Quantum Dots by Finely Controlled Ligand Removal through Gel Permeation Chromatography. *Chem. Sci.* **2021**, *12* (30), 10354–10361.
65. Walravens, W.; De Roo, J.; Drijvers, E.; ten Brinck, S.; Solano, E.; Dendooven, J.; Detavernier, C.; Infante, I.; Hens, Z. Chemically Triggered Formation of Two-Dimensional Epitaxial Quantum Dot Superlattices. *ACS Nano* **2016**, *10* (7), 6861–6870.
66. Balazs, D. M.; Dirin, D. N.; Fang, H.-H.; Protesescu, L.; ten Brink, G. H.; Kooi, B. J.; Kovalenko, M. V.; Loi, M. A. Counterion-Mediated Ligand Exchange for PbS Colloidal Quantum Dot Superlattices. *ACS Nano* **2015**, *9* (12), 11951–11959.
67. Baumgardner, W. J.; Whitham, K.; Hanrath, T. Confined-but-Connected Quantum Solids via Controlled Ligand Displacement. *Nano Lett.* **2013**, *13* (7), 3225–3231.
68. Ritchhart, A.; Monahan, M.; Mars, J.; Toney, M. F.; De Yoreo, J. J.; Cossairt, B. M. Covalently Linked, Two-Dimensional Quantum Dot Assemblies. *Langmuir* **2020**, *36* (33), 9944–9951.
69. Baek, W.; Bootharaju, M. S.; Walsh, K. M.; Lee, S.; Gamelin, D. R.; Hyeon, T. Highly Luminescent and Catalytically Active Suprastructures of Magic-Sized Semiconductor Nanoclusters. *Nat. Mater.* **2021**, *20* (5), 650–657.
70. Ni, B.; Fu, C.; Pan, S.; He, L.; Lin, Z.; Peng, J. Semiconducting Spaghetti-like Organic–Inorganic Nanojunctions via Sequential Self-Assembly of Conjugated Polymers and Quantum Dots. *Chem. Mater.* **2022**, *34* (2), 847–853.
71. Santos, P. J.; Cao, Z.; Zhang, J.; Alexander-Katz, A.; Macfarlane, R. J. Dictating Nanoparticle Assembly via Systems-Level Control of Molecular Multivalency. *J. Am. Chem. Soc.* **2019**, *141* (37), 14624–14632.
72. Lee, M. S.; Alexander-Katz, A.; Macfarlane, R. J. Nanoparticle Assembly in High Polymer Concentration Solutions Increases Superlattice Stability. *Small* **2021**, *17* (36), 2102107.
73. Zhang, J.; Santos, P. J.; Gabrys, P. A.; Lee, S.; Liu, C.; Macfarlane, R. J. Self-Assembling Nanocomposite Tectons. *J. Am. Chem. Soc.* **2016**, *138* (50), 16228–16231.

Chapter 2. Peptoid-Directed Assembly of CdSe Nanoparticles

Adapted with permission from the Royal Society of Chemistry. Copyright 2021 Nanoscale.

2.1 INTRODUCTION

Nature has perfected the coupling of discrete building blocks into complex hierarchical architectures to elicit distinct functionality. For this reason, synthetic chemists have sought versatile, scalable, and predictive platforms for accessing hierarchy.[1-5] Hybrid materials based on the combination of highly designable organic or biomolecular templates and functional inorganic building blocks are gaining momentum because of their optoelectronic and catalytic potential through synergistic interactions between the individual components of the material. Considerable work has been dedicated to understanding the side chain chemistry in block co-polymers to design materials with specific properties.[6-10] Additionally, protein design and 3D modeling have evolved to allow a great deal of control in directing biological structures, resulting in an organic lattice that is known with atomic precision.[11-14] By using individual subunits, where both the inorganic and organic components are known with atomic precision and can be tuned with atomic specificity, highly complex, compatible, and stable systems with new structures and properties can be designed.

Peptoids (or poly-N-substituted glycine) are highly tunable sequence-defined biomimetic building blocks, similar to peptides but lacking the amide hydrogen, allowing for a wider range in solubility and generating diverse and robust self-assembled nanostructures that are not readily achieved by peptide self-assembly.[15] Peptoids have been highly engineered and deeply studied to understand the self-assembled structures, their ability to nucleate and control the shape of inorganic particles, and how the side chains and periodicity alter these interactions.[16-22] One of the most common designs of self-assembling peptoids is a di-block sequence consisting polar and nonpolar domains, such as those shown in **Figure 2.1a,b**. Such di-block self-assembling peptoids have been demonstrated to form highly crystalline nanotubes or membrane-mimetic 2D nanosheets (**Figure 2.1a-e, g-j**), depending on the sequence in the hydrophobic region.[23-25] For both sheets and tubes, the peptoids form an interdigitated bi-layer in which the peptoids stack in alternating "upward"- and "downward"-pointing rows with the internal, hydrophobic regions stabilized by π stacking of the phenyl rings, and the hydrophilic regions exposed at the surface for interaction with the bulk aqueous solution (**Figure 2.1d,e**).[23,24] For the sequence used here, the bilayer thickness is 3.5- 4 nm depending on solution pH and salt concentration. Using similar peptoid sequences, these nanostructures have been shown to be stable over a range of pH values and temperatures.[24] The high stability of these peptoid nanosheet and nanotube scaffolds along with their easily functionalized hydrophilic regions results in an ideal structure for templating inorganic materials to access hybrid assemblies.

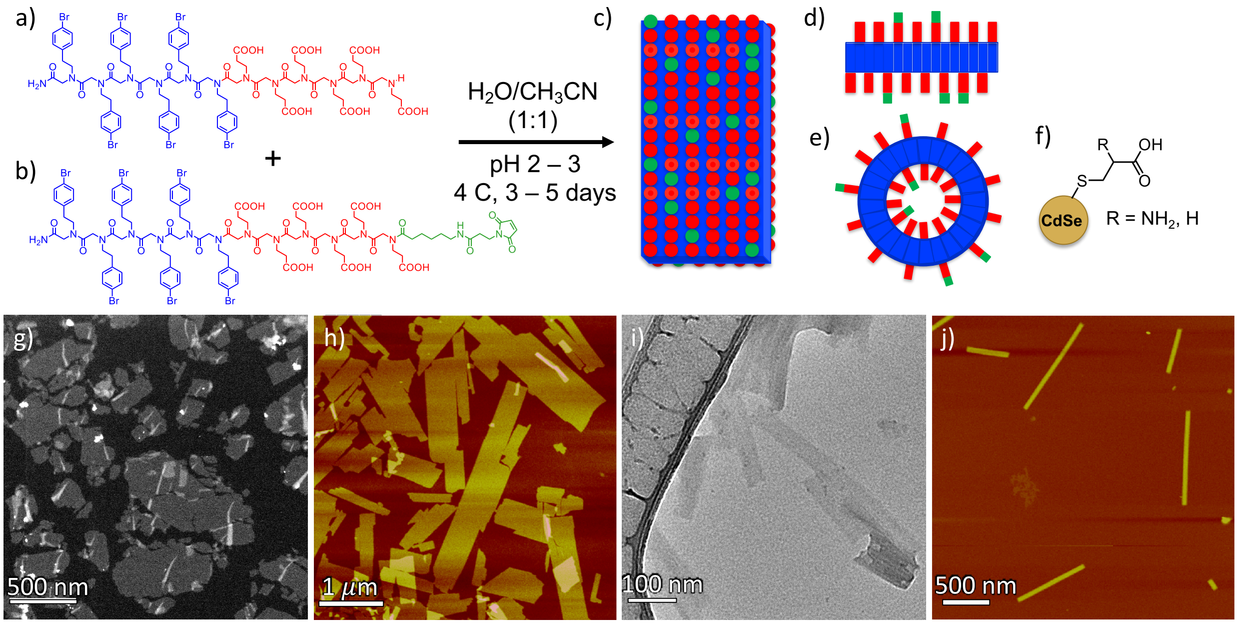

Figure 2.1. Diblock peptoid monomers (a) contain a hydrophobic region (blue) and a hydrophilic region (red). A mix of standard (a) and functionalized (b) monomers are mixed during assembly

to give a random distribution of maleimide functionalization on the surface (green, c). The hydrophobic regions of the monomers reside internally (blue) and hydrophilic regions reside externally (red) in the resulting interdigitated bi-layer peptoid sheets and tubes (d,e). CdSe particle (gold) attachment via the maleimide on the peptoid structure and a thiol in the capping ligand on the nanoparticle surface (f). Transmission electron microscopy (TEM) and atomic force microscopy (AFM) images of self-assembled peptoid sheets (g,h) and tubes (i,j). The unstained peptoids can be seen clearly via STEM (g) but require slight defocus to be resolved in bright field imaging (i).

In this work, we examine CdSe quantum dots (QDs) (**Fig. S1a**) and magic size clusters (MSCs) (**Fig. S1b**) capped with difunctionalized ligands containing carboxylic acid (-COOH) and thiol (-SH) moieties (**Figure 2.1f)** assembled in solution onto maleimide functionalized peptoid sheets and tubes, like those in **Figure 2.1g-j**. CdSe nanoparticles have a large history for use in water and biological systems, shown to be both water soluble and stable under a variety of conditions and surface chemistries.[26-30] Additionally, there has been significant work done on how to tune the spectroscopic properties of CdSe nanoparticles by both changing the size and capping-ligands.[31-34] The clusters and QDs give us two different systems that have similar composition and reactivity but different spectroscopic properties due to their size and structural differences.[35,36] Working with sheet-forming peptoids and QDs, the compatibility of the two systems is explored by altering the capping ligands of the particles and the side chains of peptoid backbones to create a system that is stable under the mildly acidic, aqueous conditions required for peptoid stability. We show control over the density of QDs on the surface of peptoid sheets as a function of maleimide percentage within the sheet. The system is proven generalizable by creating conjugates with peptoid nanotubes as well as extending the methodology to produce conjugates with atomically precise CdSe clusters. Finally, the QD and peptoid interactions are probed using NMR spectroscopy and different component compositions to determine the operative binding mechanism.

2.2 RESULTS AND DISCUSSION

2.2.1 *Conjugation of peptoid structures and CdSe particles.*

To create viable conjugation with the peptoid structures, the quantum dots must have complimentary functionalization and compatible solubility. For our system, we must design quantum dots that are both soluble in water and have high selectivity and reactivity to maleimide. Maleimide reacts under appropriate conditions with thiols to create a covalent C—S bond.[37] Conjugation between inorganic and organic units has been demonstrated using maleimide-thiol chemistry, but the approach is most commonly implemented with the maleimide functionalizing the inorganic particle and complementary cysteines positioned within the organic framework.[38-40] There are a few examples of functionalizing an inorganic particle with sulfur, either by conjugation of sulfur within the inorganic core or using a capping ligand that contains multiple thiols to maintain the sulfur interaction with the core and bind the maleimide.[41-44] The particle surface must be ligated by a molecule that both contains a binding group to attach to the particle and an additional functional group to bind to the peptoid. Cysteine has been well-studied for the synthesis of water soluble and bio-compatible QDs that interact favorably with proteins, commonly with other cystines to create a disulfide bond or via electrostatics.[45,46] Synthesis of cysteine capped CdSe has been reported extensively, with relatively mild aqueous conditions yielding well defined clusters and QDs.

Based on existing precedent, cysteine-capped CdSe (cys-CdSe) QDs were synthesized under basic conditions (pH 12) and were stored at pH 8 to limit disulfide formation that readily occurs at pH greater than 8.5.[47] Peptoid sheets and tubes were co-assembled from different proportions of monomers bearing six polar residues (N-(2-carboxyethyl)glycine) and six nonpolar residues (N-[2-(4-bromophenyl)ethyl]glycine for sheets or N-[2-(4-bromophenyl)methyl]glycine for tubes). The monomers were terminated with either a standard NH terminus or a maleimide group with the intention of creating nanosheets and nanotubes with highly tunable maleimide density for covalent attachment of QDs (**Figure 2.1a,b**). Notably, similar peptoid sheets have been demonstrated to remain stable under a large range of conditions including basic pH values up to pH 10.[23] Acidic conditions can lead to etching of QDs that can lead to shrinkage and even destabilization depending on the duration of exposure and the exact pH. For the above reasons, conjugation was performed at pH 7 with a 1 h incubation time using a 0.17 mM solution of peptoid sheets (concentration determined by individual peptoid monomers used for assembly) and a 4.2 μM QD solution. After incubation, the material was used crude to prepare the sample for analysis by electron microscopy and AFM.

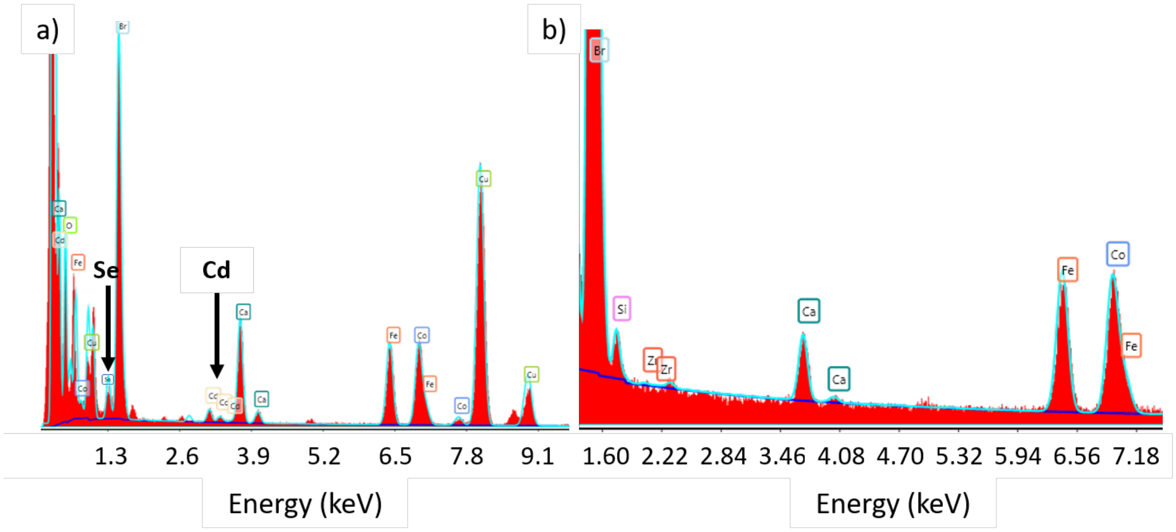

Figure 2.2. (a) EDX point scans of peptoid-CdSe QD conjugates showing Cd, Se peaks from QDs and Br peak from the peptoid. (b) Peptoid nanostructures alone with no Cd or Se peaks. Fe, Co, and Ca peaks are from impurities in the column. Cu peak from the TEM grid.

TEM was the main method of characterization, with scanning (S)TEM used to identify peptoid sheets and standard bright field methods employed to analyze particle density. TEM analysis showed a strong preference for QDs to bind to the peptoid sheets and tubes with few to no free QDs observed away from the peptoid structures (**Figure 2.3a-d**). Particle identity was confirmed using energy dispersive X-ray (EDX) analysis to identify Cd and Se in the sample (**Figure 2.2a**). No Cd or Se peaks were observed with peptoids alone (**Figure 2.2b**). The QDs remained stable with an average size of 2.82 ± 0.30 nm, but the peptoid sheets appeared to destabilize slightly under the conjugation conditions. Before conjugation, peptoid sheets averaged a few hundred nanometers in length, some as large as a micron in length, with straight, well defined edges and a rectangular shape (**Figure 2.1g,h**). After conjugation, peptoid sheets appeared to have rounded edges and were significantly smaller with an average length of 50 nm (**Figure 2.3a,b**). It is probable that the change in morphology is limited to the edges of the peptoid sheets, with the crystalline nature of the peptoids preserved throughout the majority of the sheet structure due to the primary sheet structure remaining intact, however, this cannot be confirmed under standard imaging conditions. The observed morphology changes in the peptoid sheets could be due to the increase in pH upon conjugation, interactions with the QDs themselves, or a result of imaging with an electron beam (see below for discussion following investigation by AFM).

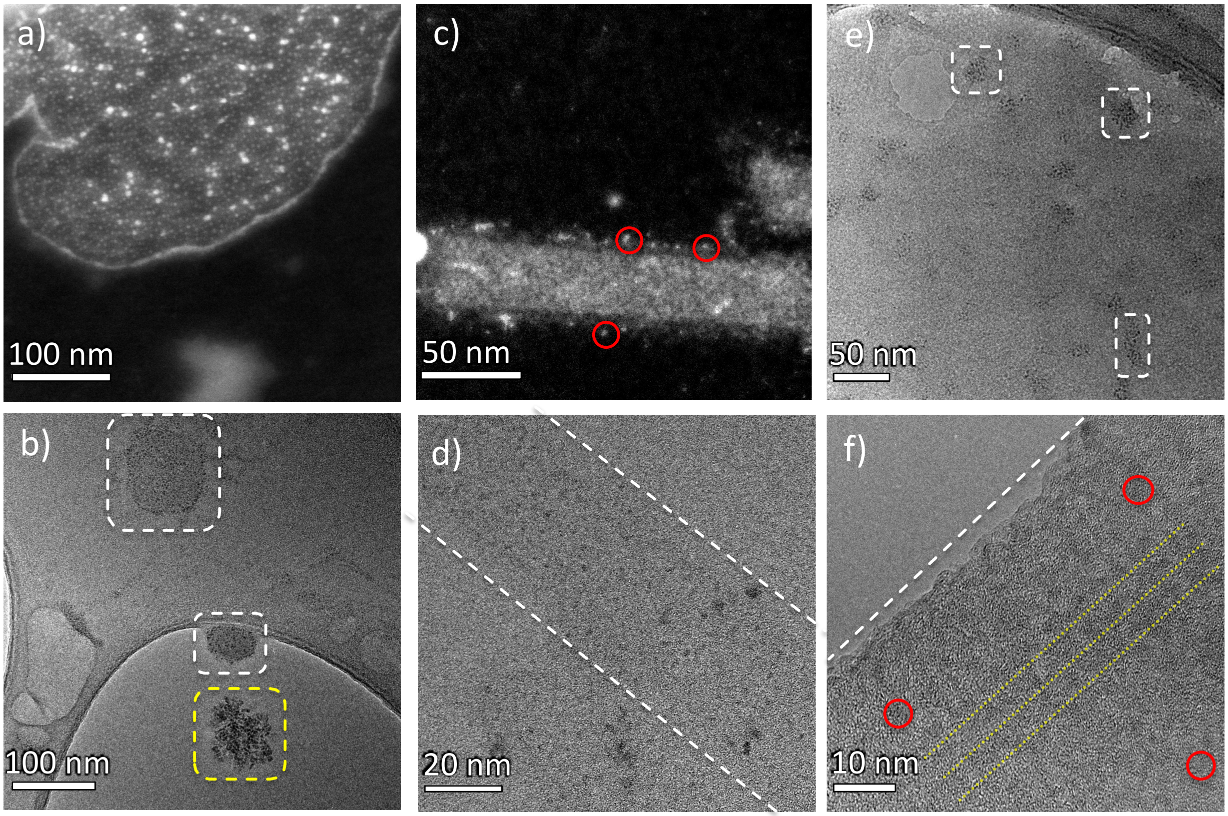

Figure 2.3. (a, b) Cys-CdSe QDs exhibit a strong preference for binding to maleimide-functionalized peptoid sheets (a) but destabilization of the sheets is seen by the smaller sheet sizes than observed in the absence of the QDs, as well as rounding of the sheet edges (b, white dashed line). (b). QD aggregates unassociated with peptoid sheets can sometimes be seen (yellow dashed line in b), recognizable by their dendritic morphologies and irregular particle distributions. (c) STEM image of peptoid tubes conjugated with CdSe QDs, seen along the tube edges (red circles). (d) Standard TEM shows that the QDs have a high preference for the tubes (white dashed lines), with uniform distribution. (e) CdSe clusters conjugated with a peptoid sheet (white dashed lines) with significant shrinkage of the sheets observed. (f) Tubes with clusters (red) exhibiting linear trends (yellow dotted lines) parallel to the tube edge (white dashed line), consistent with the interdigitated row-by-row, bi-layer structure of the peptoid tubes (**Figure 2.1c-e**).

To test the versatility of the hybrid peptoid-CdSe system, conjugation was performed with atomically precise cys-CdSe clusters characterized by a lowest energy electronic transition at 420 nm[48]. We find that CdSe clusters have reactivity comparable to that of their QD counterparts but are less robust to a variety of conditions. Conjugation was performed under standard conditions, replacing the QDs with clusters using the same total concentration (4.2 μM). Clusters showed the same strong preference for binding to the sheet surfaces (**Figure 2.3e**) and maintained their structural integrity based on their observed sizes (~2 nm). Again, the observed peptoid sheets were small and rounded after conjugation.

Peptoids have also been shown to assemble into nanotubes by changing the length of the carbon side chain in the hydrophobic region with an average nanotube being 40 nm in diameter and up to a micron in length (**Figure 2.1a,e**). Using peptoids with the same hydrophilic monomer sequence as for the sheet forming sequence, but with a tube generating hydrophobic sequence (containing one less carbon on the side chain), conjugation was performed with both cys-CdSe QDs and clusters at pH 7. Both the clusters and QDs showed a strong preference for the peptoid tube surface. The QDs and clusters are presumably also present inside the pore of the tubes but diffusion within the tube is likely limited by the irreversible binding of maleimide. However, the tubes did not show any signs of destabilization upon conjugation with the particles, in contrast to the destabilization seen with the sheets. This high degree of stability could be due to the rigidity of the tube structure relative to the sheets and may suggest that by altering the peptoid monomer, specifically the side chains to create stiffer sheets, better sheet stability could be obtained. Interestingly, alignment of the clusters parallel to the tube edge can be seen on the tube surface (yellow dotted line, **Figure 2.3f**) consistent with the interdigitated row-by-row, bi-layer structure of the peptoid tubes (**Figure 2.3e**). The same ordering was not observed in the case of the QDs, which we suspect may be a result of their inherent polydispersity and large size (**Figure 2.3c,d**).

2.2.2 *Creating a compatible system.*

As mentioned previously, peptoid sheets should remain stable at pH values up to pH 10 but this structural robustness is reliant on peptoid sheets being adequately crystalline.[23,24] Therefore, we sought different conjugation conditions to create a compatible and reproducible system. Conjugation was performed at pH 6 with cys-CdSe QDs to emulate conditions used for long-term storage of the peptoid sheets. Under slightly acidic conditions, the sheets retained their micron size and rectangular shape but the QDs were observed to aggregate with unsuccessful conjugation as there was no observed preference for QDs to bind the peptoid sheets (**Figure 2.4**). Based on the pKa values of cysteine, operating at pH 6 likely results in a zwitterion, which may decrease QD solubility and lead to the observed aggregation.[49]

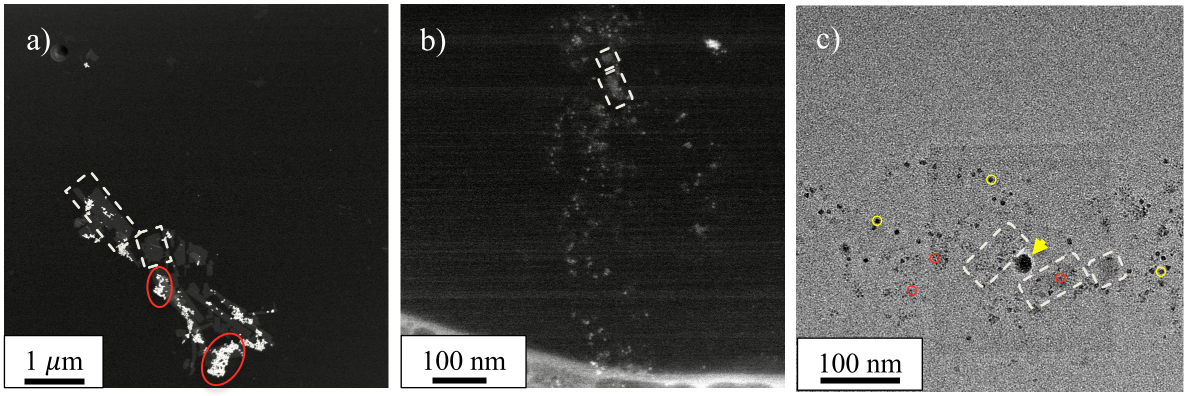

Figure 2.4. Peptoid sheets with cys-CdSe QDs with peptoids at pH 6 (a) and at pH 7 (b,c). Peptoid sheets maintain stability at pH 6 with large rectangular shape (white) but QDs become aggregated (red). At pH 7 peptoid sheets become rounded and shrunk (white) but QDs are dispersed and unaggregated (red). Larger QDs seen are an impurity from TEM sample prep (yellow) and some beam damage from STEM (yellow arrow).

A comparable bifunctional ligand to cysteine, mercaptopropionic acid (MPA) (**Figure 2.1f**, R=H), has been used in the QD literature to solubilize QDs under acidic conditions.[49-51] Additionally, MPA has a similar structure to cysteine, but without the amine substituent which should limit pH related solubility issues and be less favorable for disulfide formation.[47] CdSe QDs were synthesized with MPA as the capping ligand (MPA-CdSe) under the same conditions as cys-CdSe. After purification, the QDs were titrated with HCl, starting at pH 7, down to pH 4 while monitoring the absorbance and photoluminescence. MPA-CdSe retained their well-resolved absorption features down to pH 5.5 after which the excitonic transitions began to broaden the absorption peaks with an increase in scattering (**Figure 2.5a**). After incubation overnight at pH 6, MPA-CdSe remained stable with an average size of 2.77 ± 0.70 nm without significant etching as observed by TEM (**Figure 2.5b**).

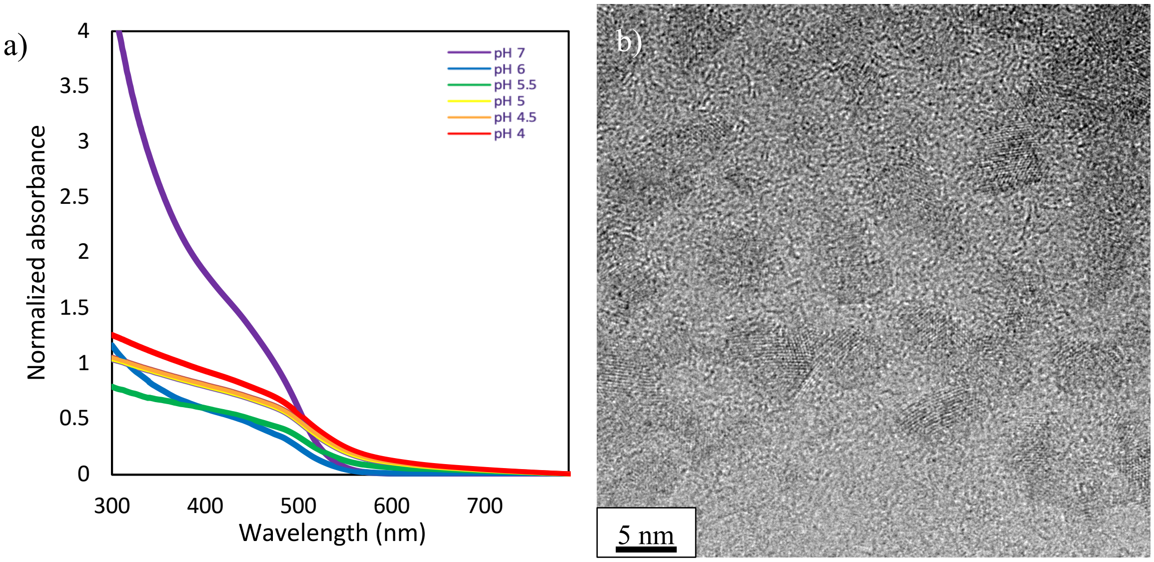

Figure 2.5. MPA-capped CdSe QDs titrated from pH 7 to 4 monitored by UV-Vis with absorption features at 444 and 494 nm maintained down to pH 5.5 (a). TEM shows further stability with minimal size change after incubation at pH 6 overnight, 2.77±0.70 nm (b). The particles show

more facets than seen with cys-CdSe, likely due to the less dense particle coverage on the TEM grid for MPA-CdSe allowing for HRTEM of the particles.

Conjugation using MPA-CdSe QDs showed a strong preference for QD association with the peptoid surface. The peptoid sheets better maintained their structure under these conditions than under those used with cys-CdSe, however, the sheets still showed rounding of their edges. This effect has two possible sources. The first is destabilization of the sheet edges due to interactions between the QDs and the peptoids exposed at the edges and due to conditions under which conjugation was performed. The second is the binding of a single QD to multiple maleimide units on the peptoid. We expect that the majority of the MPA is bound to the QD surface through thiolate ligation, with the carboxylic acid exposed to solution based on literature precedent for these systems.[52,53] However, under acidic conditions, the QD surface is likely to have some fraction of exposed thiol that is available for interaction with the maleimide on the peptoid (see below for additional analysis of the binding mechanism using NMR spectroscopy). Additionally, the peptoid monomers contain a relatively long hydrophilic region, enabling QDs bound near the edge of the peptoid sheet to interact with a MPA on the opposite peptoid surface and cause rounding of the edge.

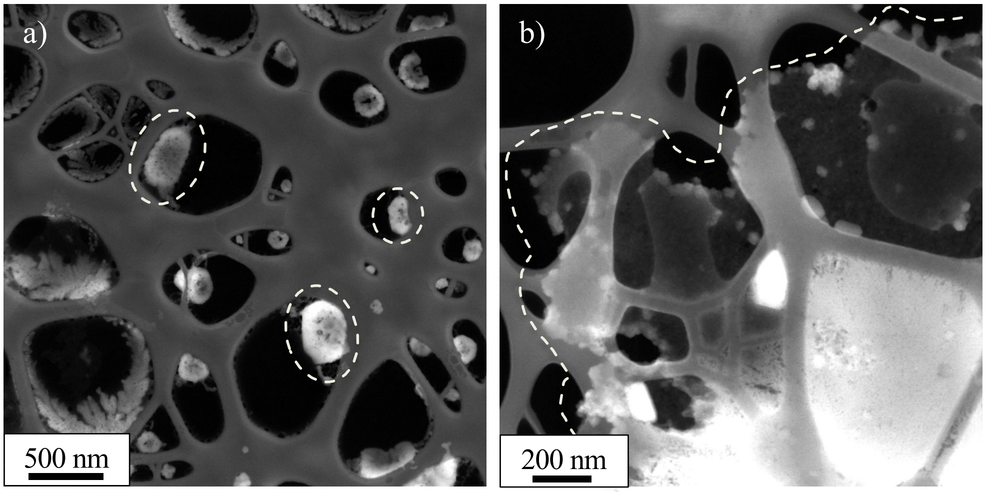

Figure 2.6. Peptoid sheets (10% MA) incubated at pH 7 overnight. Sheets (white) show shrunken size and rounded shape (a) and large amorphous areas of organic material with rounded edges (b).

The extent of destabilization has been seen to vary between samples and appears to be somewhat correlated with pH changes and maleimide concentration. Peptoid sheets are typically assembled under acidic conditions and stored around pH 2-3, but they have been shown to be stable to and assemble at pH 10.[23,24] Conjugation is performed at pH 6-7 to promote QD stability and this increase in pH could contribute to changes in peptoid sheet morphology. The peptoids used in this system were incubated overnight at pH 7 without QDs present and were observed to maintain their larger sheet size but still showed rounding of the edges (**Figure 2.6**). Conjugation above pH 8 still shows a strong preference for QD binding to the peptoid surface, but further evolution of the peptoid morphology to fibril like structures is observed (**Figure 2.7**). Incidentally, the percentage of peptoids displaying a maleimide group is controlled at the time of sheet assembly by the relative concentrations of -maleimide and -COOH terminated monomers. Sheets containing 20, 50, and 80% maleimide-terminated monomers were conjugated with MPA-CdSe QDs and analyzed. The peptoid sheets retained their generally rectangular structure in the case of 20% maleimide but begin to show large amorphous structures at 50 and 80% maleimide. Maleimide is known to be highly selective for thiols under a range of conditions, but it has been shown to react with amines over thiols at pH values above 7.5.[54] If the solution used for conjugation becomes too basic or there are local concentrations at the peptoid sheet surface of higher pH, the maleimide could react internally with the peptoids themselves to create an amorphous structure.

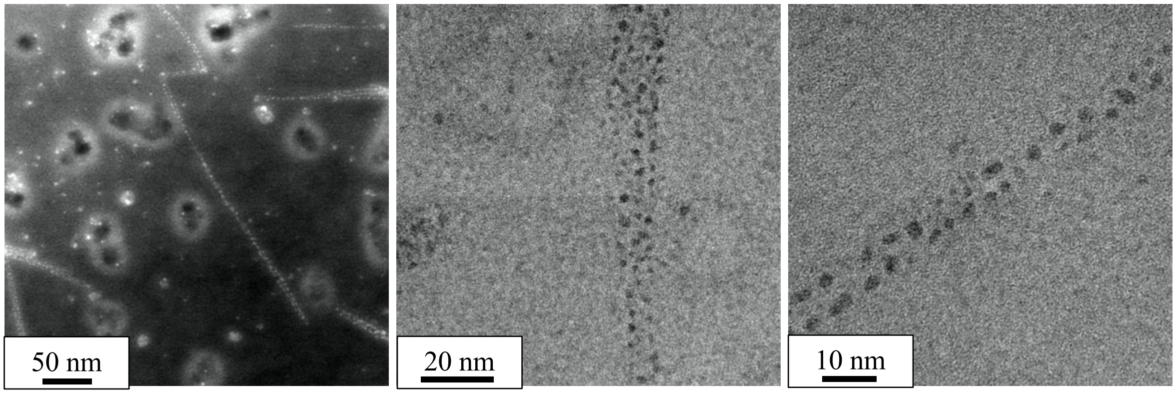

Figure 2.7. Conjugation under basic conditions between QDs and peptoid sheets leading to fibril peptoid morphologies.

Another possible source of the reduced size and rounded edges is the interaction of the QD-functionalized peptoid sheets with the electron beam during TEM imaging. Although, if this is a source of the effect, it must occur upon initial exposure, because no evolution of peptoid sheet morphology was observed during prolonged TEM imaging. To determine if the electron beam contributed to destabilization, AFM was performed on two identical TEM grids containing QD-functionalized methoxy ether peptoid sheets (structure discussed below), one exposed to the electron beam and one not. AFM images of the beam exposed grid showed slightly shrunken and rounded flake-like sheets with QDs attached, consistent with the TEM images (**Figure 2.8a-d**). In contrast, the unexposed grid contained large peptoid sheets with straighter edges and QDs on the surface (**Figure 2.8e-f**). However, ruling out the presence of some amount of smaller, rounded sheets is not possible give the inherent limit on the field of view for which the range of heights is small enough to resolve ~4 nm high sheets by AFM.

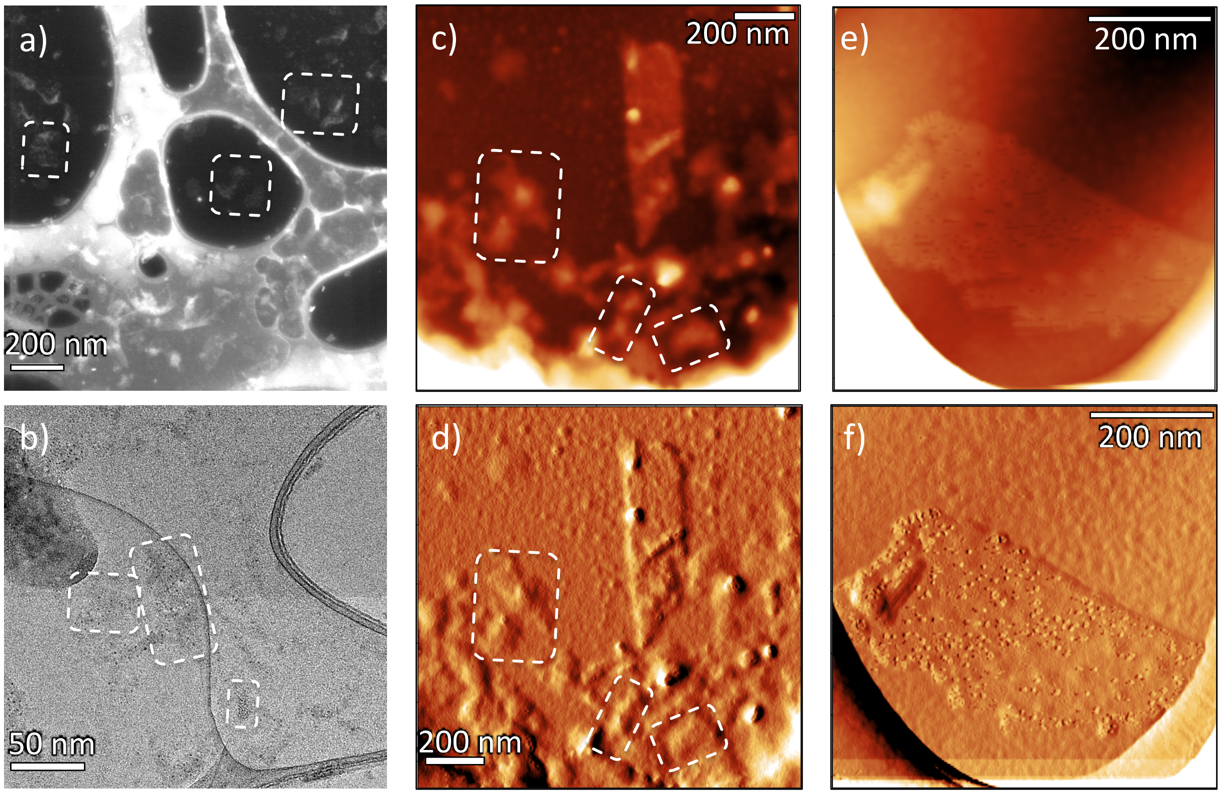

Figure 2.8. (a,b) 10% maleimide-functionalized peptoid sheets with MPA QDs on a lacey carbon grid imaged via STEM (a) and bright field TEM (b) showing small, flake-like peptoid sheet-QD conjugates (white dashed line). (c,d) The same TEM grid imaged via AFM showing primarily small peptoid sheet-QD conjugates with a few large, intact sheets. (e,f) AFM of 10 % maleimide-functionalized peptoid sheets with MPA QDs on a lacey carbon grid without exposure to the electron beam, indicating conjugation between QDs and peptoids occurs without destabilization or shrinkage of the peptoid sheets and, thus, electron-beam exposure is the source of these effects.

Further supporting the hypothesis that the electron beam is at least a partial source of destabilization, electron beam exposure of maleimide-free peptoid sheets in the presence of unbound QDs did not result in destabilization; rather well defined, rectangular peptoid sheets were observed in TEM (**Figure 2.9**). The lack of degradation upon prolonged exposure and the observation of fracturing only when the QDs were bound to the peptoid surface suggests that, while degradation induced by the electron beam may occur important, it may not be the only source of destabilization. Rather the chemical effects associated with QD-peptoid conjugation and discussed above may also be a factor. Overall, peptoid destabilization appears to be an unavoidable result of conjugation with nanoparticles but can be minimized by remaining at moderate maleimide concentrations, operating under acidic conditions, and limiting electron beam exposure.

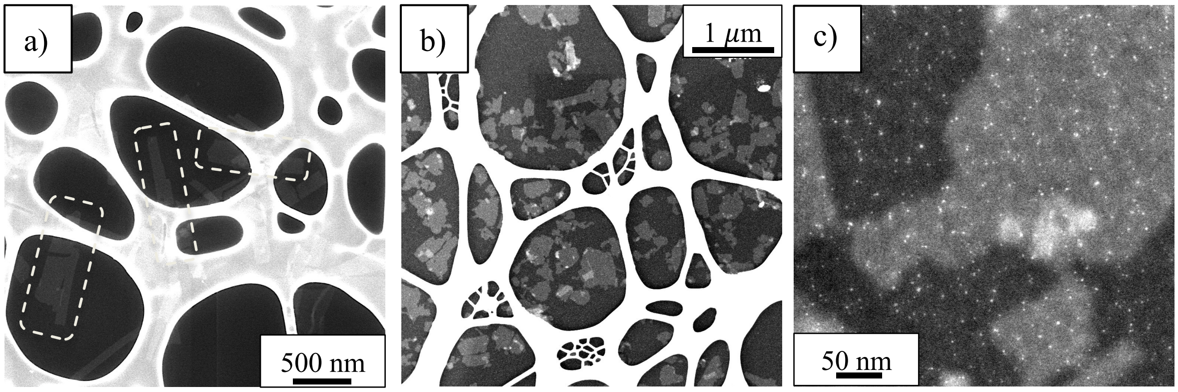

Figure 2.9. (a) Unstained peptoid sheets (white dashed line) without QDs present showing well defined edges and no destabilization from the electron beam or vacuum. (b,c) Peptoid sheets with unbound QDs present showing maintained sheet integrity under the electron beam and vacuum.

2.2.3 *CdSe conjugation density depends on maleimide content.*

To test our ability to control QD density on the peptoid sheets, experiments were performed with cystine-capped CdSe QDs at pH 7 with peptoid sheets assembled from 10, 50, and 100% maleimide-terminated peptoids. Strong preference for QDs to bind to the peptoid sheets with few QDs found independent of the sheets was observed for all cases (**Figure 2.10**). Moreover, all samples also showed complete saturation of the peptoid surfaces with QDs with no QD density difference regardless of the degree of maleimide functionalization. To understand this result, consider the impact of carboxylic acid groups in the peptoid monomers. With the standard di-block peptoid monomer, the hydrophilic region is functionalized with carboxylic acid sidechains to ensure good solubility. Carboxylates are known to act as effective ligands to stabilize QD surfaces.[52,53] We postulate that the observed saturation of the peptoid sheet surface is likely due to non-specific interactions of the QDs with the carboxylates from both the maleimide-functionalized and non-functionalized peptoid monomers. To block these non-specific interactions and maintain the hydrophilicity of the peptoid monomer, we replaced the carboxylic acid side chains with methoxy ethers (**Figure 2.11a**), thus ensuring the only favorable peptoid-QD interaction occurs via the maleimide terminus.

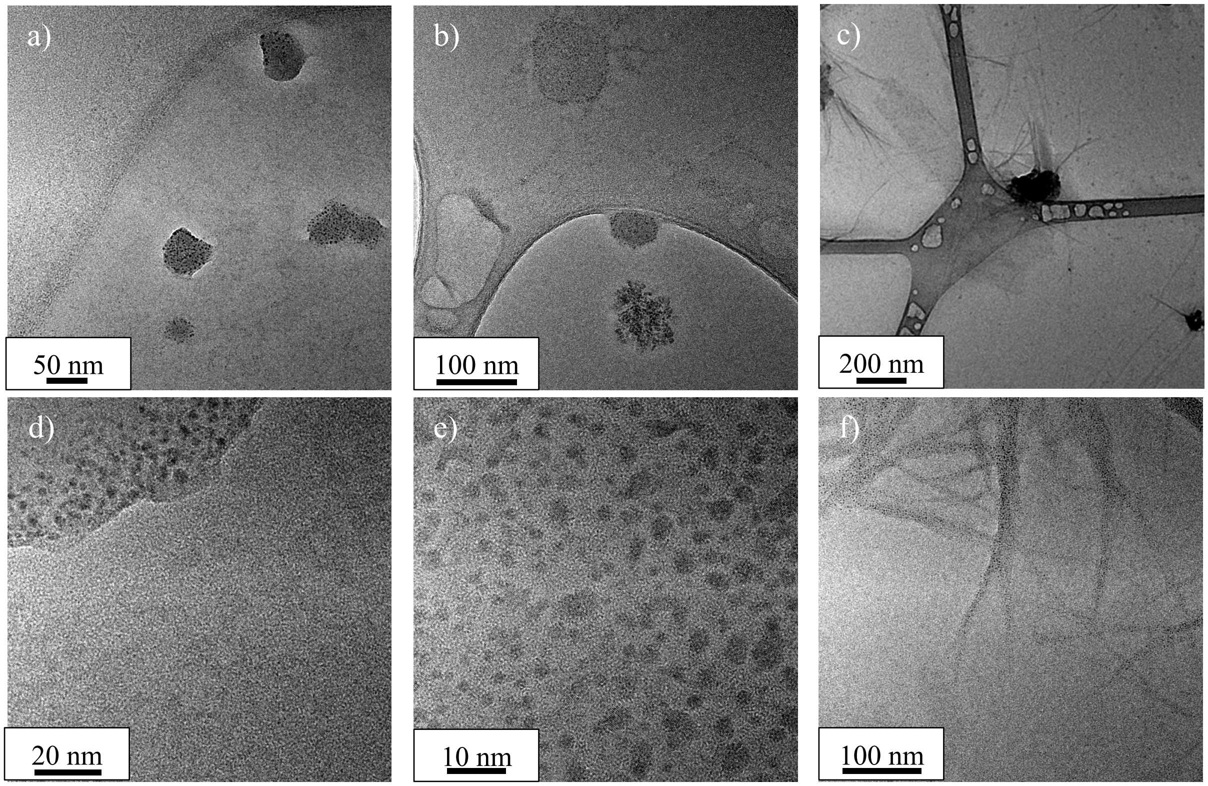

Figure 2.10. Peptoid sheets conjugated with cys-CdSe at 20 (a,d), 50 (b,e) and 80% MA (c,f). No difference in particle coverage is seen between 20-80% MA. Conjugation was performed at pH 7

leading to peptoid shrinkage and rounding (a,b) and fibril like morphology (c,f). High preference for QD attachment to the peptoid was observed.

Conjugation of methoxy ether peptoid sheets and MPA-CdSe QDs was carried out at pH 6. For all samples, MPA-CdSe QDs are seen to maintain their crystallinity, but are etched slightly, exhibiting an average loss of 1 nm in diameter after conjugation (**Figure 2.11b-i**). Particle shrinkage likely arises from a combination of the mildly acidic conjugation conditions and interactions with the peptoids, as minimal etching is observed when the particles are incubated at pH 6 alone. Successful peptoid functionalization via maleimide was observed for maleimide concentrations ranging from 2.5 to 20%. The particle size after conjugation averaged 1.78 nm with a uniform distribution across the peptoid sheets except in the case of 2.5% maleimide functionalization, for which QDs were localized at the edges of the peptoid sheets. For maleimide functionalization of 5 to 20%, the percent coverage by area of QDs on the sheets — determined by measuring the diameter of every QD on a fixed area of peptoid sheet and dividing the total QD area by the total peptoid area — tracks with the percent maleimide functionalization for a given sample (**Table 2.1**).

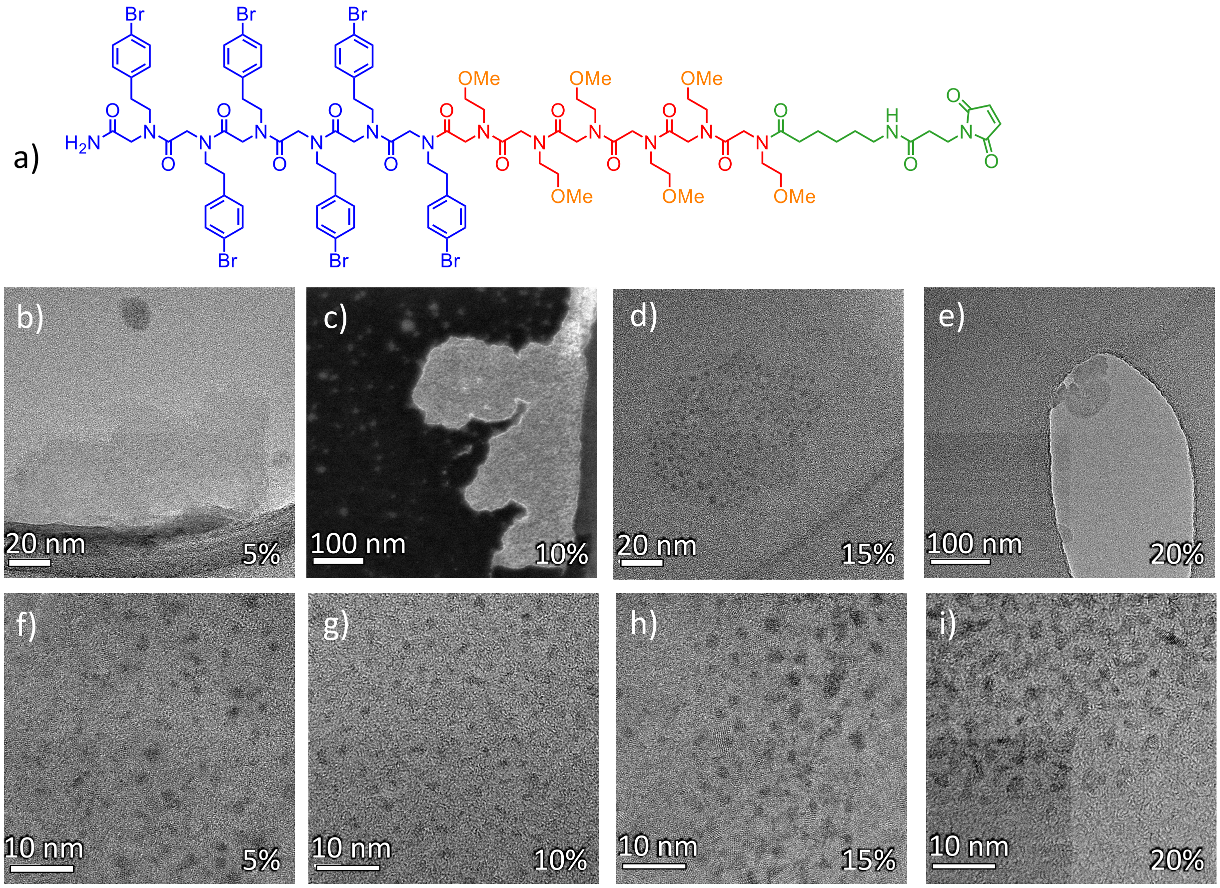

Figure 2.11. (a) Methoxy ether functionalized peptoid monomer used to eliminate non-specific QD interactions with carboxylic groups of the peptoid backbone. (b-i) Conjugation of MPA QDs with methoxy ether peptoid sheets at pH 6 with (b,f) 5, (c,g) 10, (d,h) 15, and (e,i) 20% maleimide. Peptoid sheets still show some rounding and destabilization (d,e) but maintain a larger sheet size at pH 6 than at pH 7 (compare b and c to Fig. 2b). QD density on the sheet surface increases with maleimide percentage with slight etching of the QDs from 2.82 ± 0.30 nm to 1.78 ± 0.28 nm (f-i).

The maleimide location is generally thought to be random within the orderly packed peptoid rows in each sheet and should be equally distributed on the top and bottom faces. Thus, QDs should exhibit similar coverages on both sides. The calculated percent coverage assumes that all QDs are on one side of the peptoid sheet (i.e. – only one side is in focus in an image), but, due to the relatively low contrast of carbon-based materials in bright field TEM and the sheets only being 3-4 nm thick, it is likely that QDs from both sides of the peptoid sheets are seen in a given image. To determine whether this is the case, AFM analysis was repeated using 10% maleimide-functionalized sheets for which TEM imaging gave 11.1% coverage. AFM imaging gave a QD coverage of only 2.9% (**Table 2.1**). If one assumes TEM images record QDs on both sides of the sheet, then this value represents more than half the coverage determined by TEM, appearing to confirm that the peptoid sheets are thin enough to see QDs above and below the sheet in the TEM. However, because tip convolution associated with the AFM measurement of particles renders the apparent size to be significantly larger in AFM then TEM — 3.0 nm vs. 1.9 nm, the calculated number densities are more disparate giving values per face of the peptoid sheet that differ by a factor of 5 (2 x10^{-2} QDs/nm^{-2} vs 0.4 x10^{-2} QDs/nm^{-2}). The difference in QD number density seen in TEM vs AFM may be the result of batch to batch variability, as the sheets used to determine the coverage by TEM came from a different synthesis run than those used for in AFM. For a more direct comparison, a sample of QD conjugated peptoids with 10% maleimide was first analyzed by TEM with AFM analysis immediately following on the same sample. The QD number density was more consistent between these two samples, differing only by a factor of two with the TEM and AFM measurements giving values of 0.9 x10^{-2} QDs/nm^{2} vs 0.4 x10^{-2} QDs/nm^{2}, respectively.

Table 2.1. Analysis of MPA CdSe QDs on peptoid sheets of varying maleimide percentage. The percent of sheet surface covered assumes all QDs seen are on one side of the peptoid sheet. QD diameter was determined via TEM analysis for all samples and percent coverage was determined via TEM analysis unless otherwise noted.

Percent maleimide	**Percent covered**	**QD average diameter (nm)**	**QD/peptoid area (x10^{-2} nm^{-2})**	**QD/peptoid area (x10^{-2} nm^{-2}) accounting for both sides of peptoid**
5%	5.9	1.8	3.2	1.6
10% (sample A)	11.1	1.9	4.0	2.0
10% (sample B)	12.6	3.0	1.8	0.9
10% (sample B via AFM)	2.9	3.0	0.4	N/A
15%	14.7	1.7	6.2	3.1
20%	19.6	1.8	7.6	3.8

2.2.4 *Determining the binding mechanism.*

The specificity of MPA-CdSe QD binding to maleimide-functionalized peptoid sheets could be driven by multiple binding mechanisms. The QDs could adhere to the surface either via electrostatic interactions or via the formation of a covalent bond to a moiety on the peptoid surface. Thiolate groups are known to bind more strongly than carboxylate groups to a CdSe QD surface, suggesting that a reasonable model for the QD surface is majority thiolate coordination to the CdSe with the carboxylic acid moiety exposed to the bulk solution.[52,53] However, if the thiol is required for maleimide conjugation, we would then expect that ligand rearrangement to a carboxylate-bound form is a requirement. Moreover, while a preference for carboxylate binding to the surface over that of thiolate is improbable at high pH values, at lower (neutral or acidic) pH values the thiolate protonates and binds much less strongly to the CdSe surface.[55] Also, conjugation may occur via direct bond formation between the chalcogenide core of the particle and the maleimide, as has been observed in the case of MoS_2 and WS_2.[41] To test for covalent bond formation and isolate the mechanism of biding, we performed several control experiments and followed them by TEM and/or NMR spectroscopy as described below.

First, to confirm that the observed specificity was dependent on covalent bond formation with the maleimide, as suggested by the density dependence study, conjugation of MPA-CdSe QDs was attempted at pH 6 with methoxy ether substituted peptoid sheets containing 0% maleimide. TEM analysis showed QDs randomly scattered across the sample with slight aggregation (**Figure 2.12a**), as is common in images of the QDs alone (**Figure 2.3b**, yellow dashed line). Peptoid sheets retained their micron size with well-defined, straight edges and with little to no QD coverage for any given sheet. The lack of QD binding to the peptoid sheets with 0% maleimide incorporation confirms that the preference for the peptoid surface is driven by covalent bond formation with the maleimide and is not due to electrostatic interactions between the sheet surface and the QDs.

To determine the role of thiol in the conjugation, CdSe QDs were synthesized with s-methyl-l-cysteine as the capping ligand to create a carboxylate-capped surface and a solution-facing thioether group. Additionally, previous studies of the binding of cysteine to CdSe clusters show that while the amine can help stabilize the particle surface, it will not act as the primary binding group.[56] Conjugation was performed under standard conditions with 20% maleimide peptoid sheets and analyzed via TEM. As with the 0% maleimide case, no preference was seen for the QDs to adhere to the peptoid surface; QDs were randomly scattered across the sample (**Figure 2.12b**). The unsuccessful conjugation indicates that the thiol is vital for maleimide conjugation. Additionally, it suggests that the sulfur is not reactive in its thioether form and therefore it is unlikely that, with the standard thiolate capped QDs, the sulfur maintains its interaction with the QD surface, but, instead, binds to the maleimide.

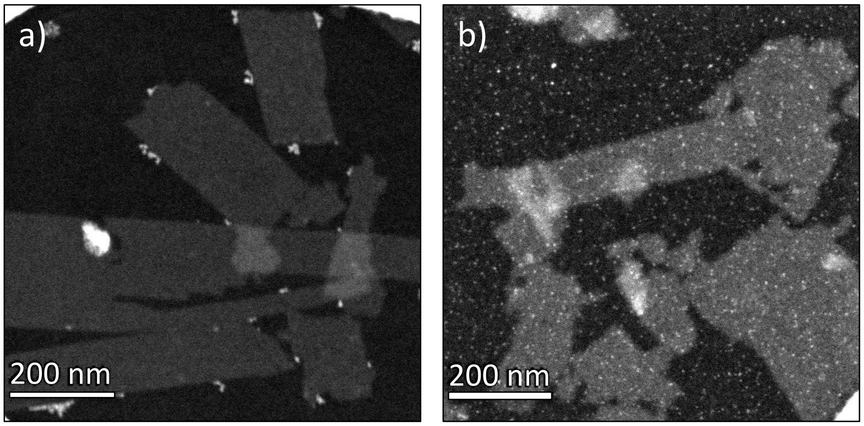

Figure 2.12. Unsuccessful conjugation of peptoid sheets with 0% maleimide with MPA-QDs at pH 6 (a). Sheets maintain defined rectangular shape and 500 nm length with the QDs aggregated randomly, likely due to drying effects on grid. 20% maleimide sheets with S-methyl-L-cysteine capped QDs and pH 6 (b) showing QDs randomly scattered around the grid with no localization of QDs to the peptoid sheet.

These results support our hypothesis that ligand rearrangement is occurring under the conjugation conditions or that, based on the relative equilibria, some fraction of the ligands are already present on the QD surface in their carboxylate bound form.[57] To further test for ligand rearrangement, $Cd(MPA)_2$ was synthesized from $CdSO_4$ and doubly deprotonated MPA and isolated for titration with a maleimide-containing small molecule surrogate, 6-maliemidohexanoic acid (EMCA), for analysis by ^1H NMR spectroscopy. Prior to EMCA addition, two triplets associated with the MPA are observed at 2.56 and 2.90 ppm with a small impurity seen at 3.02 ppm that later disappears due to overlap with shifting MPA peaks. With EMCA addition, the peaks associated with the carbon chain grow in as expected with the resonance associated with the methylene alpha to the carboxylate shifting the most from 2.36 ppm to 2.19 ppm (**Figure 2.13**). The singlet associated with the double bond in the maleimide ring is not observed, instead growth of three peaks at 2.75, 3.31, and 4.07 ppm is observed, consistent with binding of the maleimide with the sulfur of the MPA. The expected MPA-maleimide complex should only show two new peaks, but the maleimide ring is well known to be more stable in an open configuration after conjugation with a thiol.[58] Overnight incubation of the solution led to the disappearance of the peak at 4.07 ppm, a concomitant sharpening of the peak at 2.75 ppm, and an increase in the integrated area of the peak at 3.31 ppm. This indicates that initial mixing produces both the open and closed ring conformations, with the open ring species being the majority after incubating overnight.

At low EMCA concentration in solution, the peaks associated with MPA protons did not shift upon binding of the maleimide, implying that no ligand rearrangement is needed to bind the maleimide, and thus supporting the presence of a population of MPA bound via the -COOH.[57] At higher EMCA concentrations, peaks shift down field and a distinct set of triplets grow in at 2.54 ppm and 2.92 ppm. The new triplet is both distinct from the original peak and associated with maleimide binding as it integrates 1:1 relative to EMCA in solution. This observation supports MPA rearrangement in the Cd-complex to bind via the -COOH and free the sulfur for maleimide binding. The downfield shift of the remaining $Cd(MPA)_2$ peaks is likely a result of some mixed ligand environment as rearrangement occurs. The addition of maleimide to $Cd(MPA)_2$ confirms the ability of MPA to form a stable covalent bond with maleimide and supports a population of MPA bound via -COOH to cadmium. While the data suggests rearrangement is plausible, conjugation with the peptoid nanostructures was done with a low enough maleimide percentage that it is unlikely rearrangement occurs at the particle surface the MPA peaks didn't begin to shift until over 2 eq. maleimide per $Cd(MPA)_2$. Instead, the open maleimide sites are likely filled by the fraction of MPA bound via the carboxylate.

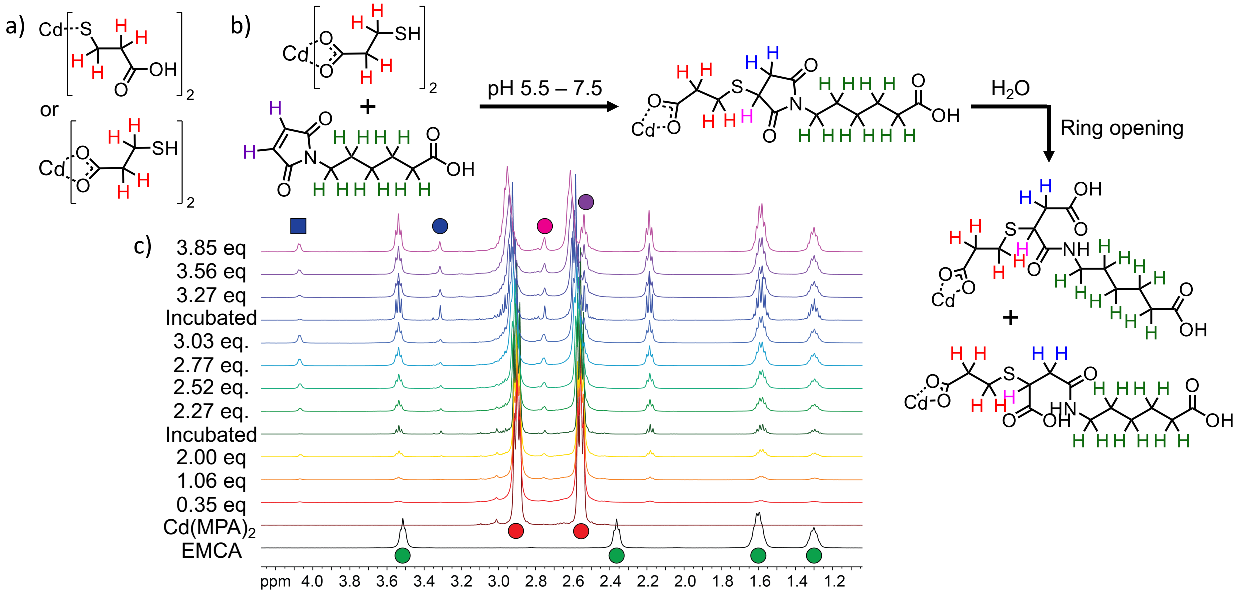

Figure 2.13. (a) Potential binding modes for MPA to cadmium and (b) the proposed reaction mechanism for Cd(MPA)$_2$ with maleimide. (c) NMR analysis of Cd(MPA)$_2$ with increasing EMCA. EMCA carbon peaks grow in as expected (green), MPA begins to shift after 2 eq. EMCA (red), with a new triplet growing in (purple), and new peaks seen from successful conjugation (blue and pink). The mix of open and closed ring maleimide conformations can be seen with two different hydrogen species representing the hydrogens beta to the sulfur (blue circle and square, respectively).

2.3 CONCLUSIONS

Understanding the interactions between peptoid structures and inorganic particles is key in designing compatible components and engineering hybrid composites with unique functionality. In this work, we have demonstrated the use of peptoid materials to template the arrangement of CdSe nanoparticles with control over the QD density based on the percentage of maleimide incorporated into the peptoid structure. We demonstrated the generality of the conjugation by using both peptoid sheets and peptoid tubes and using both CdSe QDs and atomically precise CdSe clusters. By tuning both the organic and inorganic subunits of the hybrid assembly, we have gained insight into the stability and compatibility of the two components and have identified conditions under which we can tune the QD number density. Furthermore, we have identified the operative mechanism governing the selectivity of the particles for the peptoid surfaces with a subset of MPA bound via the carboxylate to the CdSe surface, which allows for direct interaction of the sulfur with the maleimide. By understanding the design principles required to create hybrid assemblies between peptoid structures and CdSe particles, we have established a platform for expanding the structural and compositional diversity of these systems. Finally, we demonstrated exceptionally mild conditions for nucleating CdSe nanoparticles and their compatibility with peptoid structures, opening the possibility of using peptoids as a nucleation platform for CdSe nanomaterials.

2.4 EXPERIMENTAL METHODS

2.4.1 *Materials*

All reactions and manipulations were conducted in ambient air in a well-ventilated fume hood using or on a benchtop as appropriate unless otherwise indicated. Acetonitrile (99.8%), cadmium sulfate 8/3-hydrate (>99%), L-cysteine (97%), ethyl alcohol (≥99.5%), hydrochloric acid (37%), 3-mercaptopropionic acid (≥99%), S-methyl-L-cysteine (>97%), selenium powder (99.5%), sodium hydroxide (98%), sodium sulfite (>98%) were purchased from Sigma-Aldrich Chemical Co. and used without further purification. 6-maleimidohexanoic acid (>98%) was purchased from Fisher Scientific and used without further purification. Deuterated chloroform (99.8%) and deuterium oxide (99.96%) were purchased from Cambridge Isotope Labs and used without further purification. 18.2 MΩ water was collected from an EMD Millipore purification system. All peptoids were synthesized and assembled by Bin Cai and Tengyue Jian at PNNL. UV−vis spectra were collected on a Cary 5000 spectrophotometer from Agilent.

2.4.2 *Synthesis of cysteine CdSe magic-sized clusters*

The synthesis of CdSe MSCs is adapted from Park et al.[48] In a reflux setup, 12 mL water, 0.239 g Na_sSO_3, and 0.05 g Se powder were heated to 90 °C with stirring. The reaction was allowed to proceed in the dark overnight at a constant temperature at 90°C. The resulting Se^{2-} solution must be kept at 90 °C until use and must be used within two days for best results. In a separate Erlenmeyer flask, 10 mL of water and 1.754 g of L-cysteine (7.3 mmol) were mixed and then NaOH (1 M) was added until the solution reached pH 12 (~15 mL). This was necessary to ensure complete deprotonation of the cysteine. It is important to add NaOH to the cysteine suspension to limit disulfide bond formation. The solution was stirred for 30 min until clear and colorless. A 5 mL Cd^{2+} solution (0.15 M, 0.75 mmol) was added dropwise and stirred for an additional 30 min until clear. The resulting solution was then adjusted to a total volume of 46.25 mL. After the solutions were prepared, 3.75 mL of Se^{2-} solution (0.188 mmol) was rapidly injected into the flask containing Cd-cys. The solution was stirred in the dark for 1 h and then was heated to 40 °C for 20 min. The reaction progress was monitored via UV-Vis absorption spectroscopy. After cluster growth was complete, the clusters were precipitated using acetonitrile (2:1, acetonitrile: cluster solution) and the clusters were allowed to settle out of solution overnight. This was done to avoid cluster aggregation induced by centrifugation. The colorless supernatant was then decanted and the pellet containing the clusters was resuspended in 10 mL of water. The clusters were stored in the dark. The purified clusters showed an absorption maximum at 420 nm and had a diameter of 2.23 ± 0.32 nm by TEM analysis.

2.4.3 *Synthesis of cysteine CdSe quantum dots*

In a 3-neck 50 mL round bottom flask equipped with a condenser, thermowell, and rubber septum, 25 mL of crude CdSe MSCs are added without further dilution or ligand addition. The solution was heated to reflux (100 °C) and the reaction was monitored via UV-Vis spectroscopy. The reaction was allowed to proceed for 4 h until the spectra no longer changed and a final peak maximum around 540 nm was achieved. The resulting material was purified via precipitation using acetonitrile (2:1 acetonitrile:QD solution), followed by centrifugation for 10 min at 7600 rpm. The resulting QD pellet was suspended in minimal water (10 mL) and the precipitation process was repeated. The material was centrifuged for a total of 5 cycles and the final pellet was suspended in water and stored in the dark at room temperature. The resulting QDs showed an absorption maximum at 540 nm with a diameter of 2.90 ± 0.62 nm by TEM analysis.

2.4.4 *Synthesis of mercaptopropionic acid CdSe nanoparticles*

Mercaptopropionic acid (MPA) capped CdSe particles were synthesized using the same conditions as above. In the synthesis of the starting MSCs MPA was substituted for cysteine. The resulting MSCs were purified using 5 cycles of precipitation and redissolution cycles with ethanol. The resulting MPA-capped MSCs showed a broad absorption at 420 nm with TEM showing a large amount of aggregation upon drying. MPA QDs were synthesized as detailed above and purified using ethanol as the precipitant. The resulting QDs showed two broad absorption features at 445 and 475 nm with a diameter of 2.77 ± 0.70 nm by TEM analysis.

2.4.5 *Synthesis of S-methyl-L-cysteine CdSe nanoparticles*

The procedure was the same as described above but substituting S-methyl-L-cysteine (SMLC) for cysteine in the synthesis of the starting MSCs. Instead of isolating MSCs after 4 h, the reaction was continued overnight. The resulting particles were QDs with no MCSs isolated. The SMLC particles were purified using both ethanol and acetonitrile for a total of 10 cycles of precipitation and redissolution. The final material showed an absorption maximum at 592 nm and diameter of 2.96 ± 0.86 nm by TEM analysis.

2.4.6 *General procedure for peptoid-CdSe conjugation*

The peptoids were made and assembled following the procedure by Jin et al.[23,24] Conjugation was performed at room temperature by diluting the peptoid stock solution (10 μL, 1 mM) in 45 μL of water (pH 6) followed by the addition of 5 μL of CdSe QDs (2.5×10^{14} particles/mL, pH 6). The sample was allowed to incubate for at least 1 h. Imaging was then performed with no further purification or dilution.

2.4.7 *TEM sample preparation and analysis*

TEM images were collected on a FEI Tecnai G2 F20 microscope operated at 200 keV for bright field and STEM. Samples were prepared by drop-casting 5 μL of sample onto a suspended ultrathin carbon film on lacey carbon support film, 400 mesh, copper grids purchased from Ted Pella Inc. The samples were allowed to dry in air for 20 min on the grids before dabbing excess water off and drying completely on a Kimwipe. Before imaging, the grids were placed in a desiccator for at least 2 h. TEM analysis was performed using manual analysis with the help of ImageJ. Histograms, average sizes, and standard deviations for CdSe QDs and MSCs were obtained by manual analysis of over 200 particles per sample. EDX analysis was performed at PNNL by Guomin Zhu on an aberration-corrected Titan 80-300™ scanning/transmission electron microscope (S/TEM).

2.4.8 *AFM analysis*

AFM images were collected on an Asylum Research Cypher in non-contact mode with SNL-10 probes purchased from Bruker AFM Probes. AFM was performed on fixed TEM grids prepared as detailed above.

2.4.9 *NMR analysis*

^{1}H NMR spectra were recorded on 300 and 500 MHz Bruker Advance spectrometers. All samples were run with 10 scans and a delay time of 30 s. $Cd(MPA)_2$ was prepared following the standard CdSe procedure detailed above, stopping prior to the addition of the Se^{2-} solution. The $Cd(MPA)_2$ complex was isolated via precipitation and redissolution with EtOH (3:1, EtOH : Cd-MPA solution) and centrifugation. The complex was resuspended in water and lightly purified with two additional precipitation and redissolution cycles and the resulting pellet was then fully dried. The complex was resuspended in minimal D_2O and purity was confirmed via ^{1}H NMR spectroscopy. 6-maliemidohexanoic (EMCA) was used as a maleimide source for binding with MPA. 0.25 equivalents of EMCA relative to $Cd(MPA)_2$ was added via solid addition to avoid solubility issues with EMCA in water. After every addition the tube was shaken well for 30 s prior to analysis. Up to about 4 equiv. of EMCA was added to solution before the saturation point of EMCA in water was reached.

2.5 REFERENCES

1. G. Kickelbick, *Hybrid Materials*, 2014, **1**, 39-51.
2. P. A. Gabrys, L. Z. Zornberg and R. J. Macfarlane, *Small*, 2019, **15**, 1805424.
3. Y. Tian, J. R. Lhermitte, L. Bai, T. Vo, H. L. Xin, H. Li, R. Li, M. Fukuto, K. G. Yager, J. S. Kahn, Y. Xiong, B. Minevich, S. K. Kumar and O. Gang, *Nature Mater.*, 2020, **19**, 789–796.
4. J. Snyder, K. Livi and J. Erlebacher, *Adv. Funct. Mater.*, 2013, **23**, 5494–5501.

5. C. Pigliacelli, R. Sánchez-Fernández, M. D. García, C. Peinador and E. Pazos, *Chem. Commun.*, 2020, **56**, 8000–8014.
6. H. Sai, K. W. Tan, K. Hur, E. Asenath-Smith, R. Hovden, Y. Jiang, M. Riccio, D. A. Muller, V. Elser, L. A. Estroff, S. M. Gruner and U. Wiesner, *Science*, 2013, **341**, 530–534.
7. R. M. Dorin, H. Sai and U. Wiesner, *Chem. Mater.*, 2014, **26**, 339–347.
8. X. Zhang, P. Tanner, A. Graff, C. G. Palivan and W. Meier, *J. Polym. Sci. A*, 2012, **50**, 2293–2318.
9. E. J. Robertson, A. Battigelli, C. Proulx, R. V. Mannige, T. K. Haxton, L. Yun, S. Whitelam and R. N. Zuckermann, *Acc. Chem. Res.*, 2016, **49**, 379–389.
10. V. Castelletto, J. Seitsonen, K. M. Tewari, A. Hasan, R. M. Edkins, J. Ruokolainen, L. M. Pandey, I. W. Hamley and K. H. A. Lau, *ACS Macro Lett.*, 2020, **9**, 494–499.
11. C. A. Mirkin, R. L. Letsinger and R. C. Mucic, *Nature*, 1996, **382**, 607-609.
12. R. J. Macfarlane, B. Lee, H. D. Hill, A. J. Senesi, S. Seifert and C. A. Mirkin, *Proc. Natl. Acad. Sci.*, 2009, **106**, 10493–10498.
13. Z.-G. Wang and B. Ding, *Adv. Mater.*, 2013, **25**, 3905–3914.
14. Y. Zhang, F. Lu, K. G. Yager, D. van der Lelie and O. Gang, *Nature Nanotechnol.*, 2013, **8**, 865–872.
15. J. Sun and R. N. Zuckermann, *ACS Nano*, 2013, **7**, 4715–4732.
16. N. A. Merrill, F. Yan, H. Jin, P. Mu, C.-L. Chen and M. R. Knecht, *Nanoscale*, 2018, **10**, 12445–12452.
17. F. Jiao, X. Wu, T. Jian, S. Zhang, H. Jin, P. He, C.-L. Chen and J. J. De Yoreo, *Angew. Chem. Int. Ed.*, 2019, **58**, 12223–12230.
18. F. Yan, L. Liu, T. R. Walsh, Y. Gong, P. Z. El-Khoury, Y. Zhang, Z. Zhu, J. J. De Yoreo, M. H. Engelhard, X. Zhang and C.-L. Chen, *Nature Commun.*, 2018, **9**, 2327.
19. R. Li, A. Smolyakova, G. Maayan and J. D. Rimer, *Chem. Mater.*, 2017, **29**, 9536–9546.
20. C.-L. Chen, J. Qi, R. N. Zuckermann and J. J. DeYoreo, *J. Am. Chem. Soc.*, 2011, **133**, 5214–5217.
21. X. Ma, S. Zhang, F. Jiao, C. J. Newcomb, Y. Zhang, A. Prakash, Z. Liao, M. D. Baer, C. J. Mundy, J. Pfaendtner, A. Noy, C.-L. Chen and J. J. De Yoreo, *Nature Mater.*, 2017, **16**, 767–774.
22. C.-L Chen, J. H. Qi, J. H. Tao, R. N. Zuckermann, J. J. DeYoreo, *Sci. Rep.,* 2014, **4**, 6266.
23. H. Jin, F. Jiao, M. D. Daily, Y. Chen, F. Yan, Y.-H. Ding, X. Zhang, E. J. Robertson, M. D. Baer and C.-L. Chen, *Nature Commun.*, 2016, **7**, 12252.
24. H. Jin, Y.-H. Ding, M. Wang, Y. Song, Z. Liao, C. J. Newcomb, X. Wu, X.-Q. Tang, Z. Li, Y. Lin, F. Yan, T. Jian, P. Mu and C.-L. Chen, *Nature Commun.*, 2018, **9**, 270.
25. R. V. Mannige, T. K. Haxton, C. Proulx, E. J. Robertson, A. Battigelli, G. L. Butterfoss, R. N. Zuckermann and S. Whitelam, *Nature*, 2015, **526**, 415–420.
26. S. Jin, Y. Hu, Z. Gu, L. Liu and H.-C. Wu, *Journal of Nanomaterials*, 2011, **2011**, 1–13.
27. S. Mazumder, R. Dey, M. K. Mitra, S. Mukherjee and G. C. Das, *Journal of Nanomaterials*, 2009, **2009**, 1–17.
28. L. Zhao, L. Hu and X. Fang, *Advanced Functional Materials*, 2012, **22**, 1551–1566.
29. W. Liu, H. S. Choi, J. P. Zimmer, E. Tanaka, J. V. Frangioni and M. Bawendi, *J. Am. Chem. Soc.*, 2007, **129**, 14530–14531.
30. V. H. Chu, T. H. Lien Nghiem, T. H. Le, D. Lam Vu, H. Nhung Tran and T. K. Lien Vu, *Adv. Nat. Sci: Nanosci. Nanotechnol.*, 2012, **3**, 025017.
31. Y. Yuan and M. Krüger, *Polymers*, 2012, **4**, 1–19.

32. A. N. Beecher, X. Yang, J. H. Palmer, A. L. LaGrassa, P. Juhas, S. J. L. Billinge and J. S. Owen, *J. Am. Chem. Soc.*, 2014, **136**, 10645–10653.
33. M. B. Teunis, S. Dolai and R. Sardar, *Langmuir*, 2014, **30**, 7851–7858.
34. A. M. Smith and S. Nie, *Acc Chem Res*, 2010, **43**, 190–200.
35. A. P. Alivisatos, *Science*, 1996, **271**, 933–937.
36. B. M. Cossairt, P. Juhas, S. Billinge and J. S. Owen, *J Phys Chem Lett*, 2011, **2**, 3075–3080.
37. P. Akkapeddi, S.-A. Azizi, A. M. Freedy, P. M. S. D. Cal, P. M. P. Gois and G. J. L. Bernardes, *Chem. Sci.*, 2016, **7**, 2954–2963.
38. E. Oh, K. Susumu, J. B. Blanco-Canosa, I. L. Medintz, P. E. Dawson and H. Mattoussi, *Small*, 2010, **6**, 1273–1278.
39. C. Srinivasan, J. Lee, F. Papadimitrakopoulos, L. K. Silbart, M. Zhao and D. J. Burgess, *Mol. Ther.*, 2006, **14**, 192–201.
40. B. Zang, J. Yu, C. Liu, J. Wang, H. Han, P. Zhang, D. Shi, *RSC Adv.,* 2016, **6**, 50119–50127.
41. Vera-Hidalgo, E. Giovanelli, C. Navío and E. M. Pérez, *J. Am. Chem. Soc.*, 2019, **141**, 3767–3771.
42. W. J. Parak, D. Gerion, D. Zanchet, A. S. Woerz, T. Pellegrino, C. Micheel, S. C. Williams, M. Seitz, R. E. Bruehl, Z. Bryant, C. Bustamante, C. R. Bertozzi and A. P. Alivisatos, *Chem. Mater.*, 2002, **14**, 2113–2119.
43. A. Banerjee, C. Grazon, B. Nadal, T. Pons, Y. Krishnan and B. Dubertret, *Bioconjugate Chem.*, 2015, **26**, 1582–1589.
44. E. Giovanelli, E. Muro, G. Sitbon, M. Hanafi, T. Pons, B. Dubertret and N. Lequeux, *Langmuir*, 2012, **28**, 15177–15184.
45. W. Liu, H. S. Choi, J. P. Zimmer, E. Tanaka, J. V. Frangioni and M. Bawendi, *J. Am. Chem. Soc.*, 2007, **129**, 14530–14531.
46. G. Hosseinzadeh, A. Maghari, S. M. F. Farniya, A. H. Keihan and A. A. Moosavi-Movahedi, *Mater. Sci. Eng. C*, 2017, **77**, 836–845.
47. D. Bermejo-Velasco, A. Azémar, O. P. Oommen, J. Hilborn and O. P. Varghese, *Biomacromolecules*, 2019, **20**, 1412–1420.
48. Y.-S. Park, A. Dmytruk, I. Dmitruk, A. Kasuya, Y. Okamoto, N. Kaji, M. Tokeshi and Y. Baba, *J. Phys. Chem. C*, 2010, **114**, 18834–18840.
49. Y. Nosaka, N. Ohta, T. Fukuyama and N. Fujii, *J. Coll. Interf. Sci.*, 1993, **155**, 23–29.
50. D. Lawless, S. Kapoor and D. Meisel, *J. Phys. Chem.*, 1995, **99**, 10329–10335.
51. W. C. W. Chan and S. Nie, *Science*, 1998, **281**, 2016–2018.
52. R. R. Knauf, J. C. Lennox and J. L. Dempsey, *Chem. Mater.*, 2016, **28**, 4762–4770.
53. N. C. Anderson, M. P. Hendricks, J. J. Choi and J. S. Owen, *J. Am. Chem. Soc.*, 2013, **135**, 18536–18548.
54. C. F. Brewer and J. P. Riehm, *Anal. Biochem.*, 1967, **18**, 248–255.
55. I. Chambrier, C. Banerjee, S. Remiro-Buenamañana, Y. Chao, A. N. Cammidge and M. Bochmann, *Inorg. Chem.*, 2015, **54**, 7368–7380.
56. T. Kurihara, Y. Noda and K. Takegoshi, *ACS Omega*, 2019, **4**, 3476–3483.
57. J. Zhang, F. Tian, M. Zhang, T. Li, X. Kong, Y. Zhou and N. A. Kotov, *Nanoscale Horiz.*, 2019, **4**, 1416–1424.
58. S. D. Fontaine, R. Reid, L. Robinson, G. W. Ashley and D. V. Santi, *Bioconjugate Chem.*, 2015, **26**, 145–152.

Chapter 3. IMPACT OF NANOPARTICLE SIZE AND SURFACE CHEMISTRY ON PEPTOID SELF-ASSEMBLY

Adapted with permission from the American Chemical Society. Copyright 2022 ACS Nano.

3.1 INTRODUCTION

Hierarchically organized nanomaterials are often generated by mimicking natural systems wherein functional properties emerge due to order and organization across multiple length scales.[1-3] To predictively generate such materials, we must understand and systematize the atomic-level interactions that lead to organization of the functional building blocks across length scales. Traditionally, hybrid organic-inorganic nanomaterials are synthesized via bottom-up assembly or through templated assembly on a scaffold.[4-7] In these approaches, organic molecules, which are typically DNA, peptides (or peptoids), polymers, or small multitopic organic molecules, are used as the structure-directing elements with covalent and non-covalent interactions dictating the possible assembly outcomes.[1,5-13] These interactions are dependent on the sequence used and can often be controlled using pH, temperature, electrolytes, solvent, and/or pendant groups.[14-18] When inorganic nanoparticles act as the driving force for assembly, the generated structures are often a result of particle packing and drying effects. In these systems, the structures can be tuned through size, surface chemistry, ligand packing or morphology of the nanoparticles but frequently lack precision and are often limited to 2D films or layered structures of the aforementioned films.[19-23] Exquisite 3D hybrid structures have been achieved bottom-up using hydrogen bonding interactions of complimentary DNA strands to precisely control nanoparticle locations relative to one of another size or composition.[11-13] However, these systems are limited to assembly in aqueous conditions due to the stability of DNA, thus limiting the types of nanoparticles that can be used without significant surface modification. Coupling nanoparticles to information-rich linkers that are stable in organic media would offer the possibility of accessing new hybrid materials with unique functionality. Assemblies in organic media have been explored, typically with self-assembling polymers as the structure-directing agent and show promise to not only organize nanoparticles but to do in a predictive manner to access a wide variety of morphologies.[24-27]

Peptoids, or poly-N-substituted glycines, are peptide analogs that are functionalized on the nitrogen rather than carbon in the backbone sequence.[28-30] Through functionalization of the nitrogen, the monomers can be made soluble in a wide range of solvents, including organics, and the hydrogen-bonding interactions that often dominate secondary structure in peptides are absent.[28-30] Without hydrogen bonding, the structure can be tuned by the sequence of the peptoid monomer through side chain/side chain and side chain/backbone interactions. Peptoids have been shown to self-assemble into a variety of structures, most notably tubes, sheets, and helices.[31-35] Di-block peptoids containing a hydrophobic region and hydrophilic region are common self-assembling sequences that assemble in a mixed solvent system (1:1, water: organic solvent). In these systems, the slow evaporation of the organic solvent (initially used to solubilize the peptoid) acts as the driving force for assembly.[31,32] As the organic solvent evaporates, the environment becomes less favorable for the hydrophobic domain, resulting in a stacking effect where the peptoids interdigitate to form a bilayer structure with hydrophilic residues on the surface (**Scheme 3.1. a**).[33,36,37]

The resulting peptoid structures have been explored as a function of sequence length, hydrophobicity, end group functionality, pH, temperature, and as templates for nucleation and assembly of nanoparticles.[9,31,32,38-44] In previous work, we utilized peptoids as a scaffold for assembly of hybrid nanomaterials through post-synthetic addition of complimentary nanoparticles to pre-formed sheets and tubes to decorate the surface via a covalent linkage.[41] Specifically, we assembled CdSe nanoparticles onto peptoid tubes and sheets using a non-reversible thiol-maleimide click reaction that generates a covalent linkage between the nanoparticles and the assembled peptoid macrostructure. This approach allowed for control over the nanoparticle density as a function of the peptoid side-chain composition. Inorganic species have also been directly appended to the hydrophilic end of the peptoid monomers during the initial solid-phase synthesis, creating a hybrid peptoid monomer that can, in principle, then be assembled into larger-scale structures.[39] In this work, we demonstrate the versatility of a related approach by using peptoid monomers as ligands on quantum dots (QDs) to tune assembly pathways bottom up, with the final hybrid structures being a function of QD concentration, surface chemistry, and size.

CdSe and CdS QDs were attached to peptoid monomers to study the impact of these different pendant groups on assembly. The peptoid monomers contained six hydrophobic residues (N-[2-(4-bromophenyl)ethyl]glycine, Nbrpe$_6$Dig) and were terminated with a carboxylic acid (**Scheme 3.1b**). This relatively short chain peptoid was chosen for its structural simplicity, diverse solubility properties, and limited steric bulk. A carboxylic acid group was chosen as the binding moiety due to the reversibility of the interaction with the QD surface, allowing for attachment through a facile carboxylic acid - carboxylate ligand exchange reaction.[45] Furthermore, the dynamic interaction between the QD and the peptoid monomer provides a mechanism for the system to reach equilibrium and reduce the heterogeneity in the number of peptoids bound to a given QD. By starting with QDs capped with carboxylate ligands, we estimate an approximate equilibrium constant for the ligand exchange with peptoid of one.[45] For the QD composition, CdSe and CdS were chosen due to the depth of existing literature for these materials in diverse solvents, as well as the well-developed knowledge on ligand exchange and binding affinities for many different systems.[45-48] Cadmium chalcogenides are known to be relatively stable in water without significant surface modification.[46] Using QDs as pendant groups on the peptoids allows for straightforward modification of the peptoids without drastically modifying the synthetic chemistry or reactivity. This allows for a systematic study into how the pendant groups' size, hydrophobicity, and concentration alter the assembly process. This method further allows for a single peptoid sequence to provide access to a variety of structures without having to design a new sequence and introduces driving forces for assembly not accessible with peptoids alone.

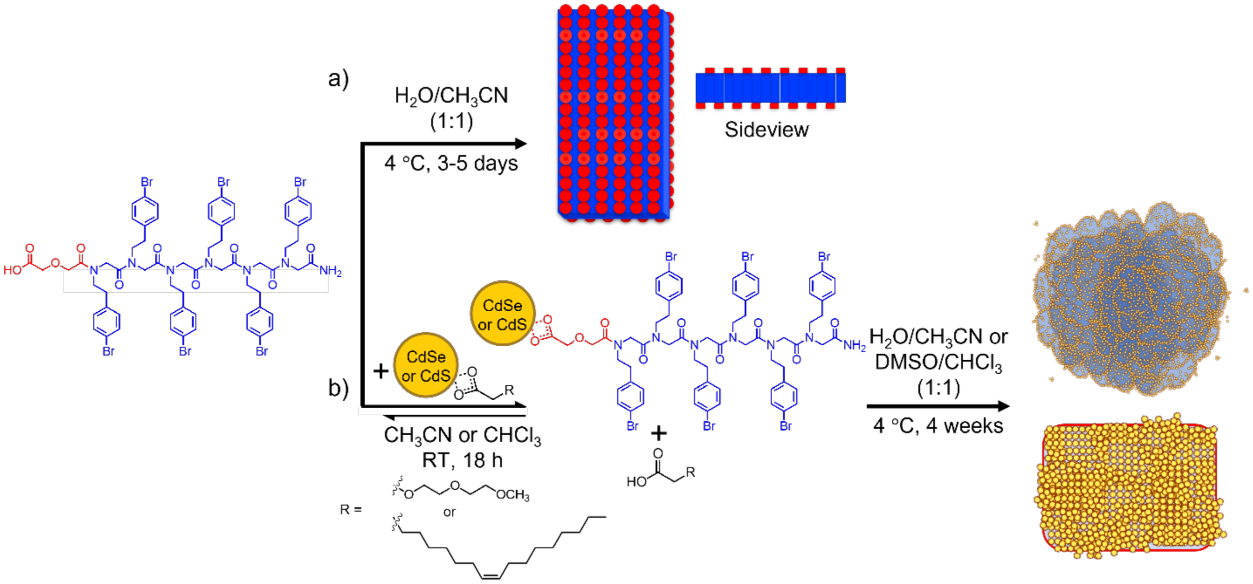

Scheme 3.1. General conditions for carboxylic acid (red)-terminated peptoid (blue) for sheet formation (a) and ligand exchange onto QDs (yellow) for hybrid sheet formation (b).

3.2 RESULTS AND DISCUSSION

3.2.1 *Peptoid and hybrid material assembly as a function of the peptoid monomer:QD ratio.*

To study assembly in a range of solvents, CdSe QDs (2.4 nm) were synthesized with 2-[2-(2-methoxyethoxy)ethoxy]acetic acid (MEEAA) to generate QDs with a wide solubility range in both aqueous and organic solutions. Peptoid monomers were added to the QDs in varying concentrations (0.3-20 eq. of peptoid monomers per QD) and incubated for 18 h in MeCN. Incubation for 18 h allowed the system to reach equilibrium and resulted in a partial ligand exchange, as evidenced by ^{1}H NMR (**Figure 3.1**). After 18 h, water was added to the solution to initiate the assembly process. This solution was allowed to assemble at 4 °C for up to 4 weeks via slow evaporation of MeCN. Ex situ transmission electron microscopy (TEM) was the primary characterization mode, with scanning TEM (STEM) and bright field (BF) to identify the microstructures and nanostructures, respectively. The assembly process was tracked by taking aliquots from the reaction solution and preparing TEM grids. Initial samples were taken prior to the addition of water (0 h) to determine if any assembly occurred without anti-solvent addition. Image timepoints for the assemblies were taken relative to anti-solvent addition at 1 h, 24 h, 4-5 d, 2 w, and 4 w.

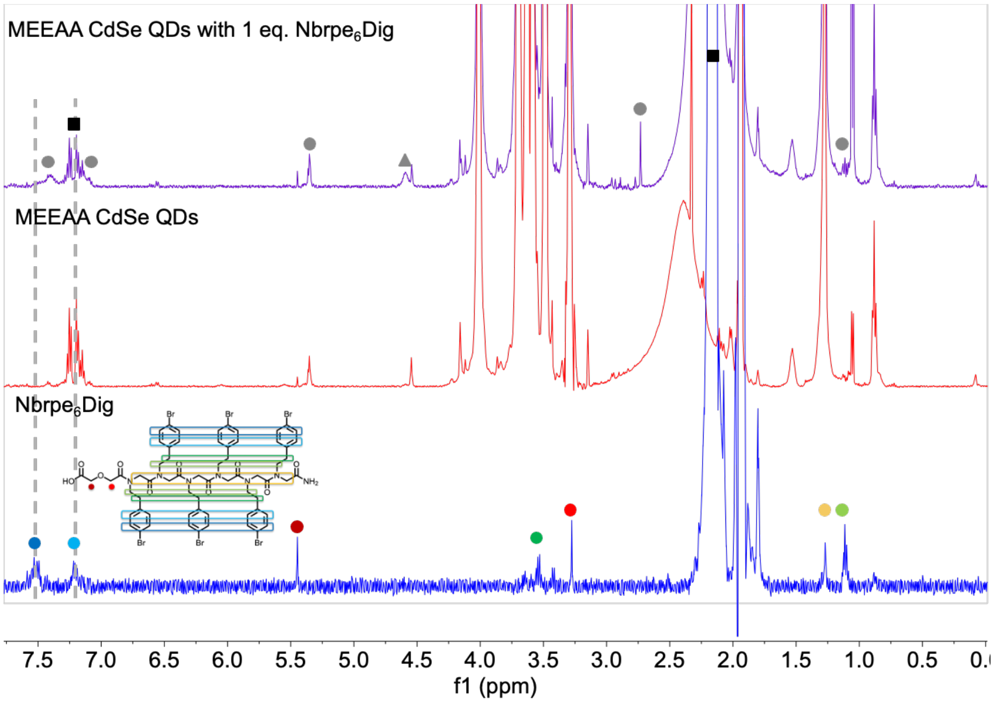

Figure 3.1. ^{1}H NMR spectra of Nbrpe$_6$Dig alone (blue), MEEAA CdSe QDs (red), and MEEAA CdSe QDs with 20 eq. of Nbrpe$_6$Dig (purple) in CD$_3$CN. The MEEAA region of the spectra do

not show any change (shifting or sharpening), indicating no significant change in free vs bound MEEAA present (left). Peptoid peaks are visible when mixed with CdSe QDs (grey) but hard to distinguish from peaks already present in the QD sample. Notably, an upfield shift is observed for the aryl peaks (7.21 ppm to 7.120 ppm and 7.51 ppm to 7.41 ppm) and broadening of a singlet assigned to protons near the -COOH binding group (4.59 ppm, triangle). This singlet does not overlap with either singlet from the peptoid alone (3.28 and 5.45 ppm), again indicating a shift from the original environment. These peak shifts and broadening consistent with the peptoid interacting with or bound to the QD surface. The amount of peptoid on the surface could not be quantified due to the formation of precipitates, likely containing both QD and peptoid. Solvent peaks are denoted by black squares.

Peptoid assembly was first tracked in the absence of QDs to gain a baseline for comparing intermediates arising during the assembly process. The peptoid partially dissolved in MeCN to produce non-uniform, elongated sheets and hollow spheres (**Figure 3.2a,b**) that evolved into large, aggregated sheets (2.9 $\pm$ 0.7 μm) and dense spheres after 18 h (**Figure 3.3a**). The spherical structures were assigned as micelles due to their dense nature and small size (20.9 $\pm$ 4.1 nm). Water addition solubilized the peptoid, facilitating rearrangement into small sheets (~100 nm) with an increase in micelle size (135 $\pm$ 36.4 nm) over 24 h (**Figure 3.3b,c**).The micelles remained present, but underwent a gradual decrease in size until complete disappearance after 5 days, while sheets continued to grow until rectangular sheets with straight edges were observed at the 4 week mark (**Figure 3.3e**).

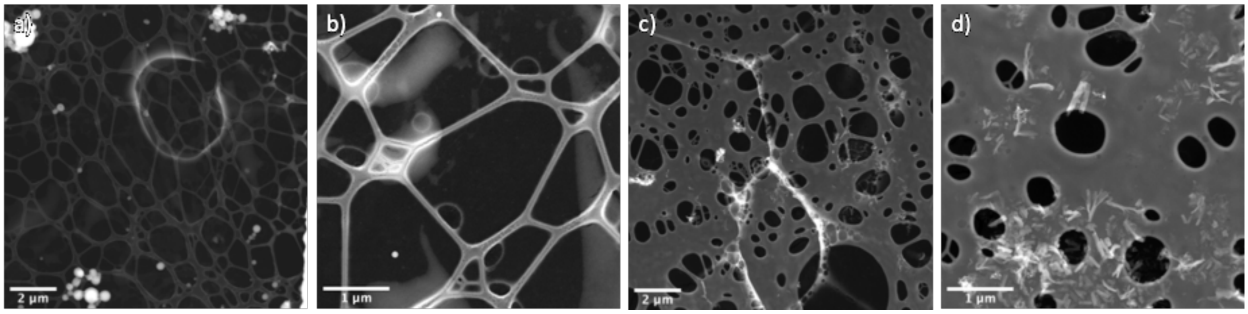

Figure 3.2. Nbrpe$_6$Dig immediately after sonication acetonitrile resulting in amorphous sheets without a defined shape, solid spheres, and smaller hollow peptoid structures (a,b). In CHCl$_3$, there was partial dissolution with long fibril-like structures containing hollow portions and small rectangular sheets (c,d).

Adding MEEAA-CdSe QDs into the peptoid solution prior to assembly produced a different final product and altered the nature of the intermediates. In MeCN, peptoid fibrils (9.94 ± 3.4 nm wide) with QDs on the edges were observed rather than large peptoid-based aggregates (**Figure 3.3f,k**). With the addition of water, the nanofibers grew slightly in width (15.0 ± 6.5 nm) in addition to the growth of peptoid micelles (30.1 ± 12.8 nm) with QDs on the edges, each in roughly equal quantities (**Figure 3.3g,l**). Upon initial imaging, the peptoid-QD spheres appeared solid in STEM mode, but prolonged imaging led to hollow structures with high contrast exteriors (**Figure 3.4a**). The production of hollow structures implies a carbon-rich center that was destroyed by the electron beam. BF mode confirmed QDs only present on the edges, thus the assignment of micelle-like peptoid structure with QDs adhering to the surface (**Figure 3.4b,c**). The CdSe QDs were seen to etch upon exposure to the peptoids and water, resulting in a diameter of 1.9 ± 0.2 nm that remained constant for up to 4 weeks in solution. After 24 h, the QD-decorated micelles were seen to arrange into a linear pattern with an average spacing of 94.4 ± 33.9 nm (**Figure 3.3h**). The distance between hybrid micelles was too large to correspond to one or two peptoid monomers, therefore we hypothesize a thin peptoid ribbon or fiber connecting the structures that was not easily seen next to the high contrast QDs (**Figure 3.3m**).

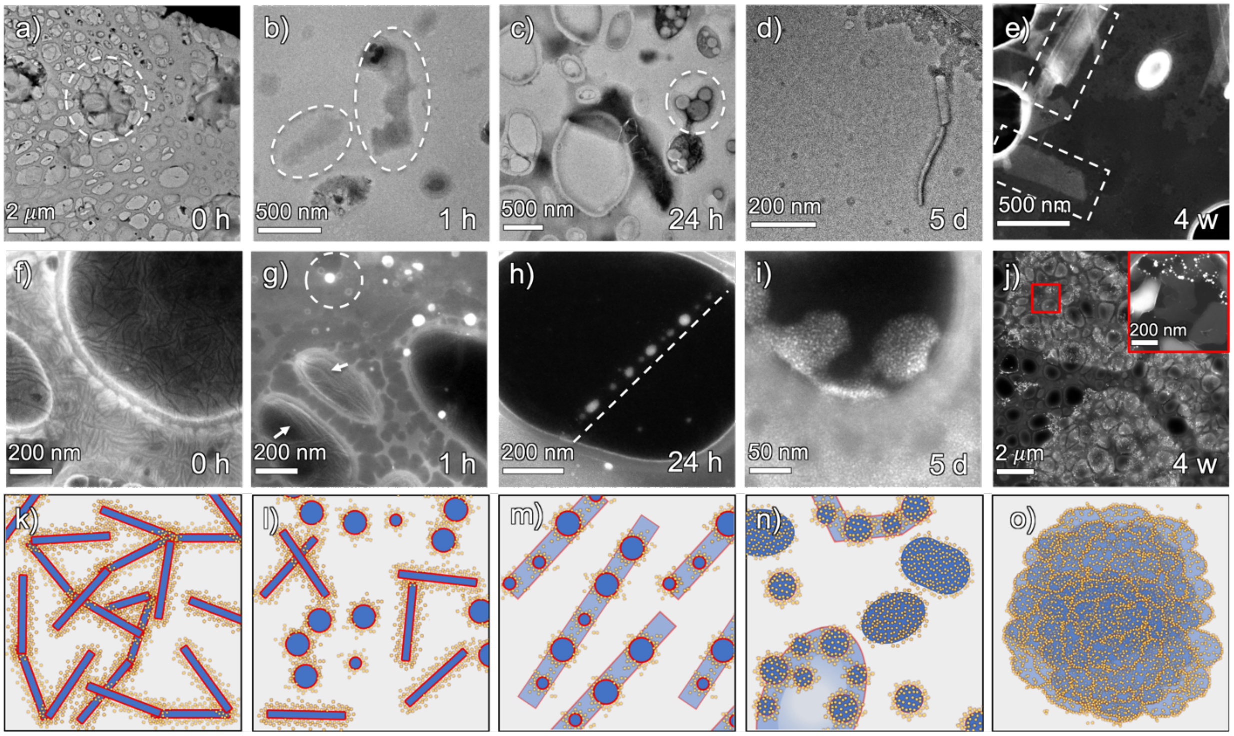

Figure 3.3. (a-e) Peptoid assembly without QDs in MeCN/H_2O. Without water, large sheet-like aggregates are seen (a) that dissolved and began to form small sheets upon water addition (b). Peptoid micelles (c) are seen throughout the assembly process as the sheets grow to be well-defined (d). After 4 weeks, large crystalline sheets are seen (e). (f-o) Assembly over time of MEEAA-CdSe QDs with 1 eq. of peptoid in MeCN/H_2O. Peptoid fibrils with QDs on the edges are seen before and right after water addition (f,g white arrows). Peptoid micelles with QDs on the edges are also observed (g) that tend towards linear arrangements (h). After 5 days, small peptoid sheets are seen with a uniform QD distribution (i). Finally, the QDs are seen to concentrate at the sheet edges and facilitate the formation of large multilayer aggregates (j) composed of many small sheets (red inset, j). Peptoid edges are denoted with white dashed lines. Schematic representation of the

assembly process (k-o) with QDs in yellow, peptoid backbone in blue, and peptoid carboxylic acid in red.

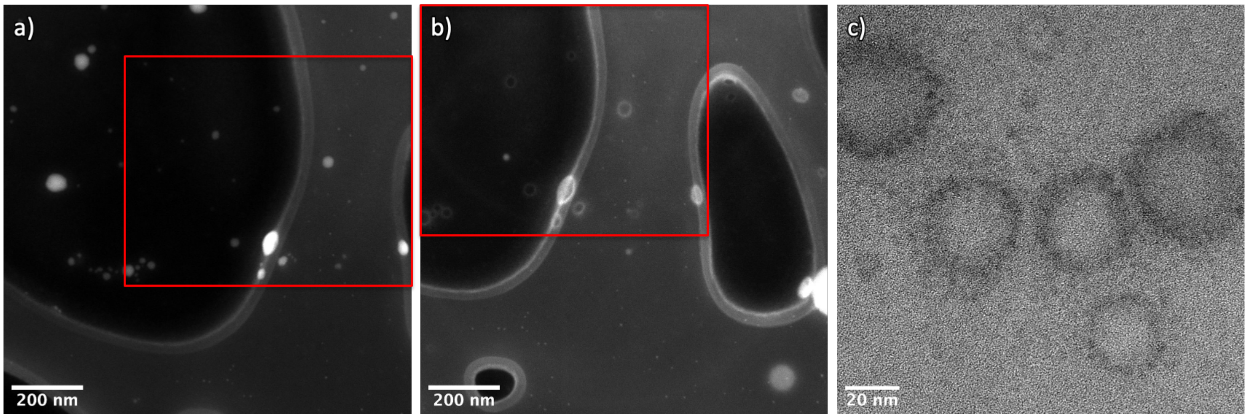

Figure 3.4. Peptoid-QD hybrid structures before (a) and after (b) prolonged imaging showed beam damage to the center of the hybrid structure. The apparent hollowing of the structure implies a non-crystalline carbon-rich center, presumably peptoid, that decomposes under the electron beam. The red box indicates the same area in both images. The BF image confirms the presence of QDs only on the exterior of the hybrid structure (c).

Over the course of 4 weeks, the connected micelles began to ripen through bending of the linear structures, generating peptoid-QD micelles that became more densely packed and smaller in size (34.8 ± 14.9 nm and 14.3 ± 6.5 nm, respectively). As the assembly progressed, small QD-covered sheets (~50 nm, **Figure 3.3i,n**) were formed, reminiscent of structures formed upon addition of QDs to pre-formed sheets.[41] These small hybrid peptoid/QD sheets eventually aggregated to form large multilayer aggregates (>5 μm, **Figure 3.3j,o**). This final hybrid multilayer material contained small QD-decorated peptoid sheets similar to those observed earlier in the assembly, but with a higher density of QDs on the edges (**Figure 3.5**). We propose that these

QDs act as linkers to bind the small sheets together into one large assembly, as has been previously observed for silica-peptoid hybrid structures.[42]

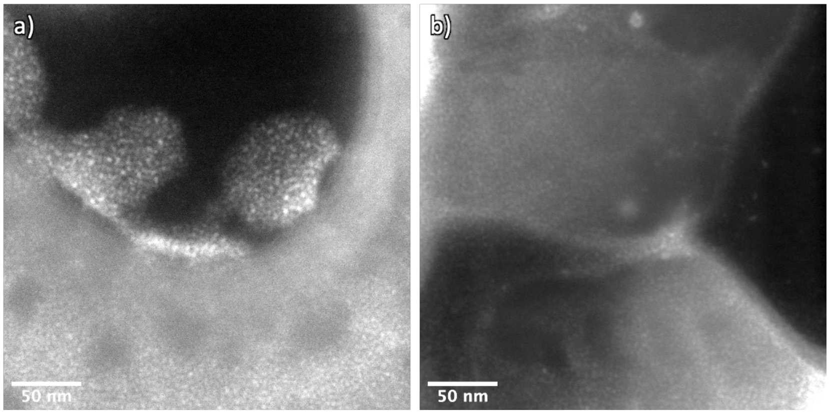

Figure 3.5. Hybrid peptoid-QD sheets when initially formed as independent sheets and after aggregation into large assemblies. Before aggregation QDs evenly cover the peptoid surface (a), and after QDs show a higher density on the edges with less uniform coverage on the rest of the sheets (b).

Dynamic light scattering (DLS) measurements of these hybrid structures and the intermediates formed during assembly confirm that the observations made by TEM are representative of what is occurring in solution (**Figure 3.6**). Upon initial assembly, DLS gives a diameter of 50.7 nm in MeCN (0 h). After addition of water, the average structure size increases to 176 nm at 1 h and 390 nm at 24 h. After 5 days, the average diameter shrinks slightly (308 nm), consistent with the bending of the linear assemblies and formation of sheets, as seen by TEM. Finally, after 4 weeks the assemblies show a diameter consistent with TEM at 2.20 μm. Overall, DLS sizes are larger than that of TEM, likely due to simplified assumptions about the form factor of the objects being measured, but support the assignment of the hybrid structures forming in solution as assembly proceeds. This series of experiments demonstrate the synthesis of hybrid materials in which both the QDs and the peptoid operate synergistically to dictate the final structure.

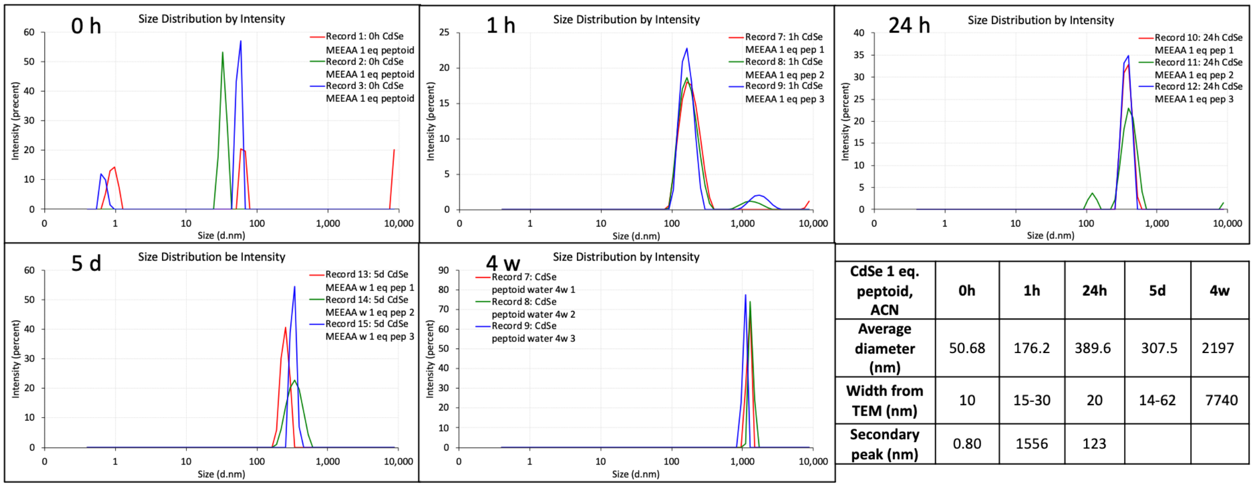

CdSe 1 eq. peptoid, ACN	0h	1h	24h	5d	4w
Average diameter (nm)	50.68	176.2	389.6	307.5	2197
Width from TEM (nm)	10	15-30	20	14-62	7740
Secondary peak (nm)	0.80	1556	123		

Figure 3.6. DLS of MEEAA-CdSe QDs with 1 eq. of Nbrpe$_6$Dig in MeCN/H$_2$O as a function of time. Assemblies are seen in solution at all time points with an increase in average diameter with time. The average diameter is larger for all time points than that of structures seen via TEM, likely due to the assumption of a perfect sphere when most structures are elongated, 2D structures.

The importance of the peptoid in this system was investigated by changing the number of peptoid monomers relative to the CdSe QD and changing the sequence of peptoid used. 20-0.33 equivalents of peptoid relative to QD were investigated while keeping the peptoid concentration constant to allow for direct comparison of assemblies at a given time point. At high peptoid equivalents, the system was seen to phase segregate with minimal integration of QDs into the structure. Here we propose the QDs are acting as defects, causing rolling and elongation of the sheets after assembly (**Figure 3.7a**). Low peptoid equivalents (5-0.33 eq.) led to assembly pathways with the same intermediates and end products as the one equivalent case described above (**Figure 3.7b-e**). However, the speed of the assembly and the stage at which different intermediates appeared varied in a consistent manner based on peptoid equivalents. In general, we observed a decrease in the overall rate of progression at higher peptoid equivalents. We hypothesize this decrease in assembly speed is due to a decrease in diffusion of the hybrid peptoid-QD monomers as the number of peptoids on the surface of the QDs and the size of the hybrid unit increases.

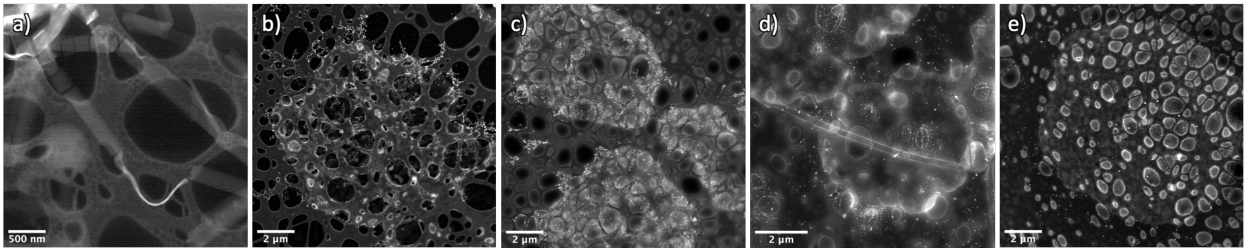

Figure 3.7. Final products of assemblies based on changing the equivalents of peptoid relative to the number of QDs present for 20, 5, 3, 1, 0.3 eq (left to right). High peptoid equivalents (20 eq.) shows peptoid sheets forming with rolling and attachment of smaller sheets (a), not seen without QDs present. With low equivalents (5-0.3 eq.), the final product is the same as the assembly described previously, independent of the amount of peptoid added (b-e). Assemblies in MeCN/H_2O with MEEAA-CdSe.

Changing the sequence of the peptoid to an asymmetric sequence with alternating (4-bromophenyl)ethyl and (4-bromophenyl)methyl side chain groups, $(NbrpeNbrpm)_3Dig$ (**Figure 3.8a**), which forms twisted nanoribbons in absence of QDs, yielded inconsistent structures both within a given TEM grid and across samples regardless of timepoint or peptoid equivalents (**Figure 3.8**). However, alteration of the assembly pathway with QDs was seen and gave structures distinct from the peptoid alone. The assemblies showed very large hybrid materials as early as 1 h for all samples but did not show any distinguishable trends. It is hypothesized that the asymmetric sequence forms a twisted structure due to the differences in packing between the two sides of the peptoid.[31,32,36,37] By having a bulky QD at the end of the sequence, this difference in packing could be disrupted and the extent of the disruption may depend on how many peptoids are on a given

QD, yielding inconsistent products. As a result, the rest of the studies described below were performed with the symmetric peptoid (Nbrpe$_6$Dig) at 1 eq. per QD.

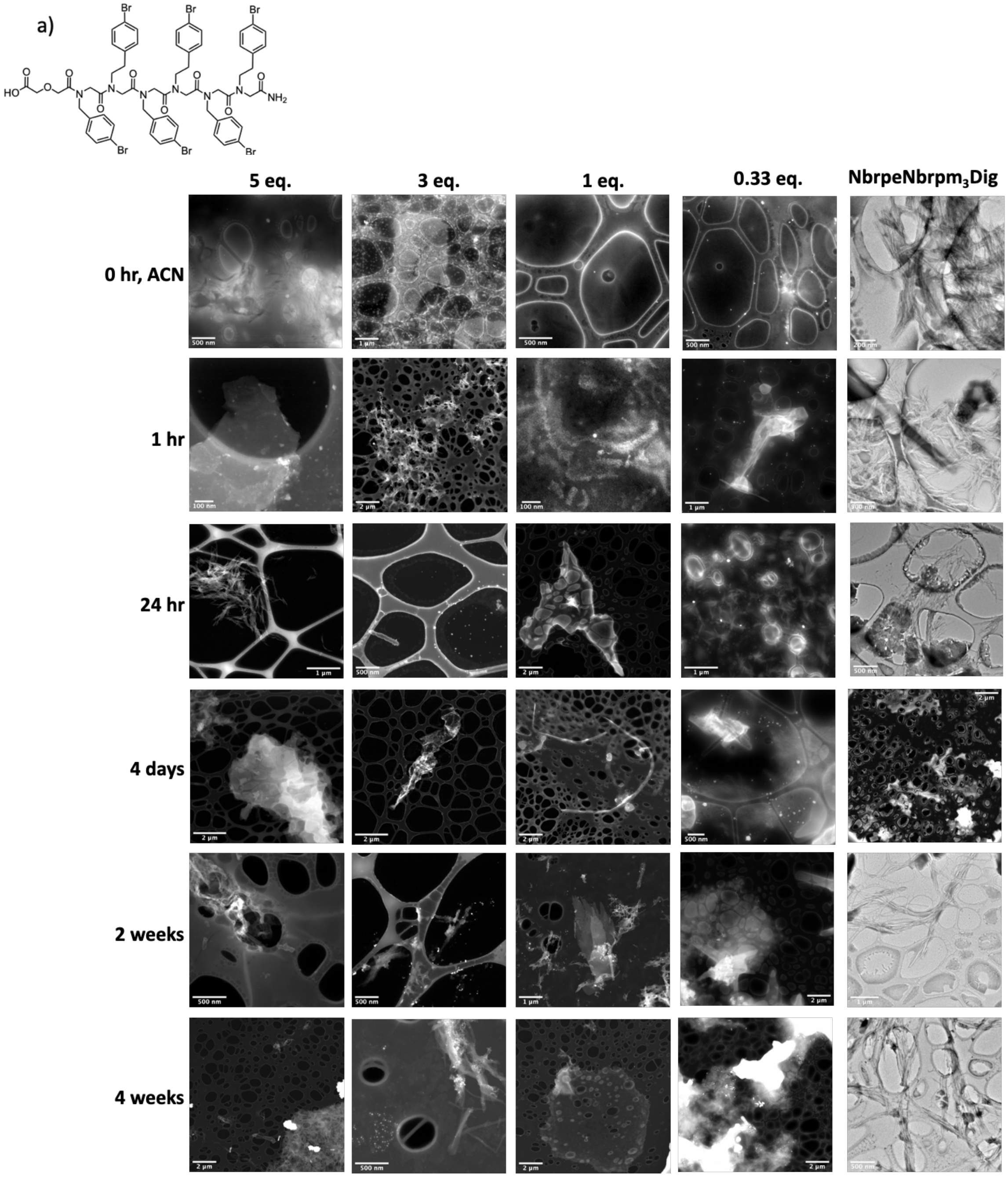

Figure 3.8. Assembly pathway for asymmetric peptoid sequence, NbrpeNbrpm$_3$Dig (a), and at low equivalents (5-0.3 eq.) with MEEAA-CdSe QDs through 4 weeks. Intermediates and products

are inconsistent both between samples and within a given sample. The assemblies with QDs are distinct from the peptoid alone and yield large hybrid structures after only 1 h.

3.2.2 *Modulating QD surface chemistry to improve assembly in organic solvents.*

By changing the ligand on the QD surface we can directly probe how the hydrophobicity of the peptoid-QD unit impacts the assembly process, allowing us to determine how different design elements lead to changes in the reaction landscape and ultimately the structure of the final assemblies. CdSe QDs (2.4 nm) were synthesized with oleic acid (OA) and MEEAA to generate hydrophobic and amphiphilic QDs, respectively, while maintaining carboxylate binding groups. To better solubilize the OA-CdSe QDs, the mixtures were assembled in dimethyl sulfoxide (DMSO) and chloroform ($CHCl_3$). Chloroform was chosen to dissolve the OA-CdSe QDs and peptoid monomers, replacing acetonitrile as the evaporating solvent, and DMSO to replace water as the higher boiling point polar solvent to create unfavorable interactions with the aryl halogens on the peptoid.

The peptoid monomer was assembled alone in these solvents to get a baseline for peptoid assembly. In $CHCl_3$, the peptoids formed an equal mixture (by number) of amorphous peptoid structures with hollow regions (207 ± 105 nm) and small rectangular sheets (~100 nm) immediately after dissolution (**Figure 3.2c,d**). After 18 h, only aggregates of hollow spheres several hundred nanometers in diameter were present (**Figure 3.9a**). With the addition of DMSO, the structures collapsed and shrank until peptoid fibers (66.7 ± 30.9 nm wide) with spheres (54.0 ± 11.9 nm) attached to the fiber edges formed at 5 days (**Figure 3.9b,c**). The fibers grew slightly over the course of a few weeks and amorphous sheets were observed (405 ± 131 nm) but never seen to formed crystalline sheets, as evidenced by their irregularity in size, shape, and contrast in

TEM (**Figure 3.9d**). Given that assembled structures were present immediately after dissolution, we believe the observed structural evolution is based on peptoid monomer rearrangement rather than complete dissolution and re-assembly from monomers, as seen in aqueous conditions. In general, these observations suggest hindered assembly in the organic solvent system, likely due to decreased solubility of the monomer units.

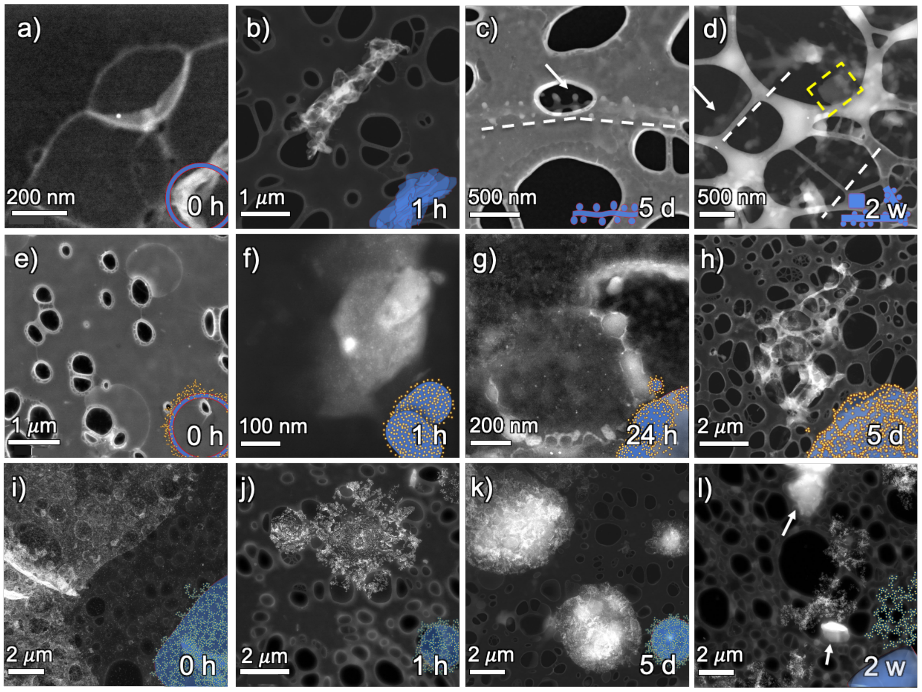

Figure 3.9. Peptoid assembly in $CHCl_3$/DMSO alone (a-d), with MEEAA-CdSe (e-h), and with OA-CdSe (i-l). Peptoid alone showed large hollow spheres (a) that collapsed to form large aggregates (b), and eventually fibers (white dashed line, c) decorated by small dense spheres (arrow, c). Some sheet formation was observed (yellow dashed line) but no large, well-defined sheets were observed (d). The presence of MEEAA-CdSe QDs produced similar large hollow spheres decorated by QDs prior to DMSO addition (e), but then facilitated the solubilization of the peptoid, generating sheets with an even distribution of QDs(f). Over time QDs concentrated at the edges (g), ultimately resulting in assembly of the small sheets into large multilayer hybrid sheets

similar to what was observed in MeCN/H_2O (h). OA-CdSe generated a hydrophobic hybrid monomer unit that formed large 2D sheets in $CHCl_3$ (i). Upon addition of DMSO collapse to form small 2D aggregates (j) that evolved into 3D hybrid multilayers (k), and eventually phase segregation of peptoid (white arrows) and QD (l).

Adding QDs with high coverage of an amphiphilic ligand should increase the solubility of the hybrid monomer unit and facilitate the formation of sheets. MEEAA-CdSe was assembled with 1 eq. of peptoid using the organic solvent system. Prior to the addition of DMSO, the QDs did not alter the hollow peptoid structures ($1.11 \pm 0.37\ \mu$m), but were instead bound to the exterior (**Figure 3.9e**). Some nanofibers reminiscent of the MeCN/H_2O system were observed but did not persist once DMSO was added. After the addition of DMSO, peptoid sheets evenly decorated with QDs (115 ± 79.2 nm) rapidly appeared and underwent aggregation over time (**Figure 3.9f,g**). The hybrid structures formed over 4 weeks primarily included large assemblies (~2 μm) composed of smaller sheets with a higher density of QDs on the edges (~100 nm, **Figure 3.9h**), similar to the assemblies observed in MeCN/H_2O. The assembly of hybrid monomer units in organic solvents did not produce spherical and fiber intermediates, once assembly was initiated, as in MeCN/H_2O (**Figure 3.3f-h**) but proceeded directly to hybrid peptoid-QD sheets after only 1 h. The QDs were again seen to etch to 1.72 ± 0.22 nm, as was observed in the aqueous system. This more rapid progression to the hybrid sheet structures suggests that the QD-peptoid monomer unit is more soluble than the peptoid alone in the organic solvents, resulting in greater lability and faster assembly. Interestingly, these observations are opposite to the trends observed in the aqueous system where additional intermediates and slower sheet formation were noted in the case of the QDs. Together these data suggest that monomer solubility plays a crucial role in the assembly dynamics and that this solubility can be dramatically tuned based on the ligation of the appended QDs.

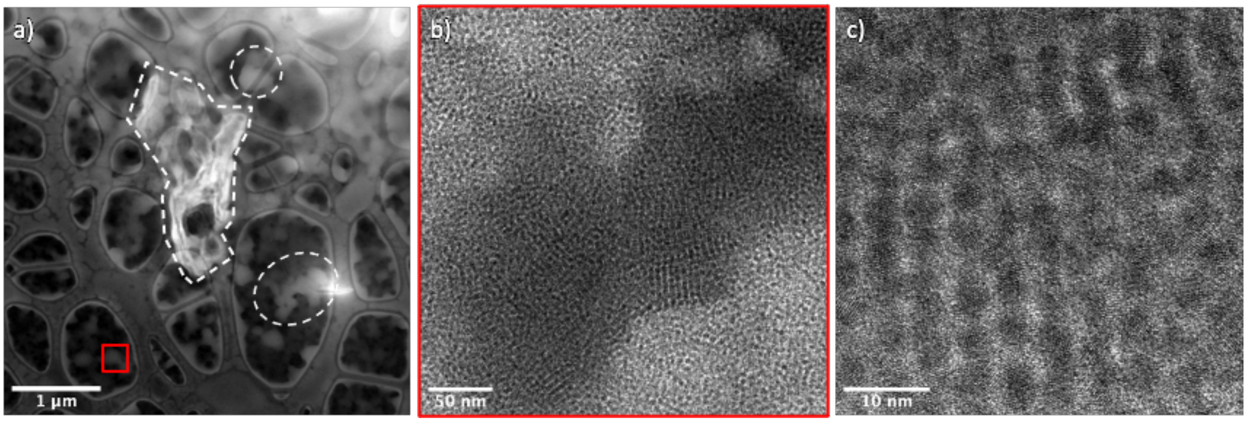

Figure 3.10. MEEAA-CdS QDs with 1 eq. of peptoid in $CHCl_3$ after 18 h. STEM showed peptoid aggregates with QDs all around the edges (a, white dashed lines). BF showed ordering of the QDs near peptoid edges with primarily a linear or row-like pattern (b,c).

To further push the assembly pathway away from evaporative ordering based on hydrophobicity, OA-CdSe QDs were assembled with 1 eq. of peptoid. A hybrid unit with OA-CdSe yields a highly hydrophobic unit with both the QD surface and the exposed portion of the peptoid being insoluble in DMSO. Prior to DMSO addition, large 2D hybrid sheets were seen after 18 h in $CHCl_3$ with lengths greater than 15 μm (**Figure 3.9i**). Within the sheets there were areas of folding or curling, but they appeared to be primarily a monolayer of QDs without any distinct ordering among the QDs. This sheet formation indicates that by changing the QD surface chemistry, assembly can be induced without the addition of an antisolvent and without any evaporative processes as a driving force. With the addition of DMSO, the sheets collapsed initially into 2D circular structures that grew into larger 3D aggregates over time (**Figure 3.9j,k**). We hypothesize that this 3D aggregation is due to the frustrated structure where neither the QDs nor peptoids are sufficiently soluble in the $CHCl_3$/DMSO solvent mixture, resulting in amorphous packing of the hydrophobic units. After most of the $CHCl_3$ evaporated, phase segregation was observed between the peptoids and QDs with large peptoid-rich structures forming and free QDs scattered across the TEM grid (**Figure 3.9l**). This phase segregation suggests that the driving force for peptoids to assemble is still present under these conditions, but the peptoids are unable to order in a favorable manner with the QDs attached.

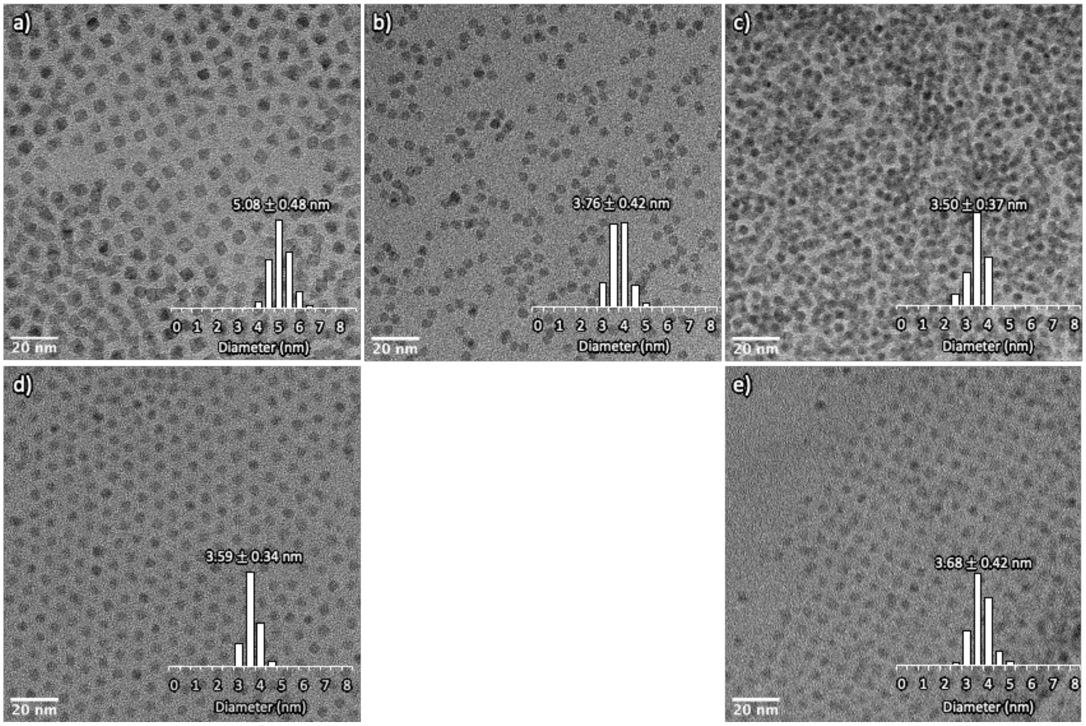

Figure 3.11. OA-CdS QDs (5.1 nm) after synthesis and purification without any modification (a) and after complete ligand exchange with MEEAA (b). Complete ligand exchange results in etching of the QDs to produce 3.8 nm particles, likely a result of removal of surface cadmium bound to oleate at the time of removal. Etching of the CdS QDs is also see upon assembly to 3.5 nm (c). This etching is not observed when 3.6 nm OA-CdS QDs (d) are left in solution with peptoid and assembled, as evidence by the change in packing pattern of the 3.7 nm QDs (e). These results indicate that peptoid interacting with the QD surface may lead to some etching but the addition of a polar, coordinating solvent such as water or DMSO also leads to etching of the surface.

3.2.3 *QD-mediated synthesis of hybrid structures and binary-QD lattices.*

Another route to change the peptoid-QD assembly is by changing the size of the QD relative to the peptoid and increasing the overall bulk of the hybrid monomer unit. CdS QDs were synthesized with OA capping ligands and then were subjected to ligand exchange to produce 3.8 nm MEEAA-CdS QDs. These larger QDs have similar surface chemistry to the MEEAA-capped CdSe QDs, in addition to the same quasi-spherical zinc blende structure. The peptoid monomer is 3.5 nm in length and 1.9 nm in width when fully extended, thus by using CdS QDs that are similar in size or larger, we expect a greater impact on assembly dynamics and morphological outcomes. The same general $CHCl_3$/DMSO assembly process was followed as above with one peptoid monomer per QD, with the only notable difference being the overall volume of QD was much larger than previously due to the increased QD size. In $CHCl_3$, large, amorphous peptoid aggregates were seen with QDs on the edges (~1 μm, **Figure 3.10a**). QDs were seen to order into a linear packing pattern near the edges of the peptoid aggregates (**Figure 3.10b,c**). Exposure to the peptoids and DMSO led to an initial etching of the QDs to give a diameter of 3.5 ± 0.4 nm (**Figure 3.11c**). This etching was not observed when QDs were assembled in $CHCl_3$, suggesting that the addition of DMSO may also contribute to etching of the QD surface (**Figure 3.11d,e**).

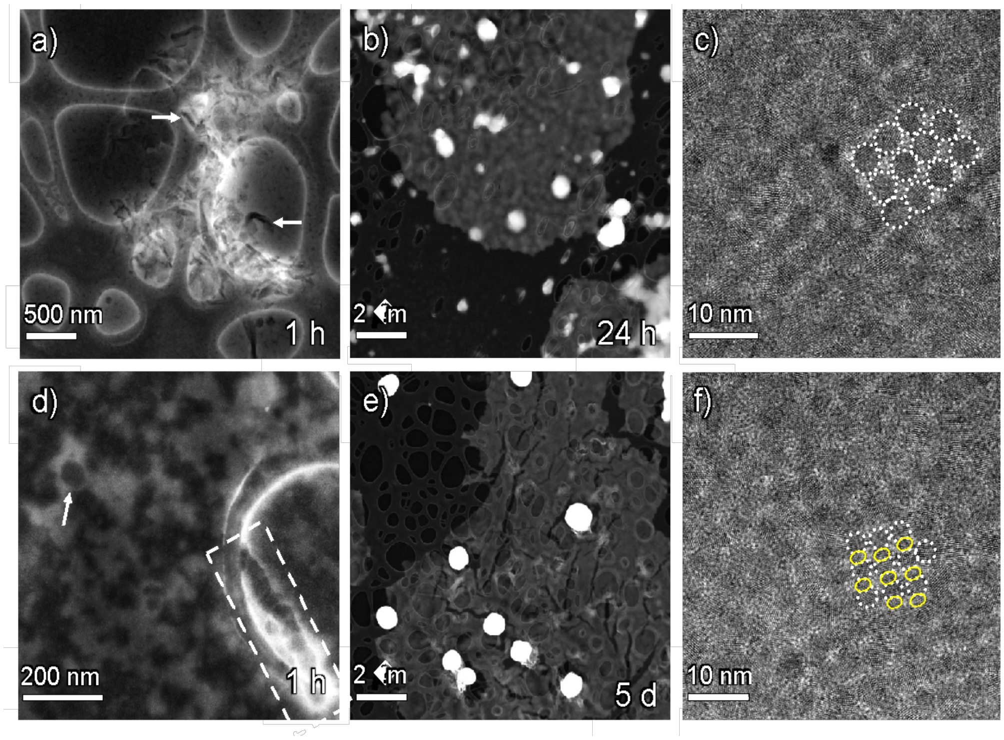

Figure 3.12. Assembly of CdS QDs with 1 eq. peptoid at 1 h (a) and 24 h (b). Early time points show phase segregation with rectangular peptoid structures (white arrow) decorated with QDs (a) until peptoid-QD integrated sheets form (24 h). Hybrid sheet shows CdS QDs (white dotted line) in square close packed arrays (c). Assembly of CdSe:CdS (1:1) QDs with 1 eq. peptoid at 1 h (d) and 5 d (e). Amorphous peptoid structures (white dashed line) and micelles (white arrow) decorated with QDs are seen at 1 h until sheets form after 5 d (e). The same square close packed arrays are seen for the mixed system (f) with CdSe QDs (yellow circles) seen between the CdS QDs (white dotted lines).

These peptoid aggregates with linear ordered QDs on the edges were maintained after DMSO addition with the appearance of large spherical aggregates comprised of primarily QDs, likely due to the high QD coverage (**Figure 3.12a**). By 24 h, large 2D sheets were seen on the order of 10 *μ*m that were persistent through the rest of the evaporation process (**Figure 3.12b**). Closer inspection of the sheets revealed the QDs packing in a square close packed array, with one

QD having four nearest neighbors (**Figure 3.12c**). This ordering was observed in patches throughout the sheets with crystalline domain sizes ranging from 15 to 100 nm with about 14% of the total sheets exhibiting order (**Figure 3.13**). These sheets were noticeably distinct from other assemblies we had observed previously and are reminiscent of structures that are dictated by inter-QD interactions arising from oriented attachment (vide infra), with the peptoid acting as a surface modifier.[49-52] We expect the CdS QDs to exhibit more highly ordered packing when compared to CdSe QDs due to their size relative to the peptoid monomer. Larger QDs are expected to more easily disrupt peptoid interdigitation, precluding the formation of conventional peptoid sheets. Furthermore, the larger CdS QDs display more pronounced facets, which may result in facet-selective binding of the peptoid monomer and result in more pronounced ordering.[53]

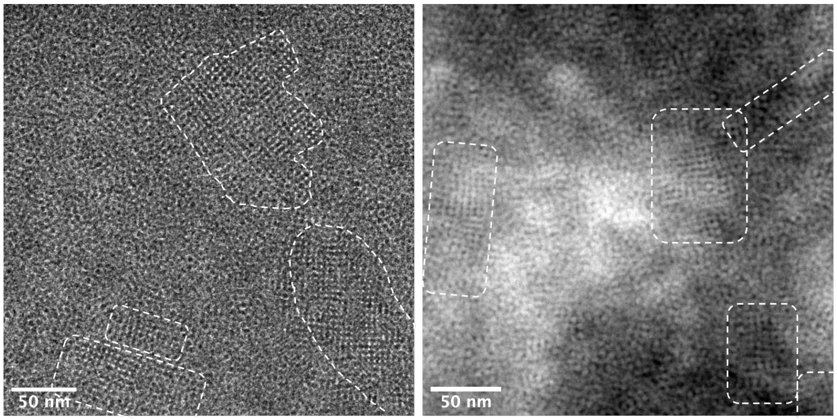

Figure 3.13. Patchy crystalline regions of CdS QDs in the hybrid sheets. Crystalline regions were observed to range from 15 to >100 nm. Examples of ordered regions are denoted by the white dashed lines.

Ordered nanoparticle superlattices with multiple types of nanoparticles have been explored through slow evaporation on a surface or at an interface, as well as by functionalization with ligands with chemical complementarity like DNA.[11,19,54,55] In the systems based on evaporation, the nanoparticle packing can be altered by changing the sizes of the nanoparticles relative to each other and their relative stoichiometries.[55] We sought to combine the CdSe and CdS QD systems to access free-standing binary QD assemblies. A total of 1 eq. of peptoid per total QD was combined with CdSe and CdS (1:1) and assembled in $CHCl_3$ and DMSO. The general assembly pathway was consistent with the CdS system, but sheet generation was slightly slowed. Peptoid micelles, previously seen in the CdSe system, were also observed at early time points with QDs in a linear pattern near the edges (**Figure 3.12d**). The QDs were dominated by CdS, with CdSe being relatively difficult to identify, but were observed throughout the time series with the identification of ~2 nm particles. We propose that this dominating effect of the CdS is a result of the more well-defined faceting and greater total volume of CdS present compared to CdSe. Over the course of 4 weeks, the sheets grew from ~ 800 nm to >5 μm while remaining 2D until at 4 weeks ordering was observed within the sheets in a similar patchy square close packed pattern (~15% of total sheet area is ordered) as seen with CdS QDs alone (**Figure 3.12e,f**). When CdS and CdSe were mixed without peptoid present, there was no evidence of ordering between the QDs (**Figure 3.14**).

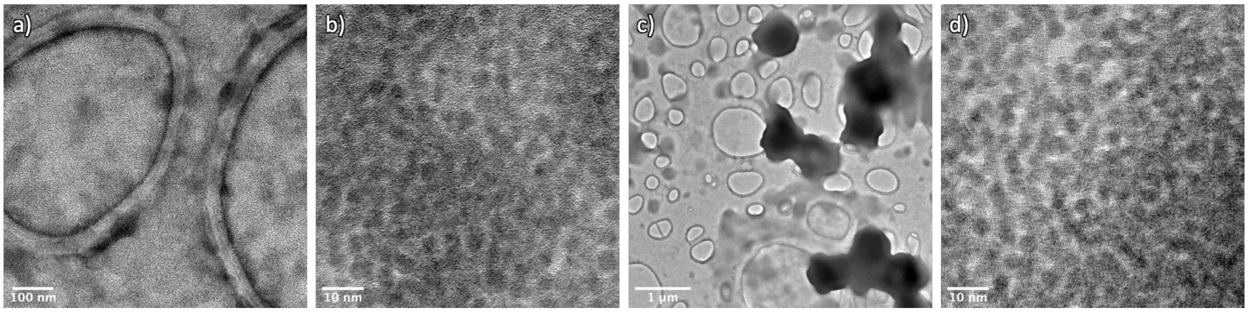

Figure 3.14. CdSe and CdS QDs mixed without peptoid present in $CHCl_3$ (a,b) and $CHCl_3$/DMSO (c,d) with no ordering of the QDs seen for either mixture (b,d). Large, round QD aggregates are seen for the mixed solvent, similar to those seen throughout the peptoid assembly, likely due to slow evaporation of DMSO and the high QD concentration (c).

Some aggregation of the QDs was seen due to high QD concentration but no free standing, 2D structures were observed in CHCl$_3$ or CHCl$_3$/DMSO. Increasing the ratio of CdSe to CdS did not lead to different packing structures, but rather a slow transformation of large sheets to smaller peptoid-QD sheets attached via bridging QDs. With increasing CdSe:CdS, the packing became more disordered, moving from square-packed QDs to linear packing, until total disorder was observed (**Figure 3.15**). These results suggest the CdSe acts as an "impurity" in the system, not dictating the structure as the CdS does. As the concentration of impurity increases, the sheets begin to break apart into smaller structures and aggregate in a fashion similar to that seen in the CdSe only system. Assembly of CdS and CdSe QDs into ordered arrays did not show significant changes in the optical properties. No change was observed in the location or intensity of the photoluminescence for the assemblies and a 2 nm redshift was seen for the absorbance (**Figure 3.16**). We hypothesize that the lack of long-range order and decreased solubility of the assemblies with time give properties comparable to free QDs.

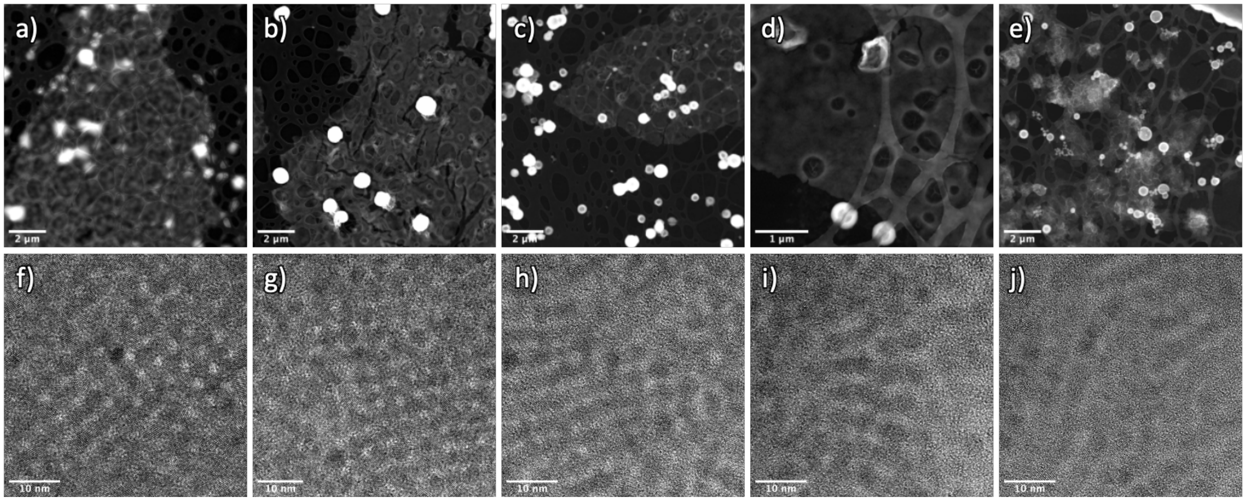

Figure 3.15. Varying the ratio of CdSe to CdS with 1 eq. of Nbrpe$_6$Dig in CHCl$_3$/DMSO from CdS alone (a,f), 1:1 (b,g), 3:1 (c,h), 6:1 (d,i), and 16:1 (e,j). Without CdSe, CdS QDs show large sheets with square-close packing (a,f), this structure is maintained with 1:1 CdSe:CdS (b,g). As

the amount of CdSe increased (3:1, 6:1, 16:1 CdSe:CdS, c-e and h-j), the order in the material decreased going first to a straight row packing and then non-linear row packing. The large sheets also begin to break down, forming more discreet sheets, similar to those seen in pure CdSe assemblies. This implies the CdSe act as an “impurity” in the binary hybrid system with the CdS being the structure determining unit.

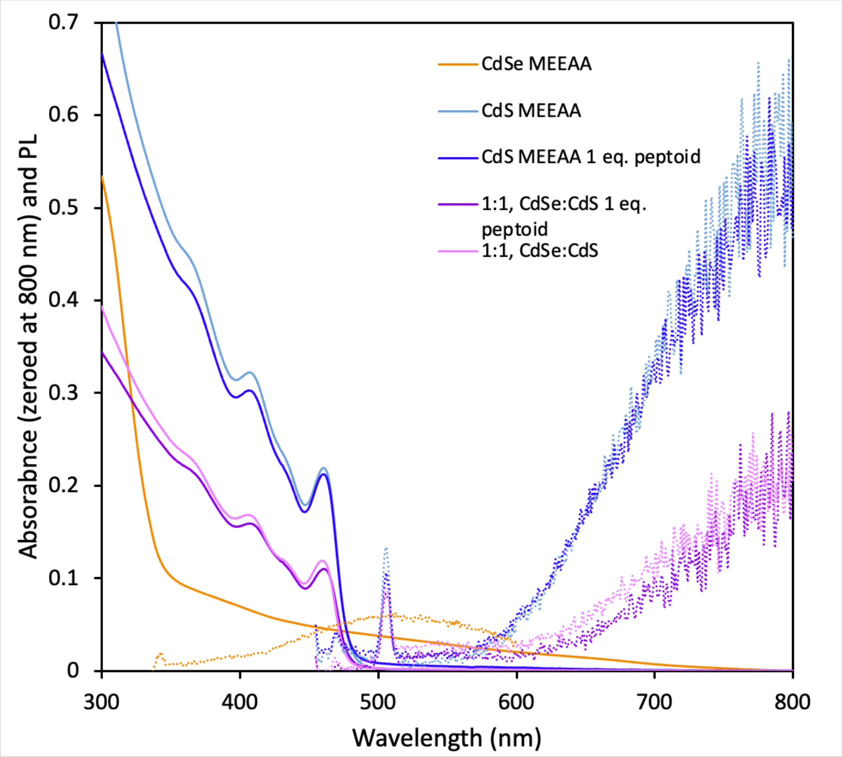

Figure 3.16. UV-Vis absorption and photoluminescence (PL) of QDs alone and of assemblies with 1 eq. of peptoid and a constant concentration for total QDs present. Without peptoid present, CdS MEEAA QDs showed $\lambda_{\text{max, Abs}}$ = 460 nm and $\lambda_{\text{max, PL}}$ = 506 nm. With peptoid present, there was a slight shift in absorption to $\lambda_{\text{max, Abs}}$ = 461 nm and no change in emission. CdSe MEEAA QDs showed absorption throughout with broad features at 370 and 615 nm and no observable PL beyond broad trap emission centered around 515 nm. A 1:1 mix of the QDs without peptoid mirrored the free CdS QDs with $\lambda_{\text{max, Abs}}$ = 459 nm and no shift in emission. With peptoid present,

the mixed QD system again showed a small shift in absorbance to $\lambda_{\text{max, Abs}} = 462$ nm and no change in the emission. The addition of peptoid shows a slight shift in absorbance, indicating there may be some electronic communication between QDs due to ordering but there is no effect on the emission nor any contribution from CdSe QDs, when present.

3.2.4 *Characterization of CdS and CdSe/CdS ordered arrays and the role of peptoid.*

To understand the formation of these ordered CdS and CdSe/CdS assemblies further, we sought to characterize their structure and dependence on drying through TEM image analysis, atomic force microscopy (AFM), and altering sample deposition. The porous spacing between the CdS particles was seen to be 1.75 ± 0.20 nm via TEM (**Figure 3.17a**). For 3.5 nm particles (after etching), without accounting for ligands present, the pore spacing between particles would be expected to have a diameter of 1.4 nm. Accounting for ligands on the QD surface that are ~1.5 nm in length with minimal interdigitation between neighboring ligand shells, a spacing of 1.9 nm would be expected (**Figure 3.17b**).

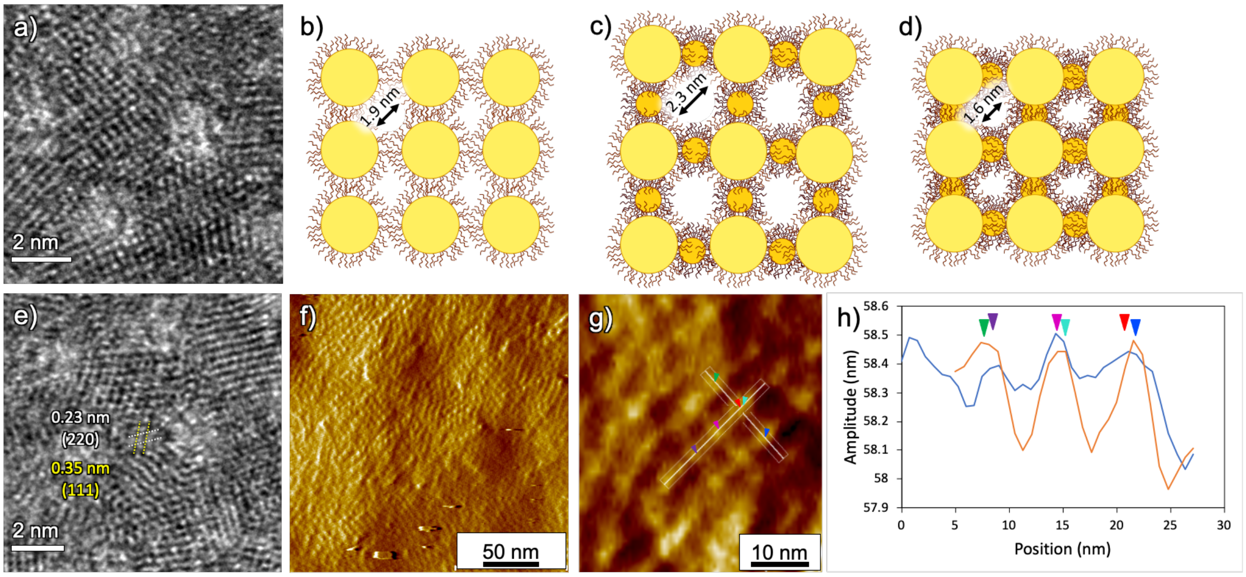

Figure 3.17. High-resolution image of CdS QDs within the 2D sheets showing a pore diameter of 1.75 ± 0.20 nm (a). Carton representation of CdS QDs with minimal interdigitation of the ligands gives an expected pore diameter of 1.9 nm (b). Cartoon representation of CdS QDs with incorporated CdSe QDs between without overlap (c) and with overlap (d) giving an expected pore diameter of 2.3 nm and 1.6 nm, respectively. High-resolution image within the sheet of mixed CdS and CdSe shows a feature between the CdS with a width of 1.65 ± 0.25 nm and pore size of 1.64 ± 0.20 nm (e). The feature showed lattice spacing of 0.35 nm and 0.23 nm, consistent with the (111) and (220) planes of CdSe. AFM amplitude image of the mixed sheets showing a patchy structure with ordered QDs (f). Perpendicular line scans of the mixed lattice show one direction with only CdS (orange line) and one with intermediate peaks (blue), presumably from out of plane CdSe (g, h).

The packing for mixed QDs showed a slight decrease in the pore size via TEM (1.64 ± 0.20 nm) compared to CdS QD assemblies (**Figure 3.17e**). Interestingly, an apparent necking feature was seen between the CdS QDs in the mixed QD samples with a width of 1.65 ± 0.25 nm, consistent with the diameter of the etched CdSe QDs (**Figure 3.12f, yellow dashed lines**). This feature did not appear to be consistent with particle fusion due to discontinuity of the lattice fringes and its round instead of tapered appearance, but rather the presence of a separate CdSe sublattice. Identification of the CdSe QDs was confirmed using high-resolution TEM to show d spacing values of 0.35 nm and 0.23 nm, consistent with (111) and (220) planes of zinc-blende CdSe (**Figure 3.17e**). Additionally, EDS analysis of the CdSe/CdS sheets showed signal from Se and higher Cd/S ratios (1.38) than would be expected for CdS alone (1.1) (**Figure 3.18**).[56] The ratio of S/Se was found to be 19.4, equating to ~2 CdS QDs for every CdSe QD present (considering the expected number of S and Se for 3.5 and 1.7 nm QDs, respectively). This is consistent with AFM and TEM images that do not show the necking feature between every CdS QD in the ordered lattice, suggesting some regions of pure CdS (**Figure 3.17e,g,h**). If the CdSe were positioned in the plane with the CdS, accounting for partial interdigitation of the ligand shells, we would expect an increase in pore size to 2.3 nm (**Figure 3.17c**). However, positioning the CdSe above or below the plane of CdS at interstitial sites results in the lattice of CdS being preserved with an apparent reduction in the pore size (1.6 nm) due to additional material at the interstitial sites (**Figure 3.17d**).

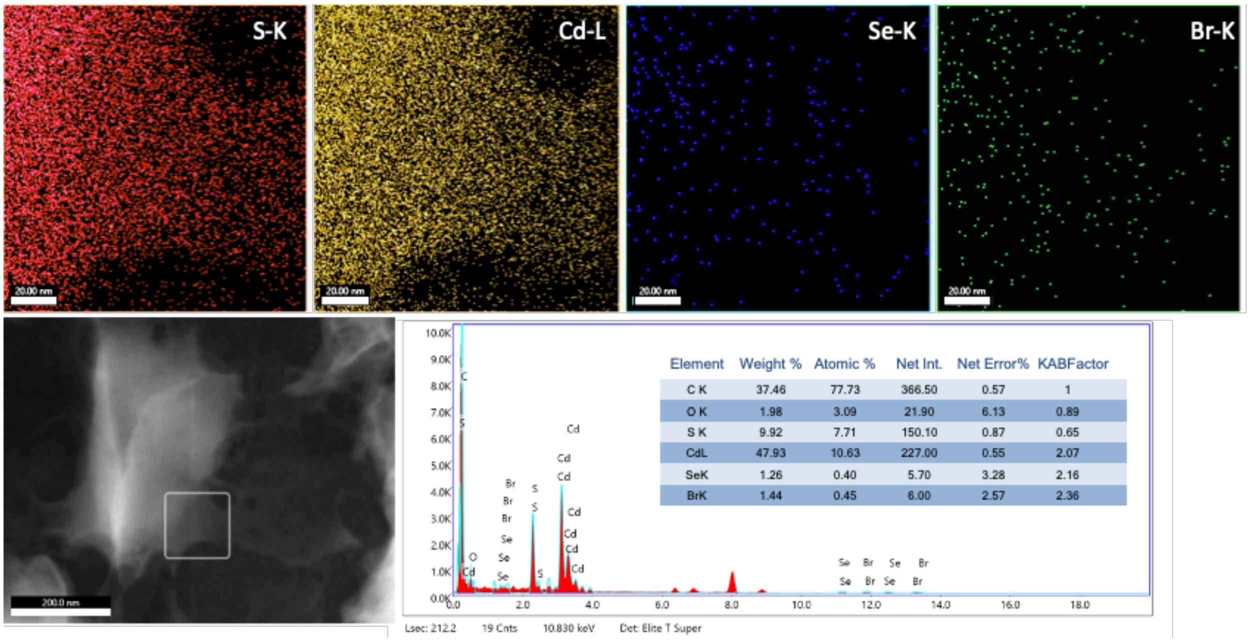

Element	Weight %	Atomic %	Net Int.	Net Error%	KABFactor
C K	37.46	77.73	366.50	0.57	1
O K	1.98	3.09	21.90	6.13	0.89
S K	9.92	7.71	150.10	0.87	0.65
CdL	47.93	10.63	227.00	0.55	2.07
SeK	1.26	0.40	5.70	3.28	2.16
BrK	1.44	0.45	6.00	2.57	2.36

Figure 3.18. EDS mapping of CdSe:CdS (1:1) assemblies with 1 eq. of peptoid in $CHCl_3$/DMSO after 4 weeks. Individual CdS or CdSe QDs are unable to be resolved due to sample instability and low signal. Weak Se and Br signal was observed and colocalized with the S and Cd. The Cd/S ratio was found to be 1.38 by atomic percent, higher than the expected 1.1 ratio, likely from the presence of CdSe. Additionally, the S/Se ratio was 19.4 which equals 2.1 CdS per CdSe QD present when accounting for number of S or Se per QD.

Additional characterization of the assemblies was done via AFM to confirm the QD ordering and determine the position of CdSe relative to CdS. Due to the large size of the sheets, the edge of the sheet was not identified with AFM. Nevertheless, the surface of the sheet showed a patchy structure with ordering throughout (**Figure 3.17f**). The patches on the surface showed a layered structure with many layers exhibiting square close packed ordering (**Figure 3.19**). We hypothesize that these assemblies are highly ordered in two dimensions but lack registry in the Z direction due to the overlap of the sheets. AFM images showed the CdSe are not in plane with the CdS as no small QDs were observed (**Figure 3.17g-h**, orange line). However, line scans of the ordered assemblies showed an intermediate peak between CdS, presumably from a layer of CdSe QDs offset from the top layer (**Figure 3.17g-h**, blue line).

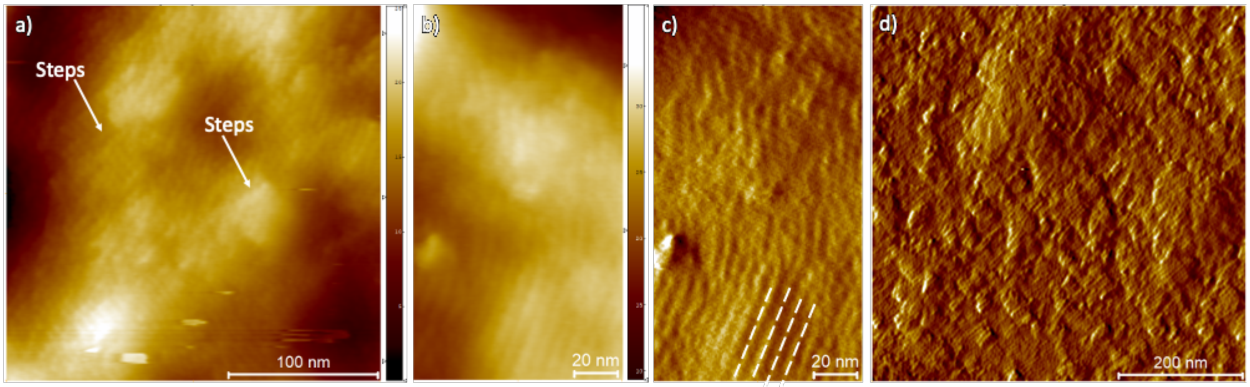

Figure 3.19. Height profile corresponding to the amplitude image (see Figure 4f) of 1:1 CdSe:CdS assemblies with 1 eq. of peptoid showing the layered nature of the assemblies (a). The QDs are seen to maintain a high degree of ordering in the X,Y directions with a decrease in height in a stepwise fashion (a, arrows). Corresponding height and amplitude images (b,c, respectively) displaying the layered nature (white dashed lines). Amplitude image showing the high degree of order in the XY direction for a large area with many patches displaying the square-close pack arrangement of the QDs (d).

Square close packing has been observed extensively for lead chalcogenide QDs both through fusion and drying effects due to decreased ligation on specific facets.[49-52] It has been shown that this fusion process occurs through oriented attachment under conditions in which ligand coverage on the (100) facet is reduced.[49-52,57] This oriented packing is not observed for QDs smaller than 4 nm as the (100) facet is not present in the smaller nanoparticles.[52,57] When the particles are not fused, these lattices arise due to drying effects. In our system, if the peptoids were acting as isolated ligands on the surface of the CdS QDs and only the QDs dictated the structure, one would expect the sheets to arise due to similar drying effects, not the observed solution-phase assembly. To confirm the sheets form in solution due to peptoid and QD contributions, the sheets were isolated by slow centrifugation of the solution, producing a yellow precipitate that was resuspended in DMSO. Large sheets formed in solution would be expected to settle out under these conditions with any free QDs remaining in solution. TEM analysis showed the same 2D sheets in the pellet with slight destabilization seen by a reduction in the percentage of ordered arrays (**Figure 3.20**). The supernatant only showed structures associated with random aggregation of free QDs and no evidence of ordering within the aggregates. These results indicate that large structures are present in solution and resemble the large sheets present in aliquots taken from solution.

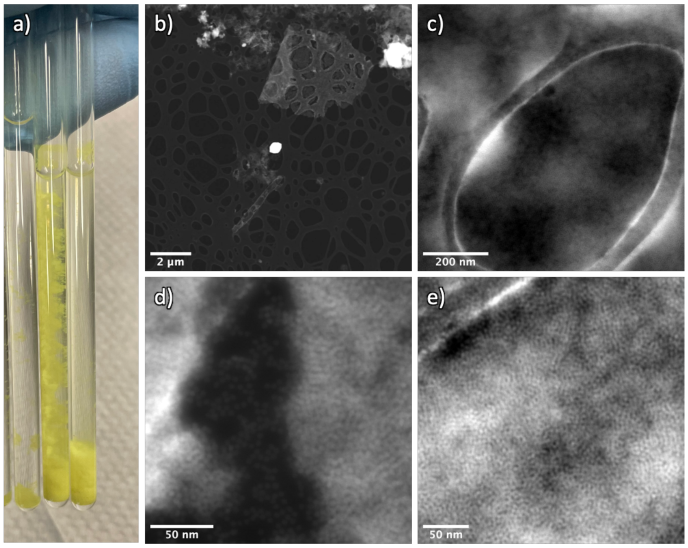

Figure 3.20. Purification of 1:1 CdSe:CdS assemblies to isolate the sheets. Prior to centrifugation, yellow material begins to crash out after 2-4 weeks in solution (a). Once centrifuged, the pellet

shows large sheets with some order but not as well defined as in the native solution (b,d). The supernatant showed primarily free QDs, as seen in the control without peptoid (see Figure S13), with no evidence of ordering (c,e).

To further determine if the sheets are present in solution or result from a drying effect, the TEM grid sample preparation method was altered. To disrupt any drying effects due to slow evaporation, the sample was drop cast onto the grid and let settle for 2 min, dabbed off, and immediately placed under vacuum to rapidly dry the sample. In contrast, typical samples are allowed to settle for 15 min before dabbing off the grid and allowing to dry on a Kimwipe for an additional 15 min before exposure to the vacuum. Analysis of the rapidly dried grid still showed the same large 2D sheets with square close packed QDs, as seen previously (**Figure 3.21**). Moreover, the prevalence of large QD aggregates was decreased and the sheets appeared thinner at the edges relative to standard sample preparation, implying that faster drying of the sample reduces overcrowding and stacking of free QDs on the grid.

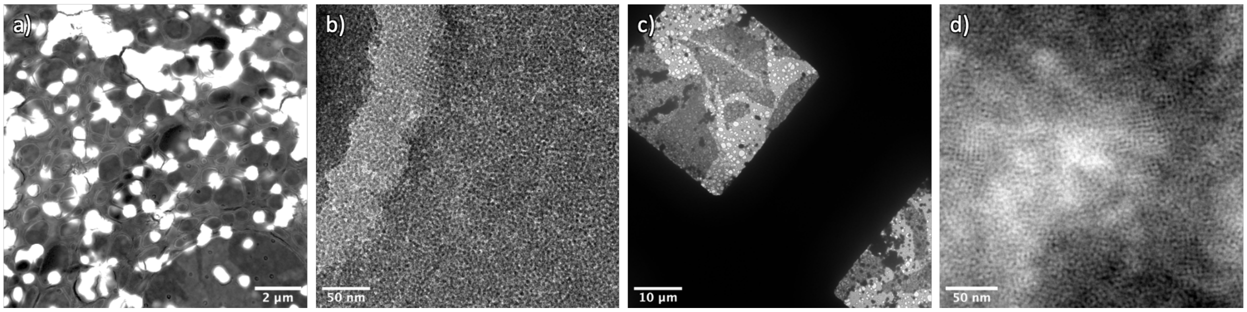

Figure 3.21. Altering the TEM grid preparation for CdS assemblies with 1 eq. Nbrpe$_6$Dig after 6 weeks. Standard grid preparation with slow evaporation shows predominantly free QDs aggregating, making it difficult to see the 2D sheets (white dots, a). Zooming in on an edge of a sheet shows a thick edge, presumably multiple layers of sheets or QDs (b). Rapid drying of the

grid showed decreased aggregation of QDs with large 2D sheets still present with intrinsic ordering of the QDs still apparent (c,d).

Finally, to determine if the assemblies form because of bottom-up assembly and integration of QDs into the sheets or decoration of QDs onto a pre-formed peptoid surface, 1:1 CdSe and CdS QDs were added to pre-formed peptoid sheets in DMSO and allowed to incubate at room temperature. Upon initial addition, QDs were seen to stick non-uniformly to peptoid surfaces, with the sheets mostly remaining intact (**Figure 3.22a**). Over the course of 2 weeks, large sheets similar to bottom-up assembly were observed but did not show ordering of the QDs and stability was lost over time to produce small, rounded peptoid sheets with uneven QD distribution (**Figure 3.22b-e**). These results indicate that the hybrid sheets are not formed due to drying effects alone and the QD superlattices do not arise from post-synthetic coordination to assembled peptoid sheets. Instead, these results support a hybrid system wherein the QDs and peptoids assemble in solution together as a hybrid unit from an integrated structure. We hypothesize that the peptoids are bound to the QD surface, acting as a ligand rather than an assembled template. On the QD surface the peptoid monomers can act as a linker between dots or bind specific facets, leading to the observed square packed superlattices where the inter-QD interactions dictate the final structure.

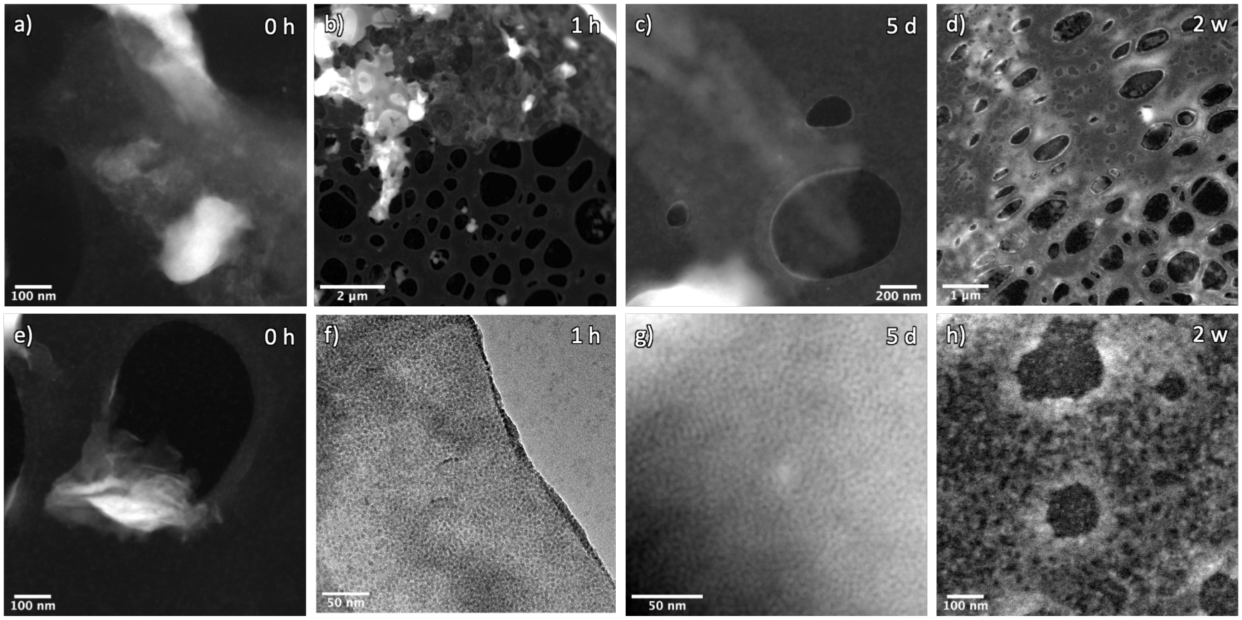

Figure 3.22. Addition of 1:1 CdSe:CdS QDs in DMSO to pre-formed sheets. Immediately after addition sheets are seen intact with QDs randomly aggregated on the surface (a,e). Over time, large 2D sheets formed (b,c,f,g), similar to the bottom-up approach, but they do not remain stable over time and do not show any ordering within the QD domains (d,h).

3.3 CONCLUSIONS

To access new hierarchical hybrid materials, we must first understand the design principles that dictate the evolution of structure in these dynamic systems and determine how different parameters can be used to tune the reaction landscape. In this work, we have outlined two assembly regimes between QDs and peptoids that reversibly bind to the QD surface. In the first regime, the hybrid structures are controlled by both the peptoid and QD, whereas in the second regime, the hybrid structures are dominated by inter-QD interactions. The assembly pathway and progression of intermediates for peptoid-QD hybrid structures were studied in aqueous and organic conditions. Attachment of the QD to the peptoid altered the solubility of the hybrid monomer unit aiding the assembly in organic conditions and stabilizing intermediates in the aqueous system. Design rules such as the ratio of peptoid monomer relative to QD, hydrophobicity of the QD, and size of the QD were explored. Changing the equivalents of the peptoid at low concentrations only changed the speed of assembly based on the diffusion properties of the peptoid-QD monomer unit. Altering the QD capping ligand changed the solubility of the hybrid peptoid-QD monomer unit, generating 2D assemblies prior to anti-solvent addition and disrupting sheet formation afterwards. With larger faceted CdS QDs, it was found that the QD dictated the structure, resulting in highly ordered square packed arrays with peptoids acting as a surface ligand on the QD. Combining two different sized QDs allowed for the incorporation of the smaller dots on top of the CdS lattice, with structures still being dictated by the large CdS QDs. Understanding these design elements allows for careful planning and manipulation of QD size, surface chemistry, peptoid sequence, and solvents to tune access to specific hybrid architectures and predictably generate structural complexity.

3.4 EXPERIMENTAL METHODS

3.4.1 *Materials*

All quantum dot (QD) syntheses were performed air-free in glassware dried overnight in an oven at 160 °C. All reactions and manipulations involving QDs and peptoids were conducted in ambient air in a well-ventilated fume hood or on a benchtop as appropriate. Anhydrous acetonitrile (99.8%), anhydrous ethanol (99.5%), anhydrous methanol (99.8%), anhydrous oleic acid (≥99%), anhydrous dimethyl sulfoxide (≥99.9%), anhydrous chloroform (99%), anhydrous N-methyl-2-pyrrolidinone (99.5%), tetramethylthiourea (98%), and selenium powder (99.5%), dichloromethane (99.8%), N,N'-diphenylethylenediamine (98%), and triethyl orthoformate (98%) were purchased from MilliporeSigma and used without further purification. Acetonitrile-D3

(99.8%) was purchased from Cambridge Isotope Labs and used without further purification. Hexadecane (99%) was purchased from MilliporeSigma, dried over calcium chloride then distilled and stored over activated 3 Å molecular sieves in a glovebox. Toluene and pentane were purchased from MilliporeSigma, collected from a solvent purification system and stored over activated 3 Å molecular sieves. 2-[2-(2-methoxyethoxy)ethoxy]acetic acid (>95%) was purchased from TCI chemicals and dried under vacuum at 50 °C then stored over activated 3 Å molecular sieves. Dowtherm^{TM} was purchased from Dow Inc. and used without further purification. Bio-Beads S-X1 for gel permeation chromatography were purchased from Bio-Rad Laboratories and dried under vacuum at 60 °C. 1,3-Diphenylimidazolidine-2-selenone (*Se*-Im(Ph_2)) and cadmium oleate were synthesized following literature procedure[1]. 18.2 MΩ water was collected from an EMD Millipore purification system. UV−vis spectra were collected on a Cary 5000 spectrophotometer from Agilent.

3.4.2 *Synthesis of CdSe quantum dots*

The synthesis of CdSe QDs was adapted from Hamachi et al.[56] In a dried 3-neck 25 mL round bottom flask equipped with a stir bar, thermowell, condenser, and rubber septum, cadmium oxide (0.023 g, 0.18 mmol) and 2-[2-(2-methoxyethoxy)ethoxy]acetic acid (MEEAA, 0.128 g, 0.72 mmol) were added. The reaction flask was cycled between N_2 and vacuum for a total of 5 times then placed completely under vacuum. The flask was then heated to 50 °C and allowed to degas for 1 h. The flask was then flushed with nitrogen and heated until the solution was clear and colorless indicating the formation of $Cd(MEEAA)_2$ (150 °C, ~30 min). The reaction mixture was allowed to cool to room temperature then placed under vacuum and allowed to degas for 1 h at 50 °C. The flask was flushed with N_2 and the $Cd(MEEAA)_2$ was dissolved in N-methyl-2-pyrrolidone (NMP, 14.25 mL) and heated to reflux (202 °C). In a nitrogen filled glove box, 1,3-

diphenylimidazolidine-2-selenone (*Se*-Im(Ph_2), 0.090 g, 0.30 mmol) was dissolved in minimal NMP (0.75 mL). The *Se*-Im(Ph_2) was rapidly injected to the reaction solution and allowed to react for 24 h. The reaction was monitored using UV-Vis absorption spectroscopy. The QDs were isolated via vacuum distillation of the solvent at elevated temperature (65 °C). The resulting QDs were brought into a glovebox, redissolved in minimal toluene, and centrifuged (7630 rpm, 10 min) to remove any insoluble material. The supernatant was decanted and the QDs were precipitated using pentane (3:1, pentane: QD solution) and then centrifuged. The supernatant, clear and colorless, was discarded and the pellet was resuspended in toluene. A total of 5 repetitions of precipitation, centrifugation and redissolution were performed before dissolving the final pellet in minimal toluene and running a size exclusion column. Two fractions were collected off the column, the first fraction was the one used for further experiments. The QDs show an absorption maximum at 615 nm and average diameter of 2.37 ± 0.39 nm by TEM analysis. Oleic acid (OA) capped CdSe were synthesized as above but OA was used in place of MEEAA and methanol was used as the antisolvent rather than pentane. OA-capped CdSe showed an absorbance maximum at 614 nm with an average diameter of 2.37 ± 0.41 nm by TEM analysis. Stock solutions of QDs were made by weighing out the QDs and dissolving them in a known volume of solvent. Moles of QDs were determined by calculating the molecular weight for a 2.4 nm CdSe QD based on the bulk density, the volume of the QD, and the number of ligands on the surface (~250).[57-58] The molecular weight used for all calculations was 68303 g/mol.

3.4.3 *Synthesis of CdS quantum dots*

The synthesis of CdS QDs was adapted from Hamachi et al.[56] In a dried 3-neck 500 mL round bottom flask equipped with a stir bar, thermowell, condenser, and rubber septum, cadmium oleate (2.43g, 3.60 mmol), oleic acid (OA, 2.04 g, 7.2 mmol) and hexadecane (140 mL) were combined. The reaction flask was evacuated at 100 °C for 2 h. The flask was refilled with nitrogen and heated (230 °C). In a nitrogen filled glove box, tetramethylthiourea (TMTU, 0.396 g, 3.0 mmol) was dissolved in Dowtherm™ (6.0 mL). The TMTU was rapidly injected to the cadmium oleate solution and allowed to react until no more changes were observed in the UV-Vis absorption spectra (~2 h). The QDs were isolated via vacuum distillation of the solvent at elevated temperature (140 °C). The resulting QDs were brought into a glovebox, redissolved in minimal toluene, and centrifuged (7630 rpm, 10 min) to remove any insoluble material. The supernatant was decanted and the QDs were precipitated using methanol (3:1, methanol: QD solution) and then centrifuged. The supernatant, clear and colorless, was discarded and the pellet was resuspended in minimal toluene. A total of 5 repetitions of precipitation, centrifugation, and redissolution were performed before dissolving the final pellet in minimal toluene for storage. The QDs show an absorption maximum at 460 nm and average diameter of 5.08 ± 0.48 nm by TEM analysis.

3.4.4 *Ligand exchange of OA for MEEAA on CdS*

The ligand exchange procedure to replace OA by MEEAA was adapted from De Roo et al.[59] OA-capped CdS QDs were dried ($9.4x10^{-7}$ mol, ~120 ligands per QD) and then 7.2 mL chloroform and MEEAA (2.43g, 6.82 mmol mol, 60 MEEAA per OA present) were added to the pellet. The vial was stirred overnight and then sonicated for 30 min to yield a clear QD solution. The solution was precipitated using pentane (1:12, chloroform: pentane), centrifuged (7680 rpm, 10 min), and the pellet was resuspended in minimal chloroform (~1 mL). Three precipitation, centrifugation, and redissolution cycles were performed, resulting in a colorless supernatant. After the third resuspension in minimal chloroform, 1.2 g of additional MEEAA was added to ensure complete exchange. This mixture was sonicated for 30 min, followed by four additional purification cycles. The sample was stored as a dry powder. The molecular weight was estimated as detailed above assuming 120 ligands per QD to give 274553 g/mol. After complete ligand exchange the QDs were seen to etch significantly to 3.76 ± 0.42 nm via TEM analysis.

3.4.5 *Peptoid synthesis and characterization*

Peptoids were synthesized using a solid-phase monomer synthesis following literature procedures.[32,60] Purity of the peptoid monomers were confirmed using a Waters ACQUITY reverse phase UPLC (corresponding gradient at 0.4 mL/min over 7 min at 40 °C with an ACQUITYBEH C18, 1.7 µm, 2.1 mm× 50mm column) that was connected to a Waters SQD2 mass spectrometry system. For Nbrpe$_6$Dig, the exact mass was found to be 1567.00 g with a molecular weight of 1573.70 g/mol. For NbrpeNbrpm$_3$Dig, the exact mass was found to be 1522.03g with a molecular weight of 1528.71 g/mol.

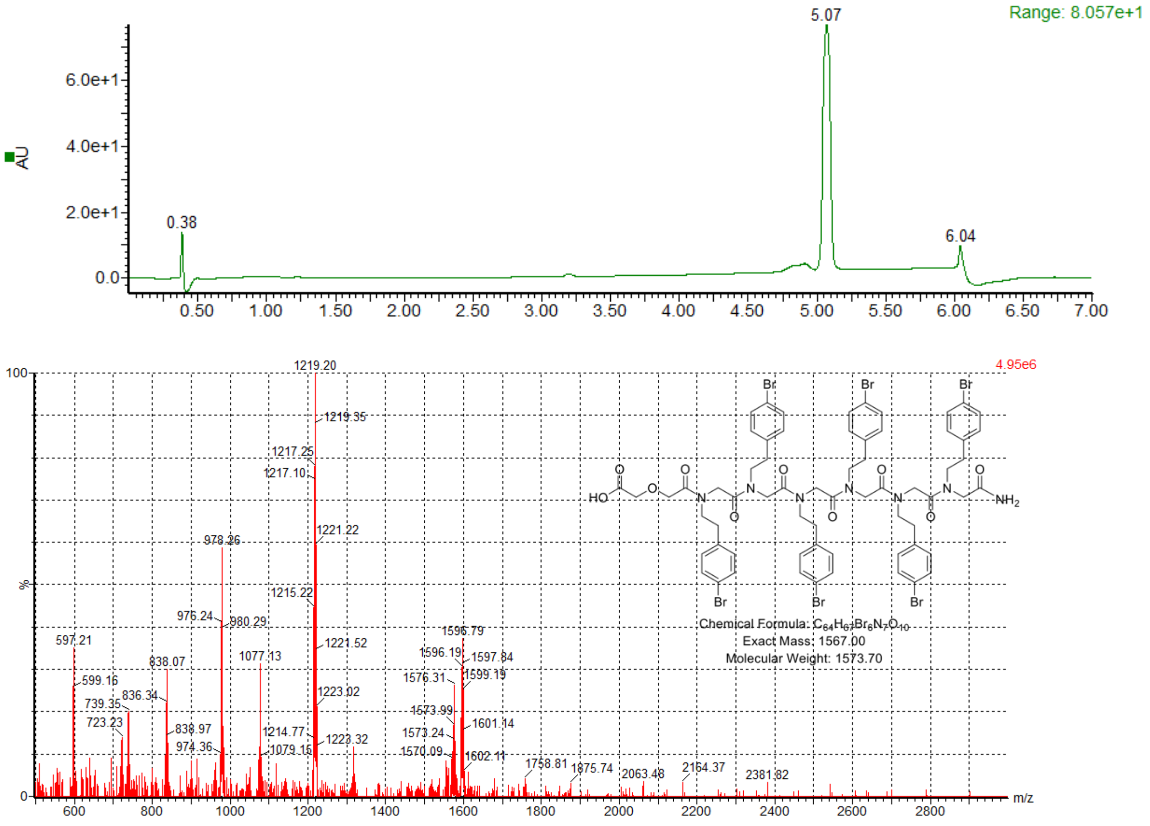

UPLC-MS data for Nbrpe$_6$Dig.

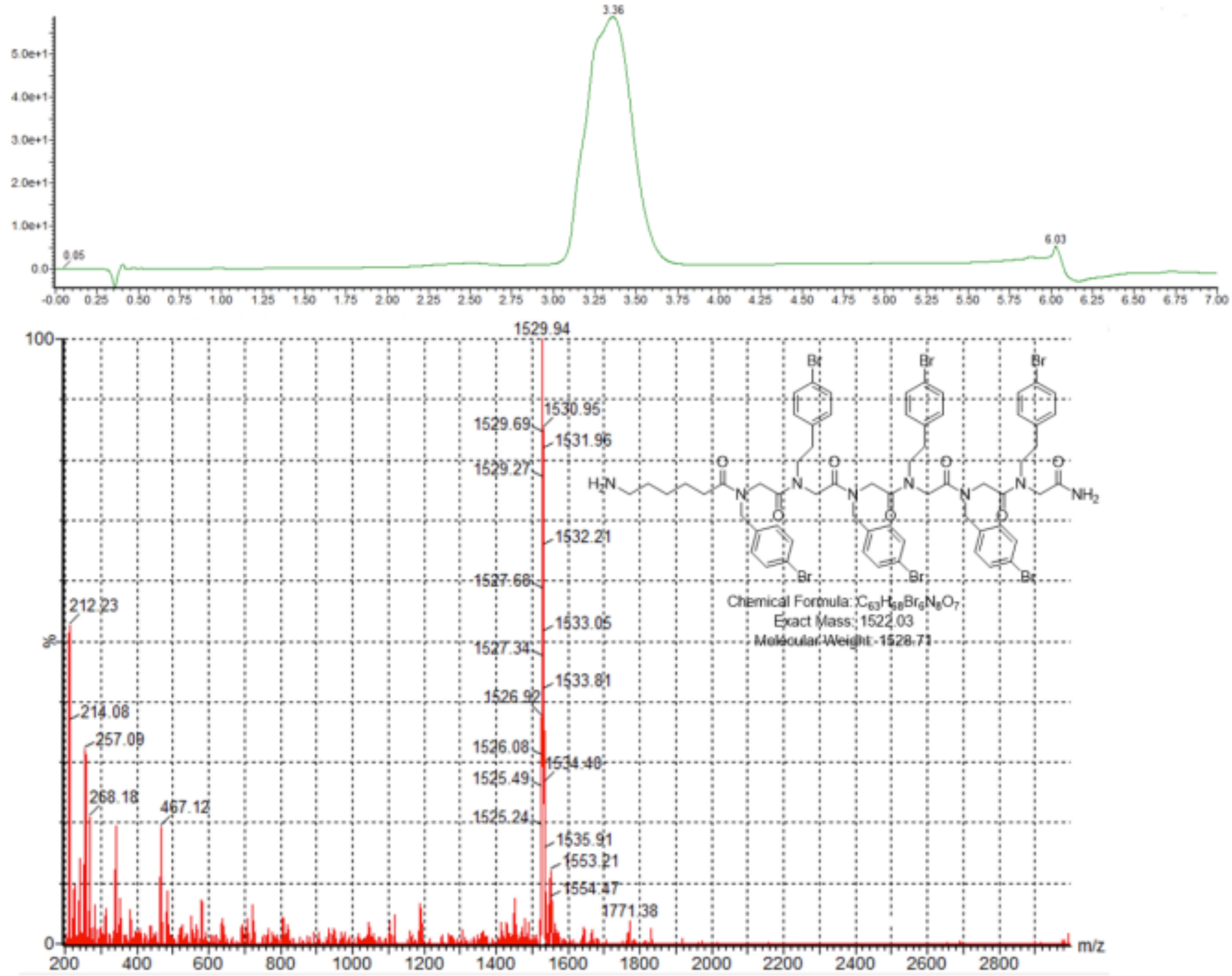

UPLC-MS data for NbrpeNbrpm$_3$Dig.

3.4.6 *General assembly process*

The peptoid concentration was kept constant for all samples to allow for comparison of assemblies at given time points, independent of peptoid concentration since peptoid concentration can influence the speed of assembly. Powdered peptoid monomer was sonicated in MeCN for 10 min to generate a cloudy stock solution. The peptoid stock solution (4.2x10^{-8} mol) was diluted in an NMR tube with MeCN to yield a total volume of (0.5 mL – X μL QD stock solution added) and inverted 3 times. CdSe QDs were dissolved in MeCN to yield a stock solution (typically 0.5

mM). CdSe QDs were added to the dilute peptoid solution to yield the desired eq. of peptoid to QD (equivalents = mol peptoid/mol QD). The resulting solution (8.4×10^{-5} M peptoid) was tightly capped, inverted 3 times then allowed to incubate at room temperature for 18 h to allow for exchange of the peptoid onto the QD. After 18 h, water (0.5 mL) was added to the tube and the sample was allowed to sit uncapped at 4 °C for 4 weeks. To track the assembly process, aliquots were taken from the reaction solution at 0 h (prior to the addition of water), 1 h, 24 h, 4-5 days, 2 weeks, and 4 weeks (see below for TEM sample preparation details). For assembly in $CHCl_3$/DMSO, the general conditions were kept constant, but MeCN was replaced by $CHCl_3$ and water by DMSO.

3.4.7 *Mixed quantum dot assembly process*

The general assembly process was the same as above with all mixed QD assemblies using 1 eq. of Nbrpe$_6$Dig (4.2×10^{-8} mol), the total moles of QDs was kept constant at 4.2×10^{-8} mol, and the solvent system was $CHCl_3$/DMSO. The mixed assemblies were made with an increasing ratio of CdSe to CdS (1-16:1). For the 1:1 assembly, the stock peptoid solution was divided in half and added to a vial for the CdSe QDs then diluted with $CHCl_3$ (0.25 mL – X μL CdSe QD stock solution added). The CdSe QDs (2.1×10^{-8} mol) were allowed to incubate at room temperature for 2 h. The same procedure was followed for CdS QDs in a separate vial with the rest of the peptoid solution. After 2 h, the two vials were combined into one NMR tube and allowed to incubate overnight (18 h) before the addition of DMSO. The same process was followed for other ratios of CdSe to CdS, keeping the ratio of peptoid to QD and concentration constant at each step.

3.4.8 *TEM sample preparation and analysis*

TEM images were collected on a FEI Tecnai G2 F20 microscope operated at 200 keV for bright field and STEM. Samples were prepared by inverting sample solutions 3 times to suspend any precipitates then drop-casting 5 μL of sample onto a suspended ultrathin carbon film on lacey carbon support film, 400 mesh, copper grids purchased from Ted Pella Inc. The samples were allowed to dry in air, without significant air flow, for 15 min on the grids before dabbing excess solvent off and drying for 15 min on a Kimwipe. Samples prepared in DMSO were then dried under vacuum for 30 min to completely remove any residual solvent. All grids were placed in a desiccator for at least 2 h or until imaged. For each sample, the grids were surveyed at low magnification (scale bar ~20 μm, BF) to compare grid holes and identify grid holes that represented the grid as a whole (in regard to type of structures and density of material). The chosen areas were imaged at low magnification in STEM mode and high magnification in BF mode (scale bars 2 μm and 10 nm, respectively) to ensure both large and small material of both low and high contrast were represented. Finally, at least 3 grid holes were checked per sample and representative images were chosen to report. TEM analysis was performed using manual analysis with the help of ImageJ. Histograms, average sizes, and standard deviations for CdSe and CdS QDs were obtained by manual analysis of over 200 particles per sample. Size analysis of assembly intermediates was performed as described but with >75 measurements per sample, apart from very large sheets (>5 μm) which were hard survey many of them due to their size.

3.4.9 *EDS analysis*

EDS images were taken using a FEI Tecnai G2 F20 SuperTwin TEM operated at 200 keV in STEM mode with an EDAX Elite T detector. The samples were prepared as previously mentioned and plasma treated prior to imaging to remove adsorbed carbon and excess carbon signal due to ligands on the QDs. Plasma treatment (2 min, H_2/O_2) decreased the beam related sample damage and sample drift to allow for longer collection times. EDS maps were collected using a spot size of 7, amp time of 7.58 µs, dwell time of 50 µs, image resolution of 512x400, and 8-16 frames per map to limit sample drift and damage while maximizing signal. Ratios of elements were determined by the atomic percent reported. Number of atoms present for CdS or CdSe were obtained by calculating the volume of a particle through the diameter via TEM then using the bulk density to find the mass of the inorganic core. Number of Cd, S, or Se were calculated assuming a 1.1:1 ratio of Cd to S or Se.

3.4.10 *AFM sample preparation and analysis*

Samples were imaged on fixed TEM grids, prepared as detailed above. AFM images were collected on an Asylum Research Cypher instrument in non-contact mode with SNL-10 probes purchased from Bruker AFM Probes.

3.4.11 *NMR analysis*

^{1}H NMR spectra were recorded on 500 MHz Bruker Advance spectrometers. All samples were run with 25 scans, 2 dummy scans, and a delay time of 30 s. Samples were capped prior to scanning but not inverted to keep insoluble material at the bottom of the tube.

3.4.12 *DLS analysis*

Dynamic light scattering (DLS) measurements were performed on a Malvern Zetasizer Nano ZS with a 632 nm laser. Measurements were performed at 25 °C in a plastic cuvette immediately after agitating the solution, without any dilutions. The refractive index was set to water for all mixed solvent samples and set to acetonitrile for the 0 h sample. Scattering data were fit using a multipeak model in the Malvern Zetasizer software.

3.5 REFERENCES

1. Pigliacelli, C.; Sánchez-Fernández, R.; García, M. D.; Peinador, C.; Pazos, E. Self-Assembled Peptide–Inorganic Nanoparticle Superstructures: From Component Design to Applications. *Chem. Commun.* **2020**, *56* (58), 8000–8014.
2. Levin, A.; Hakala, T. A.; Schnaider, L.; Bernardes, G. J. L.; Gazit, E.; Knowles, T. P. J. Biomimetic Peptide Self-Assembly for Functional Materials. *Nat Rev Chem* **2020**, *4* (11), 615–634.
3. Saveleva, M. S.; Eftekhari, K.; Abalymov, A.; Douglas, T. E. L.; Volodkin, D.; Parakhonskiy, B. V.; Skirtach, A. G. Hierarchy of Hybrid Materials—The Place of Inorganics-in-Organics in It, Their Composition and Applications. *Frontiers in Chemistry* **2019**, *7*, 179.
4. Li, Z.; Fan, Q.; Yin, Y. Colloidal Self-Assembly Approaches to Smart Nanostructured Materials. *Chem. Rev.* **2021**, *122* (5), 4976-5067.
5. Kuzuya, A.; Ohya, Y. DNA Nanostructures as Scaffolds for Metal Nanoparticles. *Polym J* **2012**, *44* (6), 452–460.
6. Yamauchi, M.; Masuo, S. Self-Assembly of Semiconductor Quantum Dots Using Organic Templates. *Chemistry – A European Journal* **2020**, *26* (32), 7176–7184.
7. Chen, C.-L.; Rosi, N. L. Peptide-Based Methods for the Preparation of Nanostructured Inorganic Materials. *Angewandte Chemie International Edition* **2010**, *49* (11), 1924–1942.
8. Ritchhart, A.; Monahan, M.; Mars, J.; Toney, M. F.; De Yoreo, J. J.; Cossairt, B. M. Covalently Linked, Two-Dimensional Quantum Dot Assemblies. *Langmuir* **2020**, *36* (33), 9944–9951.
9. Cai, B.; Li, Z.; Chen, C.-L. Programming Amphiphilic Peptoid Oligomers for Hierarchical Assembly and Inorganic Crystallization. *Acc. Chem. Res.* **2021**, *54* (1), 81–91.
10. Hoheisel, T. N.; Hur, K.; Wiesner, U. B. Block Copolymer-Nanoparticle Hybrid Self-Assembly. *Progress in Polymer Science* **2015**, *40*, 3–32.
11. Macfarlane, R. J.; Lee, B.; Jones, M. R.; Harris, N.; Schatz, G. C.; Mirkin, C. A. Nanoparticle Superlattice Engineering with DNA. *Science* **2011**, *334*, 204-208.
12. Tian, Y.; Lhermitte, J. R.; Bai, L.; Vo, T.; Xin, H. L.; Li, H.; Li, R.; Fukuto, M.; Yager, K. G.; Kahn, J. S.; Xiong, Y.; Minevich, B.; Kumar, S. K.; Gang, O. Ordered Three-Dimensional Nanomaterials Using DNA-Prescribed and Valence-Controlled Material Voxels. *Nat. Mater.* **2020**, *19* (7), 789–796.
13. Zheng, J.; Constantinou, P. E.; Micheel, C.; Alivisatos, A. P.; Kiehl, R. A.; Seeman, N. C. Two-Dimensional Nanoparticle Arrays Show the Organizational Power of Robust DNA Motifs. *Nano Lett.* **2006**, *6* (7), 1502–1504.
14. Fry, H. C.; Silveira, G. de Q.; Cohn, H. M.; Lee, B. Diverse Bilayer Morphologies Achieved via α-Helix-to-β-Sheet Transitions in a Short Amphiphilic Peptide. *Langmuir* **2019**, *35* (27), 8961–8967.

15. Lin, Y.; Penna, M.; Thomas, M. R.; Wojciechowski, J. P.; Leonardo, V.; Wang, Y.; Pashuck, E. T.; Yarovsky, I.; Stevens, M. M. Residue-Specific Solvation-Directed Thermodynamic and Kinetic Control over Peptide Self-Assembly with 1D/2D Structure Selection. *ACS Nano* **2019**, *13* (2), 1900–1909.
16. Ozkan, A. D.; Tekinay, A. B.; Guler, M. O.; Tekin, E. D. Effects of Temperature, PH and Counterions on the Stability of Peptide Amphiphile Nanofiber Structures. *RSC Adv.* **2016**, *6* (106), 104201–104214.
17. Zhang, S.; Alberstein, R. G.; De Yoreo, J. J.; Tezcan, F. A. Assembly of a Patchy Protein into Variable 2D Lattices via Tunable Multiscale Interactions. *Nat Commun* **2020**, *11* (1), 3770.
18. Jiao, F.; Wu, X.; Jian, T.; Zhang, S.; Jin, H.; He, P.; Chen, C.-L.; De Yoreo, J. J. Hierarchical Assembly of Peptoid-Based Cylindrical Micelles Exhibiting Efficient Resonance Energy Transfer in Aqueous Solution. *Angewandte Chemie International Edition* **2019**, *58* (35), 12223–12230.
19. Shevchenko, E. V.; Talapin, D. V.; Kotov, N. A.; O'Brien, S.; Murray, C. B. Structural Diversity in Binary Nanoparticle Superlattices. *Nature* **2006**, *439* (7072), 55–59.
20. Lunn, D. J.; Finnegan, J. R.; Manners, I. Self-Assembly of "Patchy" Nanoparticles: A Versatile Approach to Functional Hierarchical Materials. *Chem. Sci.* **2015**, *6* (7), 3663–3673.
21. Boles, M. A.; Talapin, D. V. Binary Assembly of PbS and Au Nanocrystals: Patchy PbS Surface Ligand Coverage Stabilizes the CuAu Superlattice. *ACS Nano* **2019**, *13* (5), 5375–5384.
22. Lee, H.-Y.; Shin, S. H. R.; Drews, A. M.; Chirsan, A. M.; Lewis, S. A.; Bishop, K. J. M. Self-Assembly of Nanoparticle Amphiphiles with Adaptive Surface Chemistry. *ACS Nano* **2014**, *8* (10), 9979–9987.
23. Abécassis, B.; Tessier, M. D.; Davidson, P.; Dubertret, B. Self-Assembly of CdSe Nanoplatelets into Giant Micrometer-Scale Needles Emitting Polarized Light. *Nano Lett.* **2014**, *14* (2), 710–715.
24. Santos, P. J.; Cheung, T. C.; Macfarlane, R. J. Assembling Ordered Crystals with Disperse Building Blocks. *Nano Lett.* **2019**, *19* (8), 5774–5780.
25. Santos, P. J.; Cao, Z.; Zhang, J.; Alexander-Katz, A.; Macfarlane, R. J. Dictating Nanoparticle Assembly via Systems-Level Control of Molecular Multivalency. *J. Am. Chem. Soc.* **2019**, *141* (37), 14624–14632.
26. Ni, B.; Fu, C.; Pan, S.; He, L.; Lin, Z.; Peng, J. Semiconducting Spaghetti-like Organic–Inorganic Nanojunctions via Sequential Self-Assembly of Conjugated Polymers and Quantum Dots. *Chem. Mater.* **2022**, *34* (2), 847-853.
27. Kubo, N.; Yamauchi, M.; Yamamoto, S.; Masuo, S. Elucidation of the Mechanism of Quantum Dot Arrangement Based on Self-Assembly of an Azobenzene Derivative. *BCSJ* **2021**, *94* (6), 1799–1803.
28. DeStefano, A. J.; Segalman, R. A.; Davidson, E. C. Where Biology and Traditional Polymers Meet: The Potential of Associating Sequence-Defined Polymers for Materials Science. *JACS Au* **2021**, *1* (10), 1556–1571.
29. Li, Z.; Cai, B.; Yang, W.; Chen, C.-L. Hierarchical Nanomaterials Assembled from Peptoids and Other Sequence-Defined Synthetic Polymers. *Chem. Rev.* **2021**, *121* (22), 14031–14087.

30. Sun, J.; Zuckermann, R. N. Peptoid Polymers: A Highly Designable Bioinspired Material. *ACS Nano* **2013**, *7* (6), 4715–4732.
31. Jin, H.; Ding, Y.-H.; Wang, M.; Song, Y.; Liao, Z.; Newcomb, C. J.; Wu, X.; Tang, X.-Q.; Li, Z.; Lin, Y.; Yan, F.; Jian, T.; Mu, P.; Chen, C.-L. Designable and Dynamic Single-Walled Stiff Nanotubes Assembled from Sequence-Defined Peptoids. *Nat Commun* **2018**, *9* (1), 270.
32. Jin, H.; Jiao, F.; Daily, M. D.; Chen, Y.; Yan, F.; Ding, Y.-H.; Zhang, X.; Robertson, E. J.; Baer, M. D.; Chen, C.-L. Highly Stable and Self-Repairing Membrane-Mimetic 2D Nanomaterials Assembled from Lipid-like Peptoids. *Nat Commun* **2016**, *7* (1), 12252.
33. Wu, C. W.; Sanborn, T. J.; Huang, K.; Zuckermann, R. N.; Barron, A. E. Peptoid Oligomers with α-Chiral, Aromatic Side Chains: Sequence Requirements for the Formation of Stable Peptoid Helices. *J. Am. Chem. Soc.* **2001**, *123* (28), 6778–6784.
34. Robertson, E. J.; Battigelli, A.; Proulx, C.; Mannige, R. V.; Haxton, T. K.; Yun, L.; Whitelam, S.; Zuckermann, R. N. Design, Synthesis, Assembly, and Engineering of Peptoid Nanosheets. *Acc. Chem. Res.* **2016**, *49* (3), 379–389.
35. Sun, J.; Jiang, X.; Lund, R.; Downing, K. H.; Balsara, N. P.; Zuckermann, R. N. Self-Assembly of Crystalline Nanotubes from Monodisperse Amphiphilic Diblock Copolypeptoid Tiles. *PNAS* **2016**, *113* (15), 3954–3959.
36. Xuan, S.; Jiang, X.; Spencer, R. K.; Li, N. K.; Prendergast, D.; Balsara, N. P.; Zuckermann, R. N. Atomic-Level Engineering and Imaging of Polypeptoid Crystal Lattices. *PNAS* **2019**, *116* (45), 22491–22499.
37. Hammons, J. A.; Baer, M. D.; Jian, T.; Lee, J. R. I.; Weiss, T. M.; De Yoreo, J. J.; Noy, A.; Chen, C.-L.; Van Buuren, A. Early-Stage Aggregation and Crystalline Interactions of Peptoid Nanomembranes. *J. Phys. Chem. Lett.* **2021**, *12* (26), 6126–6133.
38. Ma, X.; Zhang, S.; Jiao, F.; Newcomb, C. J.; Zhang, Y.; Prakash, A.; Liao, Z.; Baer, M. D.; Mundy, C. J.; Pfaendtner, J.; Noy, A.; Chen, C.-L.; De Yoreo, J. J. Tuning Crystallization Pathways through Sequence Engineering of Biomimetic Polymers. *Nature Mater* **2017**, *16* (7), 767–774.
39. Wang, M.; Song, Y.; Zhang, S.; Zhang, X.; Cai, X.; Lin, Y.; Yoreo, J. J. D.; Chen, C.-L. Programmable Two-Dimensional Nanocrystals Assembled from POSS-Containing Peptoids as Efficient Artificial Light-Harvesting Systems. *Science Advances* **2021**, *7* (20), No. eabg1448.
40. Yan, F.; Liu, L.; Walsh, T. R.; Gong, Y.; El-Khoury, P. Z.; Zhang, Y.; Zhu, Z.; De Yoreo, J. J.; Engelhard, M. H.; Zhang, X.; Chen, C.-L. Controlled Synthesis of Highly-Branched Plasmonic Gold Nanoparticles through Peptoid Engineering. *Nat Commun* **2018**, *9* (1), 2327.
41. Monahan, M.; Cai, B.; Jian, T.; Zhang, S.; Zhu, G.; Chen, C.-L.; Yoreo, J. J. D.; Cossairt, B. M. Peptoid-Directed Assembly of CdSe Nanoparticles. *Nanoscale* **2021**, *13* (2), 1273–1282.
42. Ma, J.; Cai, B.; Zhang, S.; Jian, T.; De Yoreo, J. J.; Chen, C.-L.; Baneyx, F. Nanoparticle-Mediated Assembly of Peptoid Nanosheets Functionalized with Solid-Binding Proteins: Designing Heterostructures for Hierarchy. *Nano Lett.* **2021**, *21* (4), 1636–1642.
43. Merrill, N. A.; Yan, F.; Jin, H.; Mu, P.; Chen, C.-L.; Knecht, M. R. Tunable Assembly of Biomimetic Peptoids as Templates to Control Nanostructure Catalytic Activity. *Nanoscale* **2018**, *10* (26), 12445–12452.

44. Yang, W.; Yin, Q.; Chen, C.-L. Designing Sequence-Defined Peptoids for Biomimetic Control over Inorganic Crystallization. *Chem. Mater.* **2021**, *33* (9), 3047–3065.
45. Knauf, R. R.; Lennox, J. C.; Dempsey, J. L. Quantifying Ligand Exchange Reactions at CdSe Nanocrystal Surfaces. *Chem. Mater.* **2016**, *28* (13), 4762–4770.
46. Bera, D.; Qian, L.; Tseng, T.-K.; Holloway, P. H. Quantum Dots and Their Multimodal Applications: A Review. *Materials (Basel)* **2010**, *3* (4), 2260–2345.
47. Huang, Y.; Cohen, T. A.; Sperry, B. M.; Larson, H.; Nguyen, H. A.; Homer, M. K.; Dou, F. Y.; Jacoby, L. M.; Cossairt, B. M.; Gamelin, D. R.; Luscombe, C. K. Organic Building Blocks at Inorganic Nanomaterial Interfaces. *Mater. Horiz.* **2022**, *9* (1), 61–87.
48. Mussa Farkhani, S.; Valizadeh, A. Review: Three Synthesis Methods of CdX (X = Se, S or Te) Quantum Dots. *IET Nanobiotechnology* **2014**, *8* (2), 59–76.
49. Liu, J.; Enomoto, K.; Takeda, K.; Inoue, D.; Pu, Y.-J. Simple Cubic Self-Assembly of PbS Quantum Dots by Finely Controlled Ligand Removal through Gel Permeation Chromatography. *Chem. Sci.* **2021**, *12* (30), 10354–10361.
50. Walravens, W.; De Roo, J.; Drijvers, E.; ten Brinck, S.; Solano, E.; Dendooven, J.; Detavernier, C.; Infante, I.; Hens, Z. Chemically Triggered Formation of Two-Dimensional Epitaxial Quantum Dot Superlattices. *ACS Nano* **2016**, *10* (7), 6861–6870.
51. Balazs, D. M.; Dirin, D. N.; Fang, H.-H.; Protesescu, L.; ten Brink, G. H.; Kooi, B. J.; Kovalenko, M. V.; Loi, M. A. Counterion-Mediated Ligand Exchange for PbS Colloidal Quantum Dot Superlattices. *ACS Nano* **2015**, *9* (12), 11951–11959.
52. Baumgardner, W. J.; Whitham, K.; Hanrath, T. Confined-but-Connected Quantum Solids via Controlled Ligand Displacement. *Nano Lett.* **2013**, *13* (7), 3225–3231.
53. Hartley, C. L.; Kessler, M. L.; Dempsey, J. L. Molecular-Level Insight into Semiconductor Nanocrystal Surfaces. *J. Am. Chem. Soc.* **2021**, *143* (3), 1251–1266.
54. Si, K. J.; Chen, Y.; Shi, Q.; Cheng, W. Nanoparticle Superlattices: The Roles of Soft Ligands. *Advanced Science* **2018**, *5* (1), 1700179.
55. Chen, Z.; O'Brien, S. Structure Direction of II−VI Semiconductor Quantum Dot Binary Nanoparticle Superlattices by Tuning Radius Ratio. *ACS Nano* **2008**, *2* (6), 1219–1229.
56. Chung, Y.-C.; Yang, C.-H.; Zheng, H.-W.; Tsai, P.-S.; Wang, T.-L. Synthesis and Characterization of CdS x Se 1−x Alloy Quantum Dots with Composition-Dependent Band Gaps and Paramagnetic Properties. *RSC Advances* **2018**, *8* (52), 30002–30011.
57. Kessler, M. L.; Dempsey, J. L. Mapping the Topology of PbS Nanocrystals through Displacement Isotherms of Surface-Bound Metal Oleate Complexes. *Chem. Mater.* **2020**, *32* (6), 2561–2571.
58. Hamachi, L. S.; Yang, H.; Plante, I. J.-L.; Saenz, N.; Qian, K.; Campos, M. P.; Cleveland, G. T.; Rreza, I.; Oza, A.; Walravens, W.; Chan, E. M.; Hens, Z.; Crowther, A. C.; Owen, J. S. Precursor Reaction Kinetics Control Compositional Grading and Size of CdSe1−xSx Nanocrystal Heterostructures. *Chem. Sci.* **2019**, *10* (26), 6539–6552.
59. Morris-Cohen, A. J.; Malicki, M.; Peterson, M. D.; Slavin, J. W. J.; Weiss, E. A. Chemical, Structural, and Quantitative Analysis of the Ligand Shells of Colloidal Quantum Dots. *Chem. Mater.* **2013**, *25* (8), 1155–1165.
60. Fisher, A. A. E.; Osborne, M. A.; Day, I. J.; Lucena Alcalde, G. Measurement of Ligand Coverage on Cadmium Selenide Nanocrystals and Its Influence on Dielectric Dependent Photoluminescence Intermittency. *Commun Chem* **2019**, *2* (1), 1–9.
61. De Roo, J.; Yazdani, N.; Drijvers, E.; Lauria, A.; Maes, J.; Owen, J. S.; Van Driessche, I.; Niederberger, M.; Wood, V.; Martins, J. C.; Infante, I.; Hens, Z. Probing Solvent–Ligand

Interactions in Colloidal Nanocrystals by the NMR Line Broadening. *Chem. Mater.* **2018**, *30* (15), 5485–5492.

62. Zuckermann, R. N.; Kerr, J. M.; Kent, S. B. H.; Moos, W. H. Efficient Method for the Preparation of Peptoids [Oligo(N-Substituted Glycines)] by Submonomer Solid-Phase Synthesis. *J. Am. Chem. Soc.* **1992**, *114* (26), 10646–10647.

APPENDIX A: COLLABORATIVE EFFORTS

The following work has been published in collaboration with those both at University of Washington and with other institutions. Transmission electron microscopy is a powerful tool for structural and elemental analysis both on a nano- and micrometer scale. The work highlighted below shows my electron microscopy contributions to this work and a brief summary of the results.

1) *Mapping the effects of physical and chemical reduction parameters on local atomic distributions within bimetallic nanoparticles*

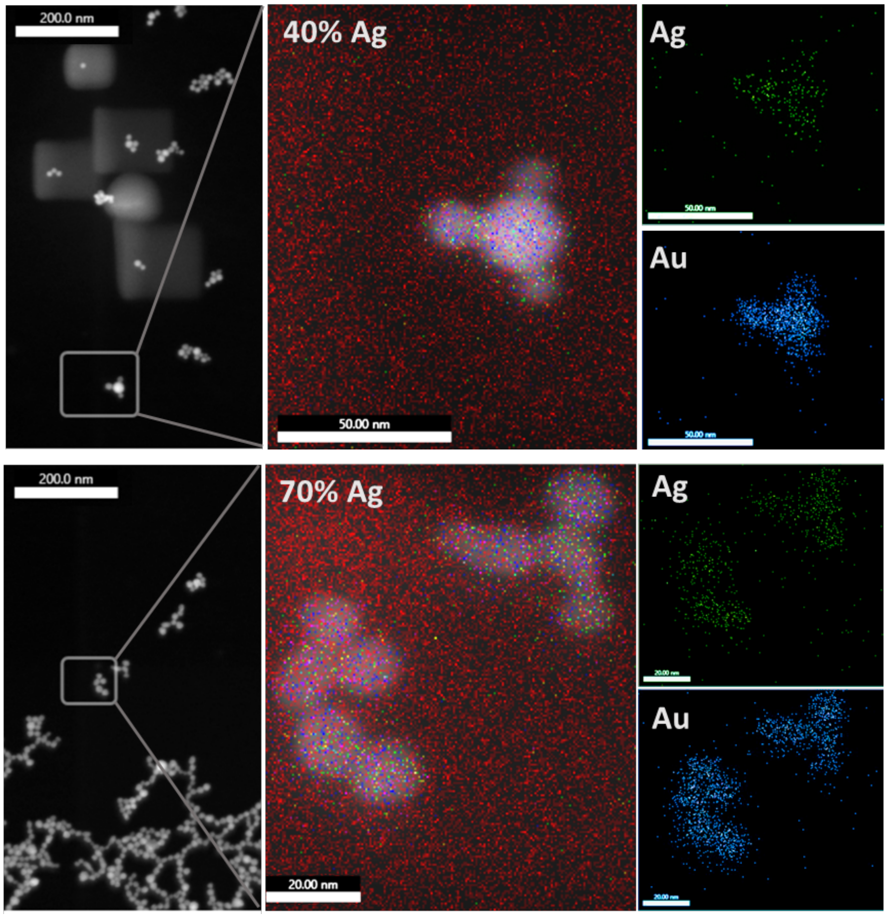

EDS maps of AgAuNPs made with a starting solution metal ratio of a) 40% Ag, and b) 70% Ag, corresponding to particles with an actual composition of 9 ± 3% and 34 ± 4% Ag, respectively.

Despite limitations of low resolution, in neither case is a bimodal population of Au and Ag NPs observed, and in fact Au does appear to be concentrated more heavily in the particle centers while Ag appears to reside more diffusely on particle surfaces and edges.

2) *Conjugated metal-organic macrocycles: Synthesis, characterization, and electrical conductivity*

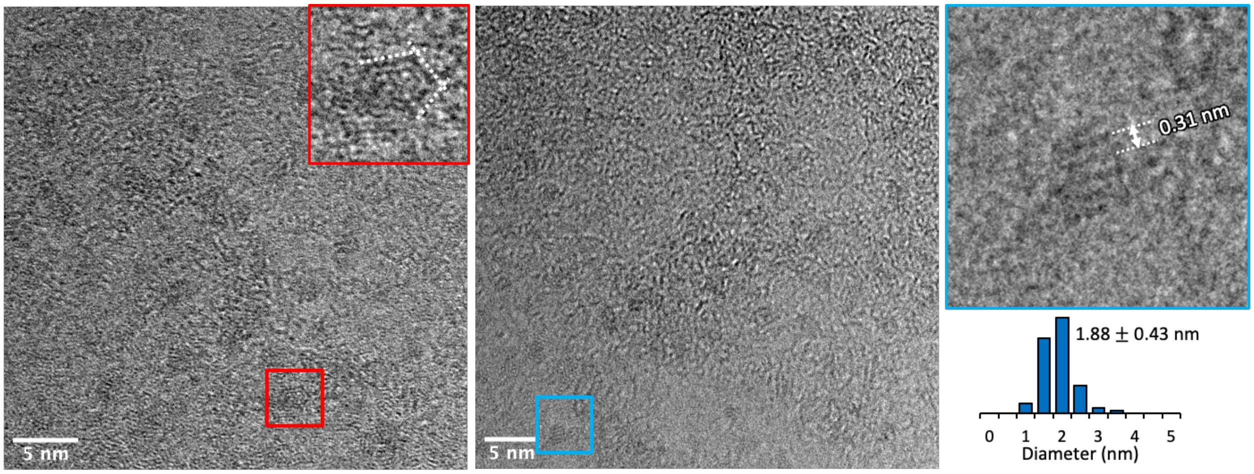

High-resolution TEM images of CuTOTP-OC4 MOFs on graphene showing the hexagonal nature of the macrocycles with a diameter of 1.88 nm (right, red) and their ability to stack into small assemblies with a spacing of 0.31 nm (left, blue). Images for CuTOTP-OC18 were not as clear with lower resolution and reduced contrast. We hypothesize that there is less stacking of the macrocycles due to steric bulk from the long carbon chain leading who a thinner, lower contrast particle.

3) *Covalent Functionalization of Nickel Phosphide Nanocrystals with Aryl-Diazonium Salts*

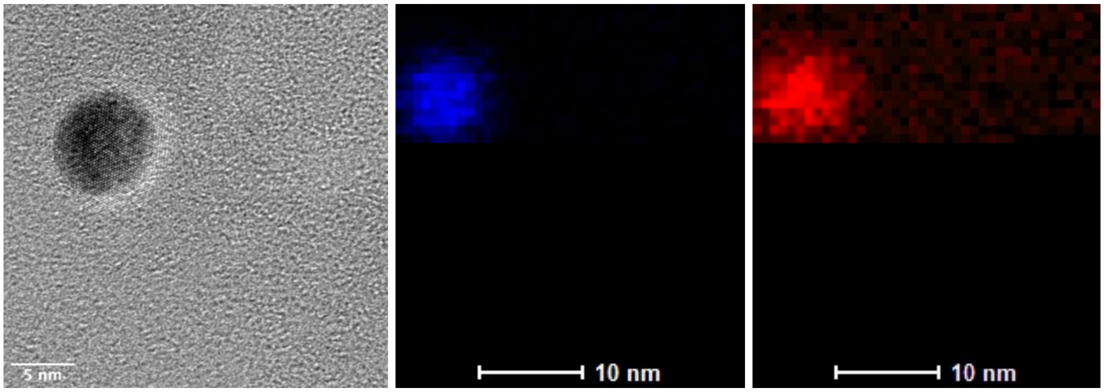

High-resolution TEM of Ni_2P nanoparticles with a phosphorus rich exterior seen by the lighter edge with lattice fringes after ligand stripping via chemical reagents (left). EDS of the nanoparticles also showed a more diffuse phosphorus (red) signal than nickel (blue), agreeing with the HR-TEM. Other attempts were made to remove surface ligands for EDS via plasma cleaning but the H_2/O_2 plasma caused fusion of the nanoparticles.

4) *Tuning the interfacial stoichiometry of InP core and InP/ZnSe core/shell quantum dots*

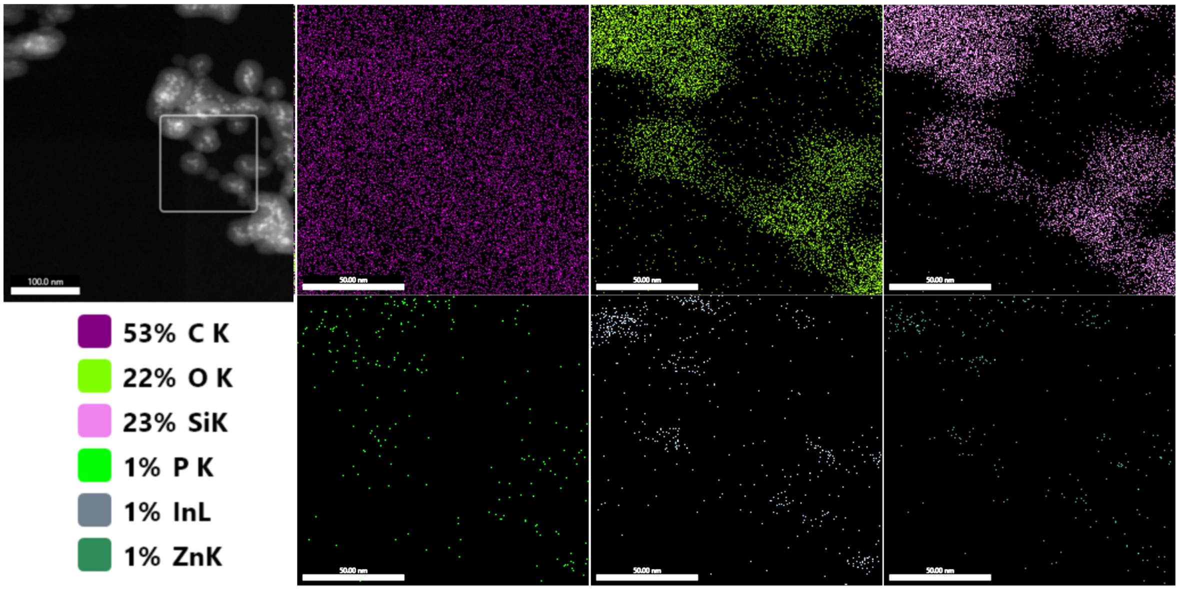

Initial studies looked at high-resolution images of core/shell InP QDs with different interfaces to look at morphology and monodispersity. No EDS images were obtained due to instability under the concentrated beam and lack of signal. In follow up studies with metal oxide interfaces we once again attempted EDS with too much instability. We decided to stabilize the sample by shelling in SiO_2 to protect the core and allow for longer scan times without destroying the sample. In combination with the new detector, longer scan times produced weak but interpretable signal showing co-localization of In (grey), Zn (dark green), and P (light green) for InP/ZnO QDs.

5) *Covalently Linked, Two-Dimensional Quantum Dot Assemblies*

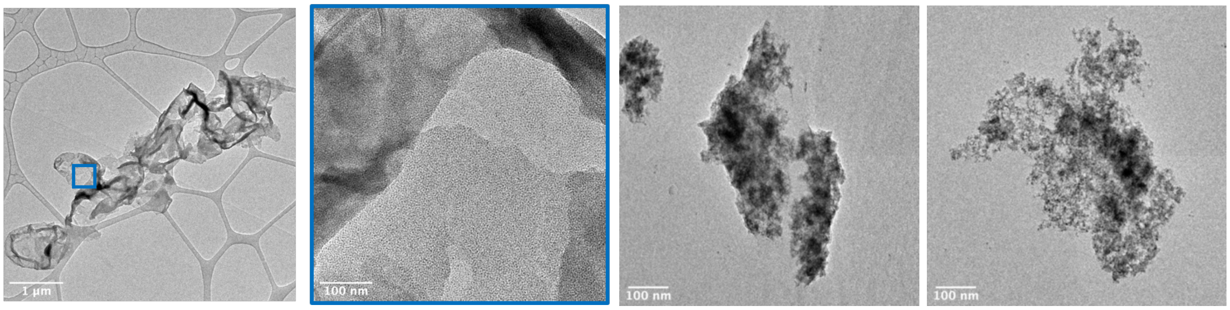

These studies focused on the assembly of CdSe and CdS QDs into large 2D sheets (left, middle left). We tracked the assemblies with time and the final structures using HR-TEM, tomography, and EDS. With changing the linker between QDs, ratio of linker to QD, and time we were able to track changes in the assemblies through QD-QD distances using HR-TEM. Tomography confirmed the 2D nature of the sheets and identified overlap areas (middle right) which without tilt (right) look like 3D amorphous regions. Using a bipyridine linker that can chelate Ni, we showed the ability for the sheets to absorb nickel using EDS to show co-localization of Cd, S, and Ni.

6) *Seeded Growth of Nanoscale Semiconductor Tetrapods: Generality and the Role of Cation Exchange*

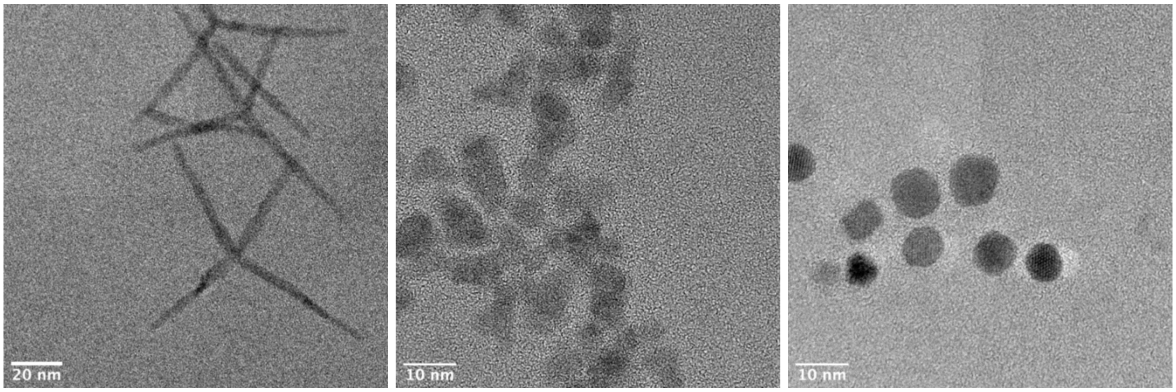

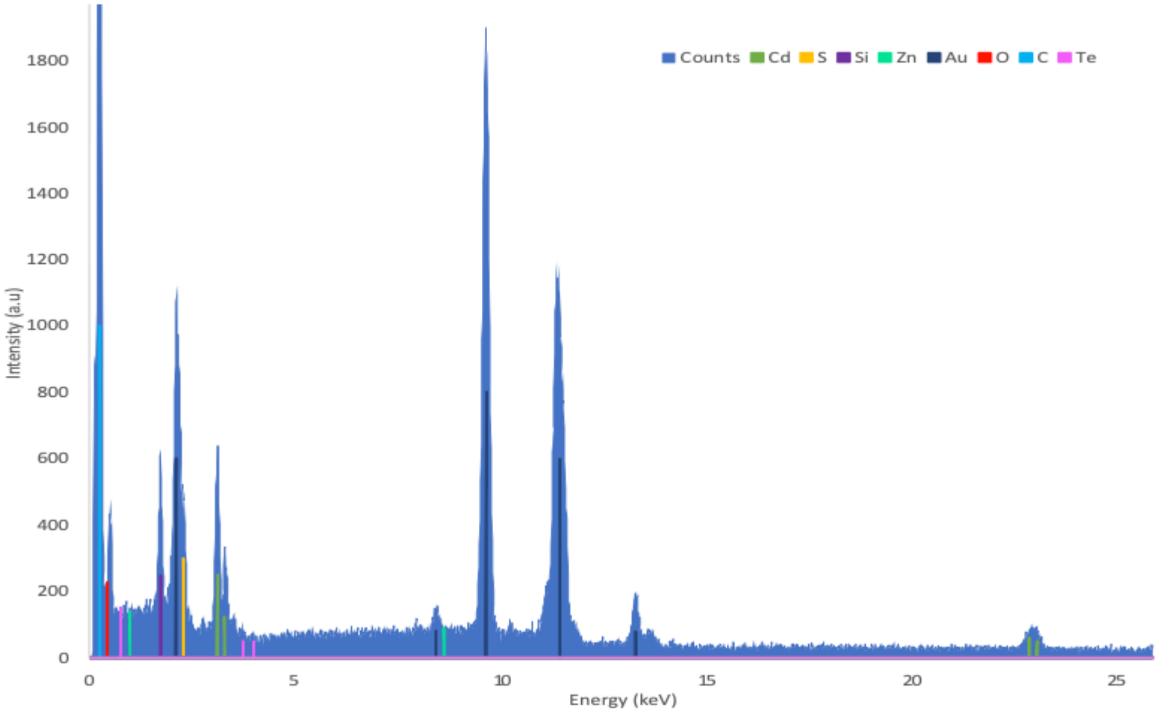

Tetrapods with CdS arms and differing cores were synthesized and characterized with TEM and EDS (left). We worked on optimizing signal in EDS to try to determine if the cores remained intact or underwent cation exchange with Cd. To optimize signal, we attempted to remove surface ligands via plasma treatment on the grid (middle) and chemical stripping in solution (right). Both methods destabilize the structures, likely due to the importance in ligand identity and binding strength in forming these structures. Point scans were used to get broad surveys of the material and confirm presence of the core elements. Representative EDS showing strong signals were observed for cadmium and sulfur with weak signal from zinc and tellurium obtained on gold grids.

7) *Synthesis of In37P20(O2CR)51 Clusters and Their Conversion to InP Quantum Dots*

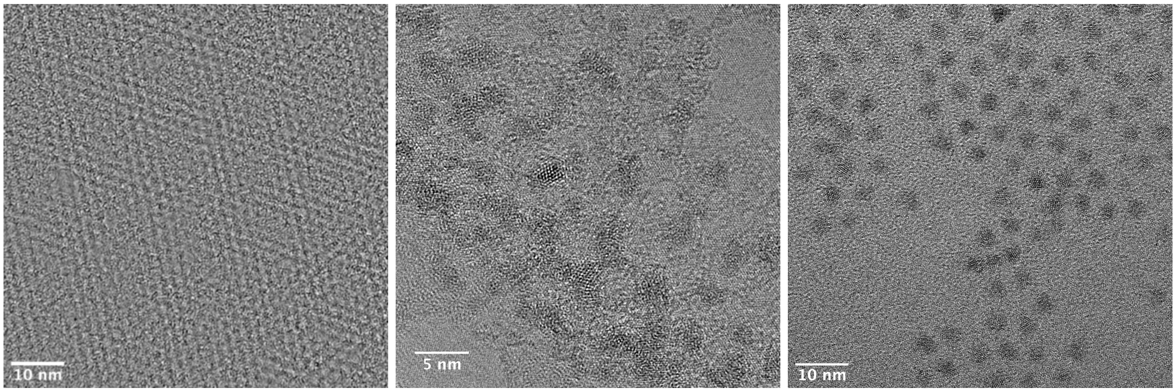

This work focused on detailing the synthesis and characterization of InP magic size clusters and QDs using the clusters as single source precursors. The methods described cluster synthesis using two different indium sources and the generalizability of the ligand. For QD synthesis, two different methods were discussed either by hot injecting the clusters into solvent or slowly heating the cluster solution. High-resolution TEM of the clusters show the high monodispersity of the clusters (left), seen by superlattice formation upon drying, and the ellipsoid shape of the C2 symmetry (middle). The InP QDs synthesized via this method also show high monodispersity and crystallinity by TEM (right).

References:

1. Johnson, H. M.; Dasher, A. M.; Monahan, M.; Seifert, S.; Moreau, L. M. Mapping the Effects of Physical and Chemical Reduction Parameters on Local Atomic Distributions within Bimetallic Nanoparticles. *Nanoscale* **2022**, *14* (12), 4519–4530.
2. Zasada, L. B.; Guio, L.; Kamin, A. A.; Dhakal, D.; Monahan, M.; Seidler, G. T.; Luscombe, C. K.; Xiao, D. J. Conjugated Metal–Organic Macrocycles: Synthesis, Characterization, and Electrical Conductivity. *J. Am. Chem. Soc.* **2022**, *144* (10), 4515–4521.

3. Murphy, I. A.; Rice, P. S.; Monahan, M.; Zasada, L. B.; Miller, E. M.; Raugei, S.; Cossairt, B. M. Covalent Functionalization of Nickel Phosphide Nanocrystals with Aryl-Diazonium Salts. *Chem. Mater.* **2021**, *33* (24), 9652–9665.
4. Park, N.; Eagle, F. W.; DeLarme, A. J.; Monahan, M.; LoCurto, T.; Beck, R.; Li, X.; Cossairt, B. M. Tuning the Interfacial Stoichiometry of InP Core and InP/ZnSe Core/Shell Quantum Dots. *J. Chem. Phys.* **2021**, *155* (8), 084701.
5. Ritchhart, A.; Monahan, M.; Mars, J.; Toney, M. F.; De Yoreo, J. J.; Cossairt, B. M. Covalently Linked, Two-Dimensional Quantum Dot Assemblies. *Langmuir* **2020**, *36* (33), 9944–9951.
6. Enright, M. J.; Dou, F. Y.; Wu, S.; Rabe, E. J.; Monahan, M.; Friedfeld, M. R.; Schlenker, C. W.; Cossairt, B. M. Seeded Growth of Nanoscale Semiconductor Tetrapods: Generality and the Role of Cation Exchange. *Chem. Mater.* **2020**, *32* (11), 4774–4784.
7. Park, N.; Monahan, M.; Ritchhart, A.; Friedfeld, M. R.; Cossairt, B. M. Synthesis of In37P20(O2CR)51 Clusters and Their Conversion to InP Quantum Dots. *JoVE (Journal of Visualized Experiments)* **2019**, No. 147, e59425.

APPENDIX B: TEM TIPS AND BEST PRACTICES

1) Sample preparation considerations

a) Substrate on the grid

Lacey carbon grids are useful for samples less that 20 nm in size. The lacey carbon can be used to help with alignment of the beam when there is no visible sample. We typically use ultrathin lacey carbon (amorphous carbon is 3-4 nm in thickness) since our materials are small and low contrast.

Graphene grids are great for low contrast samples. The grids are a few monolayers of graphene which greatly reduces the background signal and makes the sample have higher contrast. Be aware of the background pattern from graphene, since it is no longer amorphous you can get a pattern from the background just to do the graphene. Remember to be very careful not to bend or manipulate the grid too much, limit time under vacuum, and do not store in the glovebox (the atmosphere tends to volatiles that can damage the carbon support) as the thin carbon layer is very delicate and easily damaged. When imaging, make sure to zoom way out (730x) and find a section that is not broken and does not have multilayers of graphene (looks uniform and even).

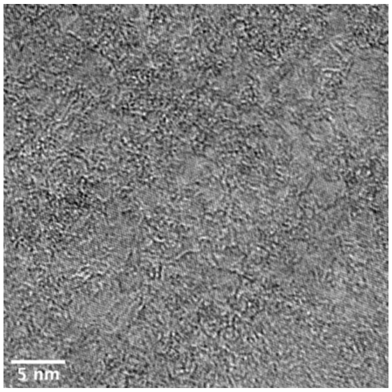

InP-OA on graphene showing the background pattern of graphene

There are many other supports available to buy. Different supports can help both due to thickness (or overall contrast) and the hydrophobicity of the substrate. For example, you can but silicon nitride grids that upon plasma treatment will be very hydrophilic, allowing for a hydrophilic sample to better disperse onto the grid. Such a sample would likely clump on regular carbon due to the hydrophobic nature.

b) *Solvents for dispersion and sample preparation*

A general rule of thumb is to pick a solvent that your sample is soluble in. It is important to pick a solvent that solubilizes your sample well as insufficient solubility will lead to an aggregated sample without well-defined particles. Beyond that, your solvent choice can vary based on the type of information you want to get out of the sample. By choosing a solvent that evaporates quickly, you sample is more likely to randomly dry and target different sample orientations (this will allow you to theoretically remove any bias or preference for one side or facet of a nanoparticle to dry against the carbon). A slow evaporating solvent will lead to clumping of the sample which can form superlattices, if monodispersed, or aggregates if excess organics such as ligands are present. If your solvent too high or a boiling point to evaporate well or just slow, you can dab off the grid with a KimWipe then set it on top of a KimWipe to dry. Due to the high surface tension, water has a high tendency to clump/concentrate the sample. To avoid this, dropcast the sample, let settle for 10-15 min, dab off the excess water and let it dry fully. Another way to disrupt drying effects is to let the grid dry/ prep it as you normally would then put it immediately under vacuum (rather than waiting a few hours). This will disrupt any drying effects and favor random orientation of nanoparticles.

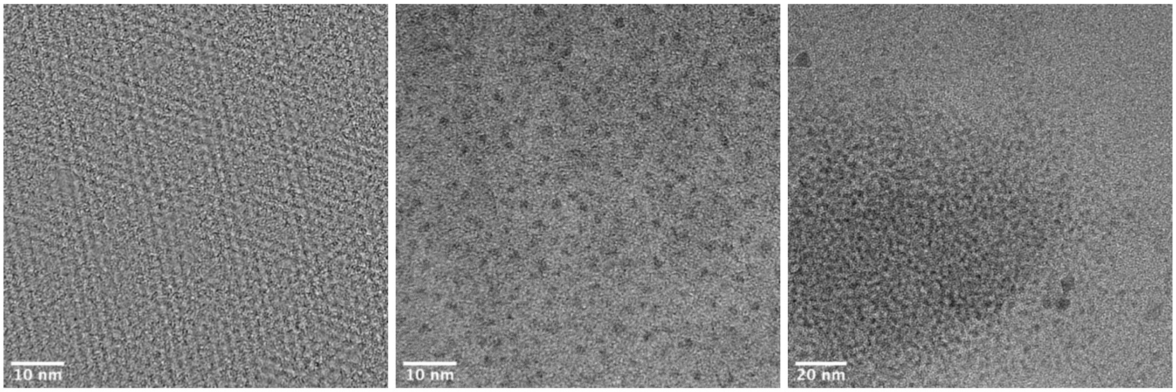

InP-OA MSCs with slow drying on graphene, rapid drying on graphene, and MEEAA-CdSe with residual NMP

c) *Surface chemistry*

The surface chemistry of your sample will have a large impact on how the sample dries, relative to one another and the spacing between nanoparticles. Ligands that repel each other, such as long chain fatty acids, will give well-defied spacing between the particles with limited overlap between particles (assuming concentration isn't too high). Shorter ligands or ones with functional groups at the outward facing ends tend to stick together causing aggregation of the particles and poor separation upon drying. The distance between nanoparticles should correlate to the length of the ligand accounting for two ligands, often with some extent of interdigitation of the two ligand shells.

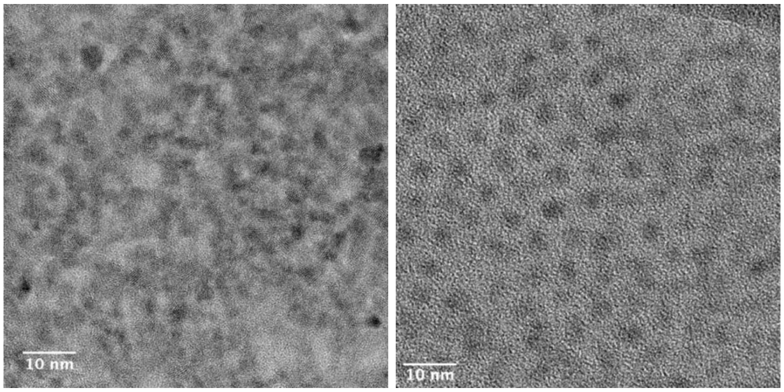

Cys-CdSe QDs with high degree of overlap and CdSe-OA QDs with large spacing and no overlap.

d) Staining samples for increased contrast

Negative staining is useful for carbon-based or other low contrast materials such a peptoids, proteins, or polymers. This is done by using a high contrast stain, often a metallic solution, that will surround the sample, inverting the contrast to that the lighter areas correspond to the sample. Typically, we use a 2% solution of phosphotungstic acid (PTA). Apply 5uL to a dry grid that already has your sample deposited. Allow the grid to sit for 3-5 min in a low ventilation area (not in a hood or near the sash) then dab off the grid and allow to dry while resting on a KimWipe.

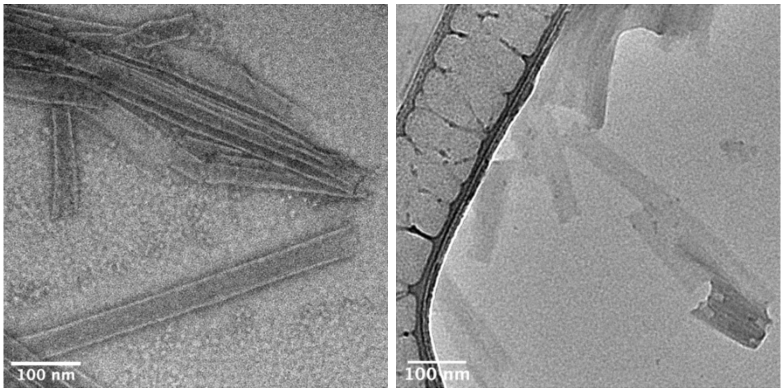

Peptoid tubes with PTA stain in BF vs without a stain in BF with an overfocus to highlight tube edges.

2) Getting started and aligning the beam

a) Find an interesting grid hole by zooming out all the way (around 730 mag) and evaluate the grid holes. Pick an area that looks representative of the whole grid and that you know has sample. To identify an area that has sample will either have visible chunks, a blurred look near the grid bars or decreased overall brightness or could just look like a plan area. Avoid areas that are unlike the other grid areas so that you aren’t being bias by choosing an area that looks the best. It is also good to check multiple grid hole to make sure that you have representative images.

b) Do your initial alignment of the microscope but do not spend all your time trying to get a perfect alignment at 125x. Once you find an interesting area, align the beam as you go up in magnification. Every time you want to image at a new magnification higher than 125x, realign the pivot points (x,y) and the beam shift. This will help you get a better alignment then if you spent a lot of time on one alignment at 125x. The misalignment will also be more noticeable as you go up in magnification so that's why it's good to align as you go up in magnification. It is also a good idea to realign when changing the grid hole or moving far away from the area you were just imaging.

c) Utilize the lacey carbon for initial alignments, especially when imaging sample that is hard to get into focus without an aligned beam (too small or too thick).

d) Change spot size to fit your needs (3-5, typically). The higher the spot size the less bright the beam will be but the better for high resolution and small materials. Most materials we work with needs the smaller spot size (5).

3) Troubleshooting and getting a good image

a) Blurry/smeared image

Images are often blurry or look smeared when the objective is astigmated or the sample is drifting. For the objective, it can be fixed (rounded) using the FFT. For sample drift, there could be a variety of reasons. The sample may not be totally dry, the stage may be moving and needs to settle (~10-30 min), there could be environmental vibrations, or there could be sample charging. For environmental vibrations, use the hat on the outside of the holder and image at a time when the campus is quieter (the morning, evening, or weekend). To reduce sample charging, use a smaller C2 aperture (higher number) to reduce the number of electrons hitting the sample.

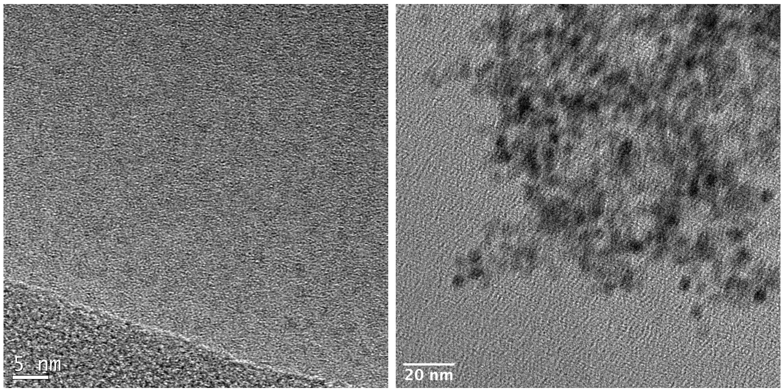

An image where the sample is drifting and where the objective is astigmated.

b) Beam damage and grainy images

These issues are related to a moving sample but rather than being an external issue such as vibrations, it is likely due to issues within the sample. Beam damage and poor resolution can be due to the sample not being fully dry or the sample not being purified enough. If there are excess organics such as solvent or ligands they can be easily damaged by the beam, leaving dark rings, and also reduce the resolution. This can be fixed by working on sample prep/purification or trying another grid hole closer to the edge of the grid, where it is likely that less sample is deposited. These types of images can also be a result of poor focus and too thick of carbon substrate. For better focus, try focusing on a single feature rather than the entire image and using the FFT to find ideal focus. The substrate thickness can be resolved by using a thinner carbon support such as graphene or flipping the grid over so that the sample side is up in the microscope.

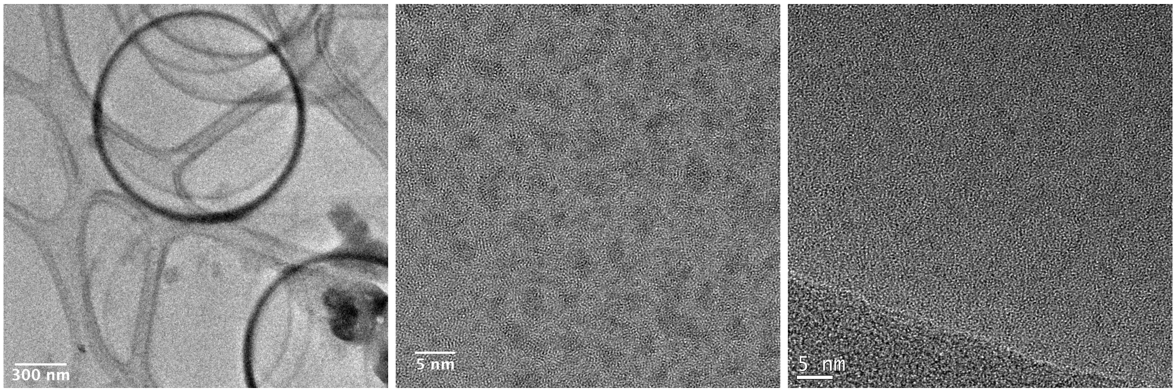

Image displaying beam damage due to excess carbon, an example of an InP cluster sample that could benefit from being flipped, and a sample that has too thick of a carbon support.

c) *Poor contrast*

Poor contrast is often a result of a few different issues. The sample could be too thick (try a different area, work on sample prep) or generally a low contrast sample (try thinner grid like graphene, put sample side up in microscope, insert the OA).

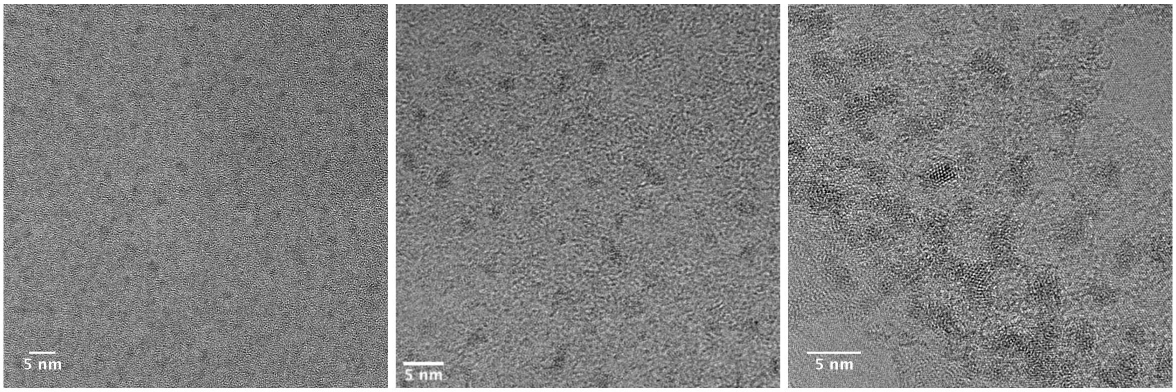

InP MSCs on lacey carbon, on graphene (sample side up).

d) *General lack of resolution*

Lack of resolution is most often due to poor alignment of the beam or issues with sample prep. As discussed above, a good alignment can be achieved by doing small alignments as you increase magnification (pivot points and beam shift) and completely redoing the alignment when changing areas on the grid (e.g., moving to another grid hole). Additionally, remember to use the lacey carbon for initial alignments and increase the spot size as needed for higher resolution.

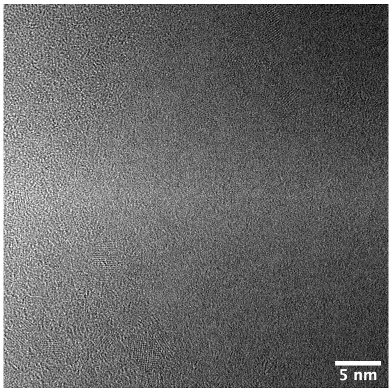

Beam shift is misaligned causing a color gradient across the image.

Sample preparation also has a significant impact on the resolution that can be acquired when imaging. For example, if the sample is too thick, poorly dispersed, or has high excess of carbon it will be very hard to get a clear image. Having clumped or thick sample areas means there is more material the electrons must pass through before hitting the camera making the image worse and harder to focus as it can only focus on a small area, making a larger amount of material out of focus and convoluting the image. To better disperse the sample, make sure that it is in a solvent that solubilizes it well to reduce aggregation and evaporates relatively quickly to reduce clumping due to drying effects. Excess ligand can also lead to aggregation of the sample and excess carbon on the grid that is not only visible but will increase the beam damage. Excess ligand can be avoided by better purifying the sample via crashouts/columns or doing a total ligand removal. Ligands can be removed in solution via chemical processes (REF) or after deposition using plasma cleaning to remove carbon on the surface. While ligand removal greatly increases resolution and limits any beam damage, it can alter your material via destruction of fine structures (ripening) or lead to fusing of particles together.

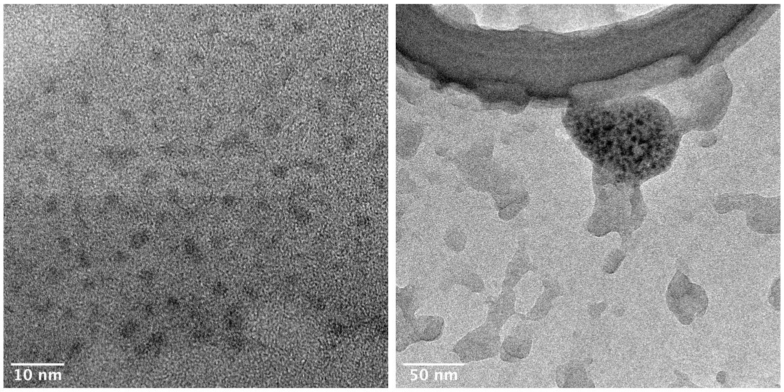

QDs showing excess ligand or carbon on the grid that leaves a shadowing effect (left) or separate structures with aggregation of the QDs (right).

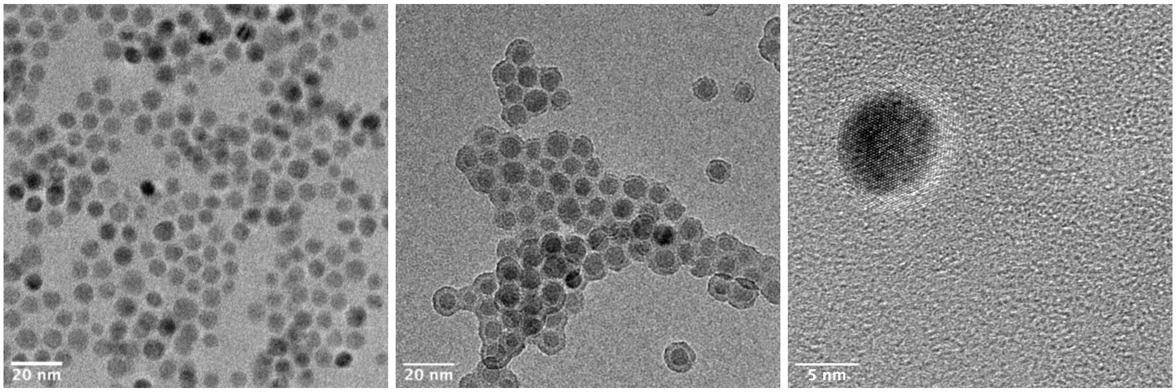

Ni_2P QDs upon synthesis and after ligand removal via plasma treatment on a grid and after chemical removal in solution showing fusion upon plasma treatment but increased resolution via the solvent route.

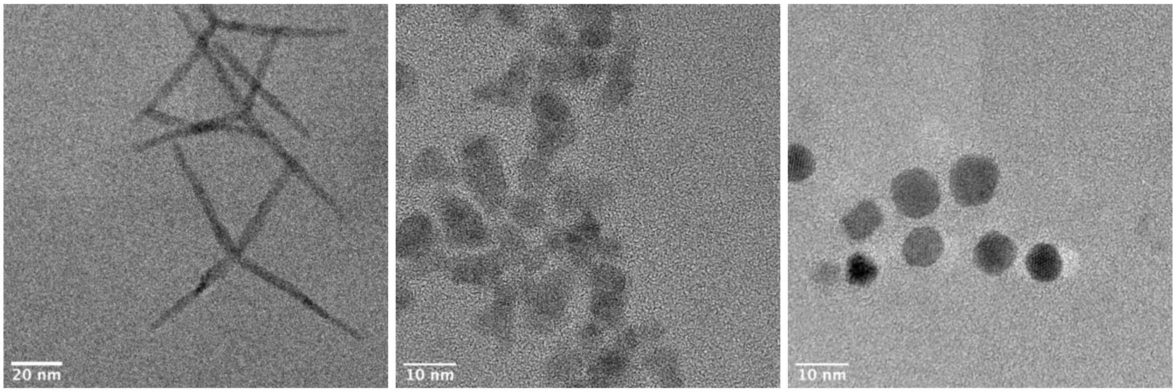

Tetrapods upon synthesis and after ligand removal via plasma treatment on a grid and after chemical removal in solution showing ripening in both cases.

e) Utilizing focal points for different information

Imaging conditions and parameters vary based on sample and information you hope to gain. Specifically, utilizing focus for a sample can give you different information about the structure. When in focus, the image will have minimal contrast with diffuse edges. This type of imaging can be useful for gaining internal structural information such as crystal structure by identifying lattice fringes and d-spacing at high magnifications. An in-focus image isn't as useful at lower magnifications as you'll be too zoomed out to see lattice fringes and not have well defined particles edges. By imaging slightly defocused at lower magnifications, the edges of particles will become more defined and easier to distinguish. This type of focus is best for particle size analysis and general morphology.

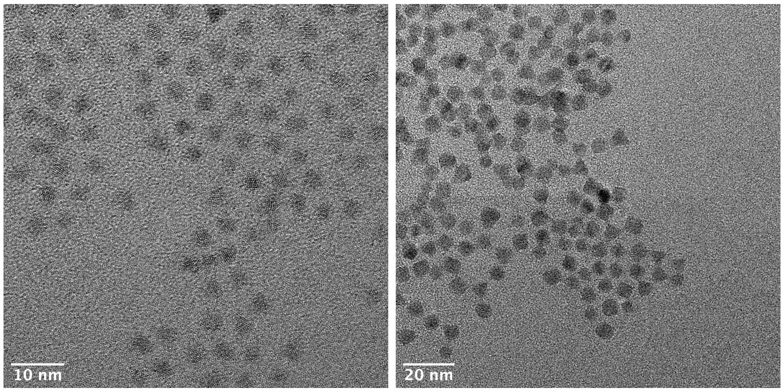

In-focus InP QDs where the edges are poorly defined but internal lattice fringes can be identified. Slightly defocused image of CdS QDs where the edges are well defined, but no lattice information is available.

4) Imaging tips based on type of sample

a) *Clusters and other low contrast materials (<2nm)*

Small, low contrast samples are some of the hardest to identify as they easily blend into the background of an image. When imaging these types of samples, sample prep and beam alignment is key. To start, make sure sample is well purified to limit carbon contamination as you will need to sit in one place on a grid for a while to align the beam and let it stabilize and will have to go to a high magnification. Letting the stage stabilize prior to imaging (put the holder in and let it sit for ~15-30 min) is important for high resolution as at higher magnifications small drifts are more noticeable. Imaging when the campus is quieter (mornings, evenings, or weekends) and using the hat over the holder will also limit stage drift due to environmental vibrations. It is also important to limit the thickness of the substrate, like using a graphene grid, as when your sample is only 2 nm thick, a 4 nm amorphous carbon layer will be dominating relative to your sample. It can also be helpful to place the grid sample side up in the microscope and let the beam interact with your sample before the carbon.

Identifying the sample with confidence can be the hardest part for low contrast materials. To start, use the lacey carbon to align the microscope as you will not be able to see clusters without doing a preliminary alignment. Slowly go up in magnification, aligning as you go (specifically ppx, ppy, and beam shift), and begin looking for clusters (a good magnification to scan some areas while being able to see clusters is 125x-250x). If you're having a hard time finding them, look near the edges of lacey carbon as sample tends to dry on the edges and/or zoom out and pick a grid hold that has some aggregation or signs of sample. Once you've found an area that you think has some sample, go to the higher magnifications, and look for a feature that remains present throughout the random noise (using the camera with a 0.1s refresh rate). When you have identified what you think is a cluster (the previously mentioned feature), move in and out of focus and see if the feature remains. If the feature remains through different focal points, let the sample sit for ~3-5 min to make sure it is well settled and not drifting then collect an image. I recommend collecting at a few different focal points as it will be hard to focus by eye and the longer acquisition time of taking an image (relative to the 0.1s refresh) will give you a better image to identify in focus. I also recommend collecting for 2-3s (rather than 1s), if you have no drift, so you get a better signal to noise ratio. A key to identifying clusters or other small materials is the relative "texture" within an image. Noise is very characteristic and random throughout the background amorphous carbon. Your sample will disrupt that texture or random noise with sharp lines, well defined shapes, or persistence throughout "searching".

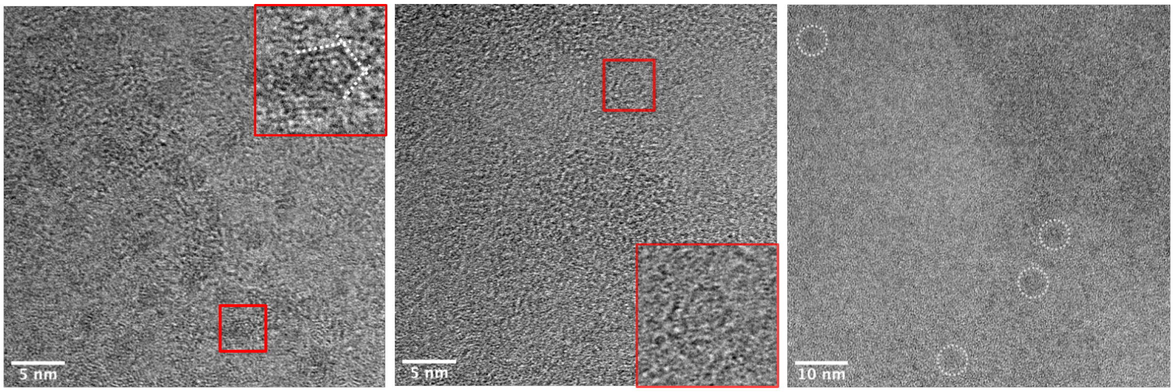

2 nm MOFs on graphene (left and middle) where particles display a well-defined edge relative to the graphene. The same MOFs on ultra-thin carbon (3-4 nm) where the structures are harder to identify but present as seen by a shadowing (white dashed lines).

b) Peptoids/organics

Carbon-based materials are much lower contrast and tend to be more susceptible to beam damage. To help with beam damage, align the microscope away from the sample (use the lacey carbon) and focus right next to the area (using the FFT or lacey carbon) then move other and collect image. In BF mode, carbon-based materials are more stable (less damage) but harder to identify. For larger carbon-based materials like peptoids, you can image them in BF by over focusing to get a darker rim around the material. You can also stain the sample (see above) to better identify structures. Another way to identify them without additives, especially for thinner samples, is STEM or dark field mode. This is only useful for more stable structures as it will have a greater chance of beam damage with the concentrated beam associated with STEM.

c) Beam sensitive materials

When your sample is beam sensitive (degrades or transforms under the beam), you want to limit the electron dose your sample gets. Your sample could be beam sensitive either from a total amount of electrons encountered (X number of electrons) or to a rate of exposure (a certain number of electrons per second). In both cases, you want to limit the time your sample is illuminated. To do this, avoid illuminating large areas (don't zoom way out in the beginning) and align the microscope away from the sample (using lacey carbon). Once the beam is aligned, move over to sample and image quickly (adjust focus at the magnification you want to image right next to sample then move over). You can also try other techniques such as cryo-EM or low dose that can help reduce beam damage or beam effects, but they need special training and may require additional optimization.

d) Conducting/charging

If you have a sample that is subject to charging (a conductive sample) then you can take a few precautions to limit this. Charging can most often be identified by significant sample drift, even after you've let the holder settle and been imaging for a while. To limit charging, you want to reduce the number of electrons interacting with your sample by choosing a smaller C2 condenser, smaller spot size (bigger number), or adding apertures such as the objective. You can also mitigate the effects of drifting by using a short acquisition time and going to a lower magnification.

e) Identifying excess carbon/ need for more purification

A sample that needs more purification is most often identifiable by amorphous regions or high amounts of beam damage. You may see darkness around your particles or clumps or gunk, likely excess carbon. A non-pure sample may also appear grainy and not give clear images at high resolution. You can check with other techniques such as XRD to see if there are excess organics or if your sample is crystalline. If you see nanoparticles peaks via XRD but cannot achieve lattice fringes, then the sample requires more purification. You can also remove excess carbon after preparing the grid to check by running the grid with sample through the plasma cleaner prior to imaging.

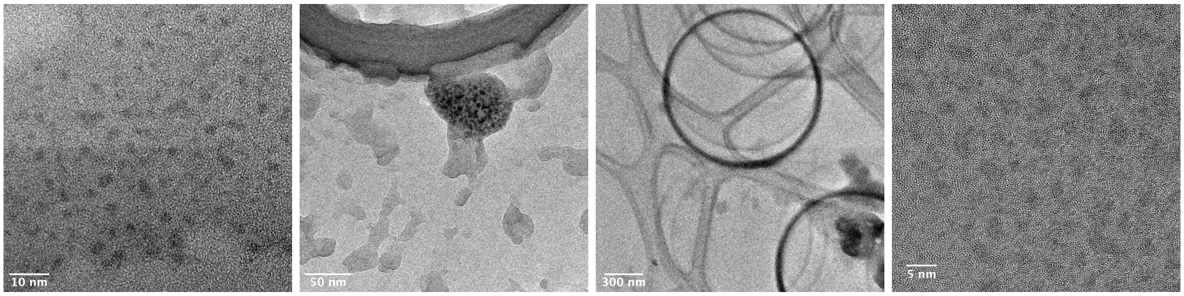

QDs showing excess ligand or carbon on the grid that leaves a shadowing effect (left) or separate structures with aggregation of the QDs (middle left). Beam damage (middle right) and poor resolution/grainy image (right) due to excess organics in the sample.

5) Using imageJ/working up images

a) Setting the scale of the image

Open .dm3 files that digital micrograph program creates, if you have any issues opening them redownload imageJ and it should work. The .dm3 file has scale built into it so no need to "train" the program. For tiff files from TIA (with scale bar, Frodo), open the image, draw a line across the scale bar, and go to analyze>set scale> and type in what the length should be (whatever the scale bar says). For tiff images with no scale bar (Sam), the image has scale already set but the default is microns rather than nanometers. To change to nm, analyze>set scale and change known distance to "1000" and unit to "nm".

b) Adding scale bars

To add a scale bar go analyze> tools> scale bar and choose the length you want the scale bar to cover. I recommend increasing the font size (80) and height (20) for BF images or font (40) and height (12) for STEM images. You can also check “hide text” to get just the scale bar. When you save the image, change the file name to denote the scale and then you can easily edit font size for the scale bar when making presentations. Note: When adding text to TEM images, I recommend white text with a back border to make it more visible for images with high variability in contrast. I usually select the text, format text, add glow, then add a black glow with 3 pt and 0% transparency.

c) *Measuring particles (making distribution plots, tips to avoid bias)*

To start, pick images that have well defined edges on the nanoparticles or are high enough resolution to clearly see the edges of the nanoparticles (lattice fringes, etc). I typically use 20 nm scale bar images for 4-10 nm particles or 5-10 nm scale bar for nanoparticles under 4 nm. Zoom into the image so you can clearly see particles and accurately measure. To measure particles, select the line tool and make sure your scale is properly set. Draw a line across a particle and press “m” to take a measurement, this will create a chart with the length corresponding to what you just measured. Continue measuring until you have enough data points (for a rough measure, over 100 particles or for a high-quality distribution, over 250 particles) and then copy and paste the chart into excel (or whatever software you prefer) to make graphs. For consistency, I recommend doing all your measurements for a sample at one time without taking breaks as there can be variations in how you measure from day to day. Also determine a method for measurement for a given sample and stick with it. For rectangles, choose a given side (or measure in two data sets). Triangles determine if you’ll measure through the center or a side. For round nanoparticles, I recommend measuring in one direction (example: top to bottom on the particle) so that you aren’t tempted to always measure a smaller or larger size if the nanoparticles are a little anisotropic. To remove bias, I recommend not looking at the length as you measure as you may be biased by what you expect the size to be or want it to be. You should also always measure form multiple images and measure any nanoparticle you can see so that you don't bias toward the larger/darker ones. You can also leave lines or boxes on an image (if you want to mark off what particles you've measured or highlight a feature) by drawing it out then pressing "b". By double clocking the line tool you can adjust the thickness of the lines.

d) *Making histograms*

There is a histogram graph that is premade in excel but it doesn't allow for you to customize it as much with labels and appearance. There is also a histogram function in imageJ but the graphs aren't very customizable. I start by making the histogram in excel, up the number of bins to 30, then denote categories that I want for my graph (0.5, 1, 1.5, 2, etc.). Once I have set my categories, I sum the number of counts per category (so for 1.5, I count how many between 1.25 and 1.75) and manually input it into a new column. Once done, I highlight the totals, make a bar graph, and assign the category labels following the ones set above (0.5, 1, 1.5, 2, etc.).

e) *Adding filters to remove background signal*

Some images have significant artifacts that can be removed by adding a filter to the image. There are various types of filters (high-pass, low-pass, or generally a bandpass) that can help improve the signal to noise of the image. They remove certain frequencies in the image, in this case associated with noise or an artifact, and leave frequencies pertaining to the area of interest. To add a bandpass filter in imageJ, process> FFT> bandpass filter. A pop up will appear with different parameters, I typically play around with different settings until I'm happy with the image produced.

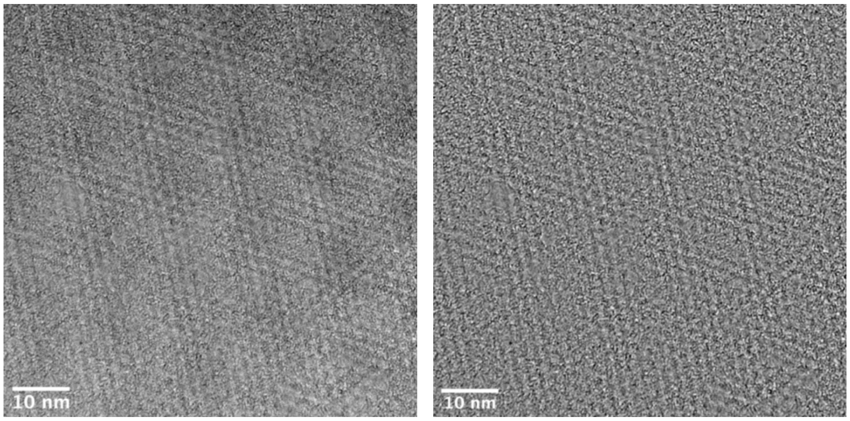

Images of InP MSCs in a superlattice before and after applying a bandpass filter.

f) *Stacking/aligning images*

In cryo-EM they increase the signal to noise of an image by stacking identical images. To do so, you must take multiple images of the same area without moving. This works best if you do so quickly and after letting the sample settle to avoid drift. In imageJ, open the images then form a stack (image>stacks>images to stack). This will create a stack where each image is considered a slice. You can download a plugin (align slice) to align each image relative to each other and remove any drift. Once then are aligned, unstack the images (image>stacks>stack to images). From there, you'll take one image as the base then add overlays of the other images. To add an overlay, select the base image then go image>overlay>add image and a pop up will appear that has a drop down where you can select which image to add as an overlay. There is no need to add an X or Y translation since you already aligned the images, but you want to set it to 50% or less transparency. If your images are properly aligned, this will make the features of interest clearer and make the background blurrier due to overlapping random noise. Repeat adding overlays until you've added all the images you want. Once you are satisfied you can flatten them to make one final image (image>overlay>flatten) that you can save.

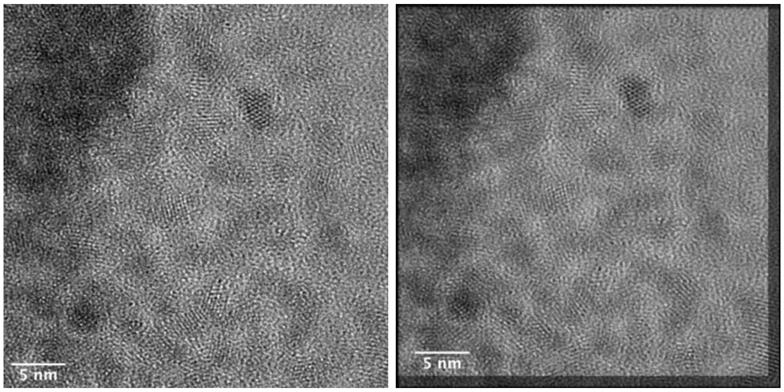

CdSe QDs in a single image (left) and in 3 stacked images that have been aligned (right).

g) *How to measure FFT*

To measure the FFT, use the rectangle tool to select either the whole image or a portion of it. Once the area is selected to go process> FFT> FFT to create the FFT. Once the FFT is created, you can zoom in and alter the brightness/contrast to better resolve the spots (image> adjust> brightness/contrast). Measuring the whole image will give you a sum of all the particles present, leading to many different orientations of the nanoparticles (assuming no superlattice is present). To obtain a clearer image, select just one particle with clear lattice structure and do the FFT.

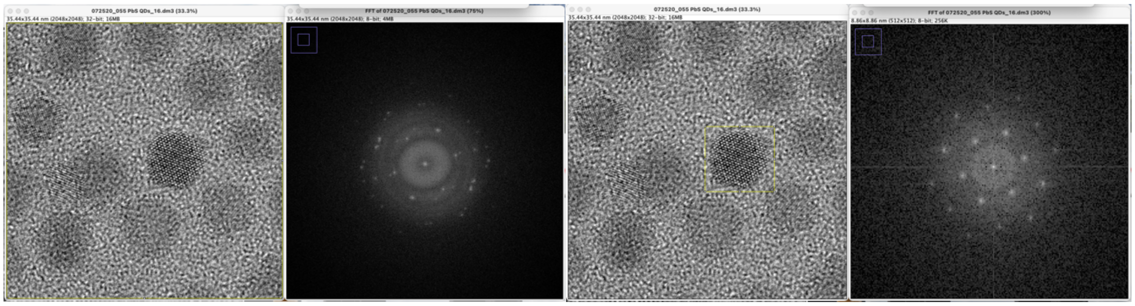

FFT of the entire image showing a polycrystal (left) vs selecting one well defined particle showing a singly crystal (right).

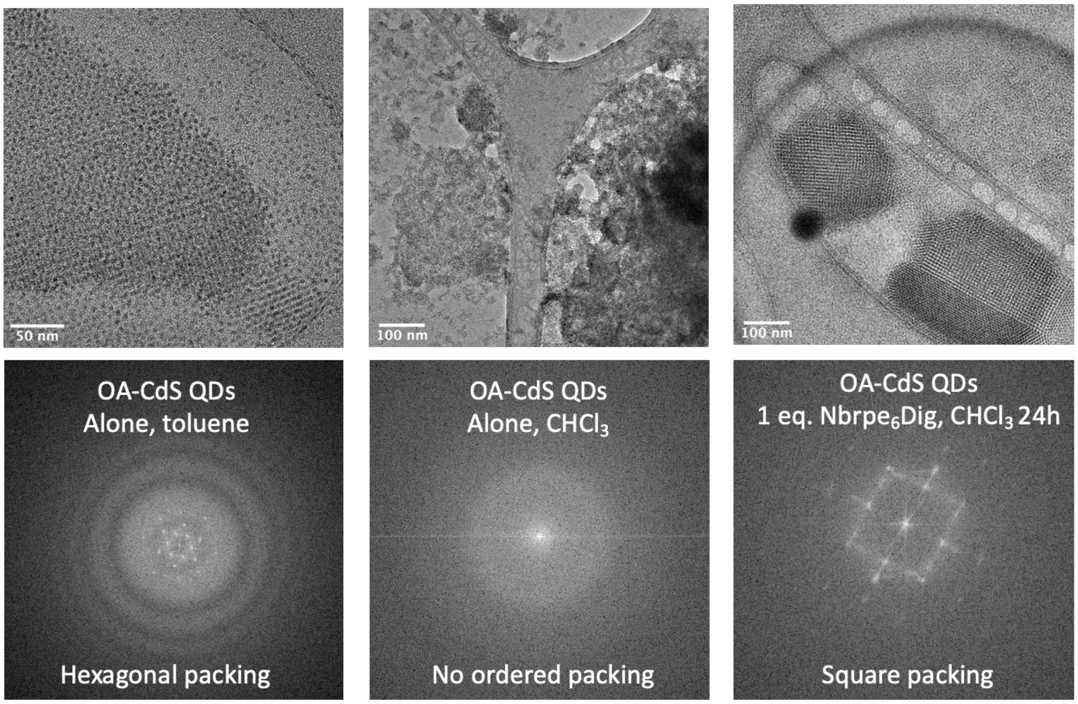

FFT of assemblies showing different packing patterns vs amorphous packing.

h) Measuring lattice fringes

There are several ways to measure the lattice fringes via manual and automated methods. To automate it, draw a line across the lattice fringes you want to measure then analyze> plot profile and it will give you a plot of the grey value vs distance for the line you drew. You can then export the data as XY points and plot in other software or measure the distance between peaks to get the lattice spacing.

For manual analysis, zoom into the lattice fringes and measure the space between the lines. I recommend measuring several points across a given line and between several different lines to get a good average of the spacing. For images that do not have lines but rather a grid-like arrangement, you can draw a line of a given row and press “b”, this will keep the line you’ve drawn. Do so for two adjacent planes then measure the distance between the lines.

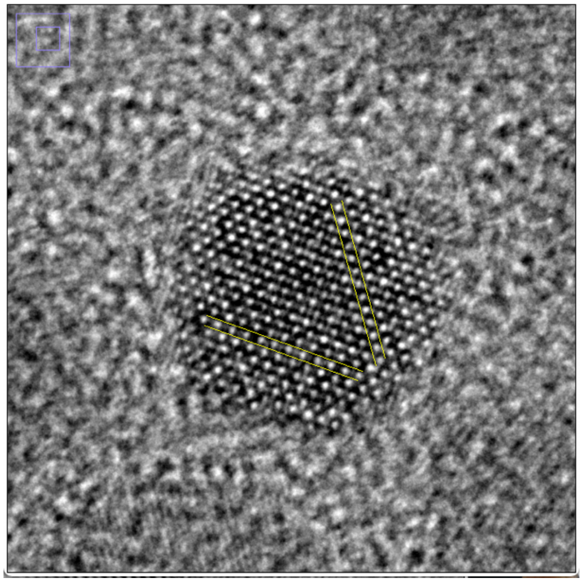

6) STEM mode

a) When to use

STEM is best for getting more 3D information as it has better z-contrast than standard BF. It also is better for recognition or characterization of carbon-based materials as it has better overall contrast. It can be much more damaging than regular BF as the beam is highly concentrated and always rastering across the image area. This makes STEM unideal for easily damaged samples (proteins or delicate other carbon structures, clusters, or nanoparticles under 3 nm). For carbon-based structures, STEM can be useful as an initial screening at low magnification to get a survey for all of the structures in the sample. Once I find an area of interest, I usually switch of BF for higher resolution and less sample damage.

b) Tips to help with focus and alignment

Aligning in STEM can be tricky, especially when it's pretty off. I usually align the ppx, ppy, and rotation center before the condenser aperture. Doing those alignments first can make the ronchiogram centered and easier to adjust to a rounded spot. If you have a sample that damages easily, it will be very hard to align it once you've damaged the area so you may have to move around a bit as you align the beam. Unless I'm going EDS, I use a spot size of 9 to get the highest resolution. To focus the image, focus on the lacey carbon away from the area you want to image and only lightly change the focus from there. Taking too long to focus in an area will result in destruction of the sample.

7) Tomography

a) When to use

Tomography is a useful tool to examine the 3D structure of a sample to investigate the thickness. A sample is a good candidate it is small enough that can tilt and keep the whole sample in the frame (under ~5 microns) and has an area of interest in the tilt direction you have (left to right in brightfield). It also helps if you have a well-defined area of interest that should remain present throughout the tilting. The area of interest should also be near the center of a grid hole, so the grid bar doesn't get in the way when you tilt.

b) Tilting and aligning by hand

The automated program is a bit bulky and have a significant shift in the middle of the tilt series. I always prefer to tilt by hand to roughly align the images prior to doing so after image collection. By hand, I identify an area/object of interest that I want the tilt series of left to right. I get a baseline image at 0 tilt and select a prominent feature in the rough center of the object that I want to be my rotation axis. I then take the corner of a posted note and place it at that focal point, this will be my reference point on where I will focus the image and align the sample to as I tilt. I then tilt as far as I can in one direction without seeing grid bars and use that as my start point (usually between -60 to -45 degrees). I align and focus the image at my designated point, take the image, then tilt 5 degrees from my start point and realign and focus. I do this ever 5 degrees until I’ve completed the tilt series. I save the images, being careful to save them in order and open all of the in order in imageJ (note: it is important they open in order as when you stack the images, they will not stack by name but rather the order which they were opened). Once the images are open, stack them (image>stack>images to stack) and open the align slice, you must download this plug in in addition to regular imageJ (plugins>align slice). Place your marker on the same feature of interest that you picked during imaging and align the images by adjusting the XY directions until the focal point is aligned with your marker. Once all the images are aligned, they can be placed as a movie and recorded via a screen recording. You can also save the stack to be reopened at another time.

c) *Calculating sample thickness*

To calculate sample thickness using tomography, take two images (one at 0-degree tilt and one at high, tilt like 65 degrees). Identify where in the sample you want to measure the thickness. I recommend measuring a certain distance from the top or bottom of the feature to be consistent through both images. Measure the width at that point for both images. You should also calculate what you’ll expect for thickness of your material (one layer of QDs or a layer of QDs+peptoid or other materials). You can then measure the expected width for the feature at a given tilt for your material (see below for example).

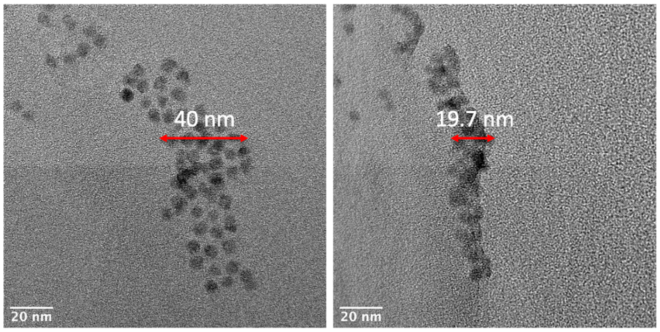

At 65° tilt
Actual width= 19.7 nm
Expected monolayer width= 19.4 nm

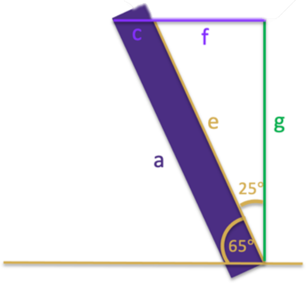

a = 40 nm (measured at 0° tilt)
b = 5.3 nm (estimated thickness if one later of 5nm QDs)

e + d = 40 nm

x = width observed at high tilt
c + f = x

$Cos(25) = \frac{5.3}{c}$
c = 5.85 nm
$d = \sqrt{(c^2 - b^2)}$
d = 7.89 nm

e = 40 – d
e = 32.1 nm

$Cos(25) = \frac{g}{e}$
g = 29.1 nm

$f = \sqrt{(e^2 - g^2)}$
f = 13.6 nm

x = c + f
x = 19.4 nm

8) EDS

a) Considerations/sample requirements

The sample you want to image must be stable under the STEM beam with limited sample damage. If your sample is highly susceptible to beam damage, it will lead to a lot of drift and inaccurate/blurry mapping. It is best to reduce carbon on the sample prior to imaging (either from plasma cleaning or chemical stripping in situ). You can also mitigate sample drift by altering the image conditions to scan for a shorter period or time or image at lower magnification where sample drift is less noticeable. You will also more than likely have to use a larger spot size to get better signal which will be more damaging for the sample so keep that in mind. Getting good signal is a balance of collection time, number of frames, and sample stability. The more stable your sample is, the longer you can collect, and the nicer the image will be. If you have a less stable sample, it is better to so a higher number of scans with shorter collection or dwell time because it'll damage more slowly.

b) *Typical imaging conditions for QD based samples:*

  - *i)* Amp time of 7.58 us (you may have to decrease if you have a lot of counts)
  - *ii)* Dwell time of 50 us (how long it scans at each point, limited for QDs due to damage)
  - *iii)* 8-32 frames (number of times it goes across the image, higher number decreases signal to noise)
  - *iv)* Image resolution of 512x400 (how many pixels or points in reference image)
  - *v)* Map resolution of either 512x400 or 256x200 (how many pixels or points in map image (plus/minus one of image). The lower the resolution the better color distribution (less scattered) it'll have but also less accuracy.
  - *vi)* Spot size of 7 (lower number, more intense, higher counts but more damage)

c) *General tips*

If you go above 1024x800 image the program tends to freeze and the files sizes become huge. Higher image size gives better spatial resolution and smaller pixel sizes. Dwell time is how long the detector measures or the beam sits at each point in the image. Longer time not always better, time to collect more signal but also leads to more damage and sample drift. Often the sample remains more stable by shortening the dwell time and doing more scans to get the same amount of signal collection with less rapid sample damage. It helps to put the detector in before handing off to EDAX software. The detector will shift the image and change the alignment/focus. Check that you are still in the area of interest, in focus, and that the condenser aperture hasn't become misaligned (common)

9) Liquid-phase

a) When to use and considerations

Liquid-phase TEM is useful when you have a sample that you want to investigate the mechanism of assembly or formation or rule out drying effects for generated structures. The sample should either be on the larger side (above 10 nm) or high(er) contrast as low contrast, small particles such as InP or CdSe are very hard to identify through the solvent. You will also need to consider beam damage and interactions with solvent. Most solvents have some sort of degradation under the electron beam and will go one to react/degrade your sample.

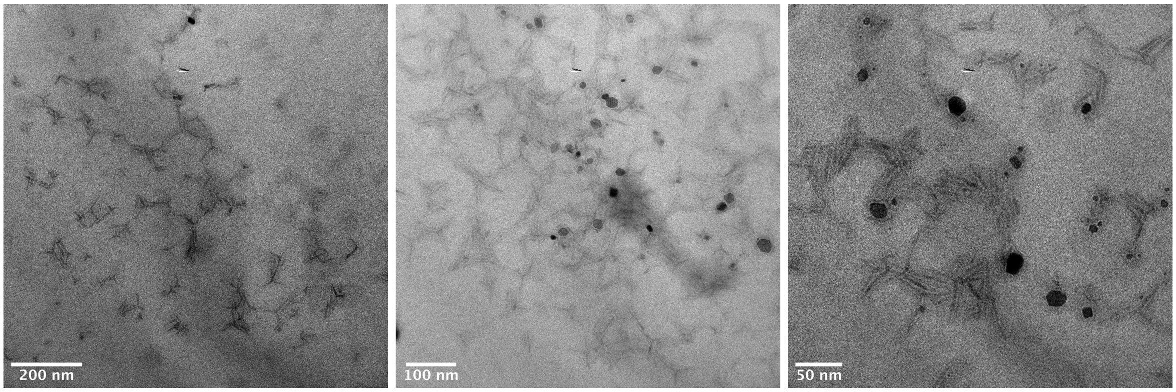

CdSe/CdS tetrapods in toluene initally (left) and after degridation of solvent and sample (middle and right) to produce CdO structures (black).

b) Useful solvents and what to avoid

You should not use toluene (dissolves the glue and dries quickly), dodecane OK, and water is well vetted. You want to choose something conjugated that can take an electron without destroying the molecule and higher BP so doesn't dry quickly. (REF). There is a tester kit in the microscopy drawer so you can check different solvents compatibility with the liquid cell holder. I recommend taking them to a dissecting microscope (in TEM rooms or AFM labs) and take images before exposing to the solvent of interest then again after. If you see evidence of degradation on any of the components, then you shouldn’t use that solvent.

References:

1. Zhu, G.; Reiner, H.; Cölfen, H.; De Yoreo, J. J. Addressing Some of the Technical Challenges Associated with Liquid Phase S/TEM Studies of Particle Nucleation, Growth and Assembly. *Micron* **2019**, *118*, 35–42.
2. Pyrz, W. D.; Buttrey, D. J. Particle Size Determination Using TEM: A Discussion of Image Acquisition and Analysis for the Novice Microscopist. *Langmuir* **2008**, *24* (20), 11350–11360.
3. De Yoreo, J. J.; N. a. J. M., S. Investigating Materials Formation with Liquid-Phase and Cryogenic TEM. *Nat Rev Mater* **2016**, *1* (8), 1–18.
4. Hinks, J. A. A Review of Transmission Electron Microscopes with in Situ Ion Irradiation. *Nuclear Instruments and Methods in Physics Research Section B: Beam Interactions with Materials and Atoms* **2009**, *267* (23), 3652–3662.
5. Rehn, S. M.; Jones, M. R. New Strategies for Probing Energy Systems with In Situ Liquid-Phase Transmission Electron Microscopy. *ACS Energy Lett.* **2018**, *3* (6), 1269–1278.
6. Nielsen, M. H.; De Yoreo, J. J. Liquid Phase TEM Investigations of Crystal Nucleation, Growth, and Transformation. In *New Perspectives on Mineral Nucleation and Growth: From Solution Precursors to Solid Materials*; Van Driessche, A. E. S., Kellermeier, M., Benning, L. G., Gebauer, D., Eds.; Springer International Publishing: Cham, 2017; pp 353–374.
7. Chen, Q.; Dwyer, C.; Sheng, G.; Zhu, C.; Li, X.; Zheng, C.; Zhu, Y. Imaging Beam-Sensitive Materials by Electron Microscopy. *Advanced Materials* **2020**, *32* (16), 1907619.
8. Egerton, R. F. Choice of Operating Voltage for a Transmission Electron Microscope. *Ultramicroscopy* **2014**, *145*, 85–93.
9. Egerton, R. F. Radiation Damage to Organic and Inorganic Specimens in the TEM. *Micron* **2019**, *119*, 72–87.
10. Yoshida, K.; Biskupek, J.; Kurata, H.; Kaiser, U. Critical Conditions for Atomic Resolution Imaging of Molecular Crystals by Aberration-Corrected HRTEM. *Ultramicroscopy* **2015**, *159*, 73–80.
11. Su, D. Advanced Electron Microscopy Characterization of Nanomaterials for Catalysis. *Green Energy & Environment* **2017**, *2* (2), 70–83.
12. Levin, B. D. A.; Padgett, E.; Chen, C.-C.; Scott, M. C.; Xu, R.; Theis, W.; Jiang, Y.; Yang, Y.; Ophus, C.; Zhang, H.; Ha, D.-H.; Wang, D.; Yu, Y.; Abruña, H. D.; Robinson, R. D.; Ercius, P.; Kourkoutis, L. F.; Miao, J.; Muller, D. A.; Hovden, R. Nanomaterial Datasets to Advance Tomography in Scanning Transmission Electron Microscopy. *Sci Data* **2016**, *3* (1), 160041.

VITA

Madison Monahan was born in Durham, North Carolina (as a Gladding) before moving to Oregon where she grew up with her older sister, Bethany, and younger brother, Caleb. Madison spent much of her childhood outside, torturing her siblings with jump scares and spiders. In high school, she split her time between school, sports, and volunteering. While she was certain she would go into the medical field and become a surgeon, Madison discovered a love of chemistry in high school and went on to major in chemistry with minor in mathematics at Linfield College. During her time at Linfield, Madison met Clay through hurdling and, after some friendly competition to see who was faster, they wed shortly after graduating college. They moved to Washington where Madison started her Ph.D. in chemistry at the University of Washington. Over the years, they acquired two unofficial therapy dogs, Gris and Glen, that kept them busy and were always down for a stress nap. Madison swore she would never follow her father's footsteps as a microscopist, as it would be too boring to stare into a microscope all day, but has since eaten her words after falling in love with electron microscopy and started a career in industry specializing in just that.